UNIVERSITY OF CALIFORNIA
RIVERSIDE

Structure-Activity Relationship in Transition Metal Boride for Hydrogen Evolution Reaction Electrocatalyst

A Dissertation submitted in partial satisfaction
of the requirements for the degree of

Doctor of Philosophy

in

Chemical and Environmental Engineering

by

Eunsoo Lee

June 2022

Dissertation Committee:
Dr. Boniface P. T. Fokwa, Chairperson
Dr. Juchen Guo
Dr. Robert Jinkerson

The Dissertation of Eunsoo Lee is approved:

_____

_____

_____

Committee Chairperson

University of California, Riverside

ACKNOWLEDGEMENTS

Countless people supported my effort in this thesis. First and most, my big appreciation goes to my supervisor, Professor Boniface Fokwa, for his marvelous supervision, guidance, and encouragement. He always gave me great advice whenever my research was in trouble, and thanks to him, I learned a lot about the basics of chemistry that I was lacking. Sincere gratitude is extended to his generous participation in guiding, constructive feedback, kind support, and advice during my Ph.D. Thank you very much Professor Fokwa.

I would like to thank my Ph.D. committee members, Dr. Juchen Guo and Dr. Robert Jinckerson for taking the time to consider this work. This dissertation could be improved by their meaningful comment and constructive feedback based on their expertise. I appreciate their help.

I am indebted to my past and present lab mates, Dr. Hyounmyung Park, Dr. Amir Ardalan, Dr. Jan Scheifers, Dr. Palani Raja, Dr. Yuemei Zhang, Dr. Abishek Iyer, Dr. Teresa Ortner, Dr. Pritam Shankhari, Johan Yapo, Diana Luong, Sang Bum Kim, and Kate Gibson. In particular, I would like to express my gratitude to Hyounmyung, Amir, Jan, and Raja. A long discussion with them gave me a lot of hints about my research and was able to publish it in a very reputable journal. Moreover, computational results from Yumei and Johan also helped a lot to go one step further. Without their help, it would have been difficult to complete this thesis. Thank you all again.

Last, but not least, my Deepest thanks to my family, who keep me grounded, remind me of what is important in life, and are always supportive of my adventures. My

accomplishment and success are because they believed in me. Especially thanks to my wife Jieun Lee and daughter Yoona Lee for constantly listening to me rant and talk things out and for the sacrifices you have made for me to pursue a Ph.D. degree. I am forever thankful for the unconditional love and support throughout the entire thesis process and every day. I give everything to my family including this.

COPYRIGHT ACKNOWLEDGEMENTS

DFT calculation was conducted by Dr. Yuemei Zhang and Johan Yapo.

ABSTRACT OF THE DISSERTATION

Structure-Activity Relationship in Transition Metal Boride for Hydrogen Evolution Reaction Electrocatalyst

by

Eunsoo Lee

Doctor of Philosophy, Graduate Program in Chemical and Environmental Engineering
University of California, Riverside, June 2022
Dr. Boniface P. T. Fokwa, Chairperson

Hydrogen, as an abundant and clean, renewable energy source, has taken the center stage to replace carbon-based fuels. Among hydrogen generation strategies, electrochemical water splitting through hydrogen evolution reaction (HER) is a green and efficient approach for hydrogen production. However, industrializing this technology is not yet efficient enough, due to the high expenses of needed metals such as platinum.

Recently, transition metal borides (TMBs) have been proposed as potential electrocatalysts for HER applications, both for bulk and nanoscale materials, owing to their low cost, high activity, and stability in acidic and basic electrolytes. Meanwhile, some studies indicate that boron covalent networks in crystal structures play an important role in electrocatalytic activity. Therefore, further research on structure-activity relationships is required to understand and possibly even predict more active and efficient catalysts.

Herein, we propose the possible application of transition metal diborides as electrochemical catalysts for HER. Firstly, the high activity of V_xB_y has been rationalized by studying the effect of aggregating boron chains as a function of HER activity. A structure-activity relationship is found that helps to predict new phases and HER overpotentials. Then, we report on an unusual volcano-like behavior of the *c* lattice parameter in the AlB_2-type solid solution $V_{1-x}Mo_xB_2$ (x = 0, 0.1, 0.3, 0.5, 0.7, 0.9, 1) and its direct correlation to the HER activity in 0.5 M H_2SO_4 solution. Further, a more detailed structure-activity relationship in transition metal boride studied in the lab since 2017 is summarized. In addition to the transition metal boride, we apply Mo_2BC to HER electrocatalyst in both acid and alkaline electrolytes for the first time and suggest the synergy effect of β-MoB and α-MoC substructure in Mo_2BC crystal structure. Moreover, a suitable electrode preparation method beyond dense electrodes, which was studied in our previous report, is proposed for maximizing HER activity. Finally, we report on the experimental and theoretical investigations of the HER activity of $Fe_{5-x}Ge_2Te_2$. It is a recently discovered iron-richer phase that is structurally related to Fe_3GeT_2.

Table of Contents

List of Figures

List of Tables

Chapter 1.

Introduction

1.1. An Overview of Hydrogen Energy and Electrocatalysts

Since the industrial revolution, global warming has progressed dramatically, with a surge in demand for fossil fuels such as natural gas, coal, and oil. Global energy needs will increase by 30 % between today and 2040.[1] This situation will cause a depletion of fossil fuels, as well as a serious environmental pollution problem. The need for alternative energy sources to replace carbon-based fuels is undoubtedly pressing.[2-3] Recently, the "Hydrogen economy"- a forthcoming energy system based on hydrogen energy- has drawn attention, as concerns about environmental issues have been rising.[4-5] Hydrogen is a clean and renewable energy source, with more specific energy (33.3 kWh/kg) than other fuels (natural gas: 13.9 kWh/kg, diesel: 12.6 kWh/kg, coal: 8.2 kWh/kg).[6] However, a groundbreaking method is needed to produce large amounts of hydrogen, as 150 million tons/year of hydrogen would be required just for U.S. transportation alone.[7]

So far, about 66 % of global hydrogen is produced through coal gasification and methane reforming at a relatively low cost. However, this method produces CO_2 as a by-product, which dramatically accelerates global climate change.[6] As an alternative, electrochemical water splitting through the hydrogen evolution reaction (HER) is a promising method to produce hydrogen. It is not only a clean and efficient technology but can also easily be coupled with other renewable sources such as solar- and wind power.[8]

Still, despite the merits compared to coal gasification, platinum-based catalysts, the most active catalyst for HER found so far, are too costly to be used in the industry.[9-11]

To date, efficient, non-noble metal HER electrocatalysts have been synthesized, based on twelve non-precious elements, as highlighted in **Figure 1.1**. To be specific, electrocatalysts based on these elements, such as transition metal carbides[12-13], chalcogenides[14-16], borides[17-18], and phosphides[19-20], have been widely employed to substitute precious metal electrocatalysts. Among these alternatives, transition metal borides (TMBs) have received a great amount of attention due to their low cost, high activity, and stability in both acidic and basic electrolytes.[21-23] The various covalent networks formed by boron, such as 1D chains, 2D sheets, and also 3D networks, dictate the numerous different crystal structures of TMBs and significantly impact their catalytic activity. Boron's properties, such as electron count, electronegativity, and ionization energy, determine not only the arrangement of boron atoms in the structure but also the physical properties of the boride.[24-25] Therefore, it is necessary to study the structure-activity relations to understand and improve the HER activity of boride catalysts. Innovative methods to synthesize ternary and nano-sized TMBs are required to legitimately compete with Pt-based catalysts. A systematic study on TMBs is proposed in this thesis, aiming to understand the effect of boron chains on HER activity.

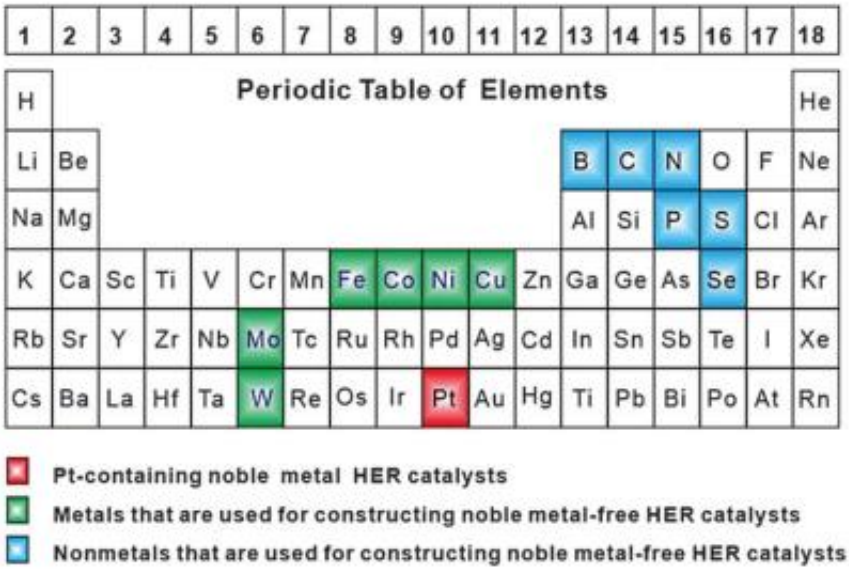

Figure 1.1. Elements that are used in HER electrocatalysts.[26]

1.2. Hydrogen Evolution Reaction (HER)

The HER ($2H^+ + 2e^- \rightarrow H_2$) is a multistep, cathodic reaction taking place on the surface of an electrode. **Figure 1.2** shows the reaction mechanisms in acidic and alkaline solutions.[27-28] The initial proton discharge to form adsorbed hydrogen (H_{ad}) (Volmer reaction) is followed by either the recombination of the H_{ad} to form H_2 (Tafel reaction), or electrochemical desorption of the adsorbed intermediate to form H_2 (Heyrovsky reaction), as shown in **Figure 1.2**. The possible reaction kinetics for HER can be discerned by the Tafel slope value. The Tafel slope is calculated by the linear portions of the fitted Tafel equation at low overpotential ($\eta = b log\, j + a$; η is the overpotential; j is the current density; b is the Tafel slope). At room temperature, the Tafel slope of Volmer, Heyrovsky, and Tafel reactions are 120, 40, and 30 mV/dec., respectively.

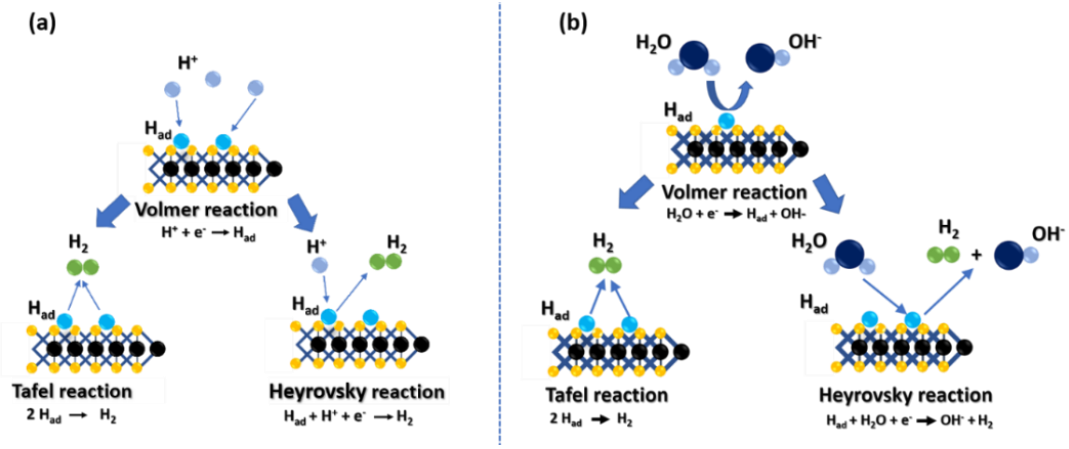

Figure 1.2. HER mechanisms in (a) acidic and (b) alkaline solution.

In reaction kinetics, the equilibrium constant K is defined as the value of the reaction quotient at the thermodynamic equilibrium. K can be expressed as a function of the free energy change for the adsorption on a catalyst surface (ΔG_H).[26] If ΔG_H is negative, the adsorbed hydrogen H_{ads} is bound strongly to the electrode surface, making the initial Volmer step easy, but the subsequent Tafel or Heyrovsky step difficult. If ΔG_H is large and positive, H_{ads} has a weak interaction with the electrode surface, resulting in a slow Volmer step that limits the overall turnover rate. It means that according to the Sabatier principle (the best catalyst should bind atoms and molecules with an intermediate strength), ΔG_H should be zero, to achieve a maximum rate of the overall reaction. The ideal catalyst is not too weak to be able to activate the reactants, and not too strong to be able to desorb the products. Therefore, ΔG_H is a widely accepted descriptor to evaluate HER electrocatalysts.[29-30]

Another point to consider when designing HER electrocatalysts are the reaction overpotentials. The theoretical voltage, which splits water into hydrogen, is 0 V for the

HER at 298 K. Extra electricity is needed, however, to overcome an overpotential caused by the activation energy barrier.[26] The equation $E_{electrolysis} = E_{reversible} + \Delta E_{irreversible} + IR$ represents the energy sum needed, where $E_{reversible}$ is the theoretical decomposition voltage, $\Delta E_{irreversible}$ is the overpotential for the HER, and IR accounts for the voltage drop caused by the electrolyte, wires, and contact points. Thereby, the overpotential ($\Delta E_{irreversible}$) is caused by two factors: concentration polarization and electrochemical polarization. The concentration polarization can be resolved by boosting ion diffusion through stirring or increasing operation temperature; the electrochemical polarization can be reduced by the use of an appropriate electrocatalyst.[31] Concentration polarization and IR drop can hence easily be reduced by controlling the experimental conditions and IR compensation. Decreasing the electrochemical polarization is, however, not as simple. Because appropriate electrocatalysts for compensating the electrochemical polarization are Pt-based materials which are very expensive and scarce. Therefore, investigating non-noble-metal-based catalysts are required to improve energy efficiency and reduce the price.

1.3. Transition Metal Borides (TMBs)

Among the non-noble-metal-based catalysts, we are trying to focus on TMB materials because of their low cost, high activity, and stability in both acidic and basic electrolytes.[26] TMBs can be classified as highly refractory and corrosion-resistant compounds. Several studies of TMBs show that the borides have metallic properties as well as high hardness and inertness, with high melting points. Furthermore, due to

boron's properties, the covalent networks of TMBs contain a plethora of structure forms, ranging from 1D chains to 2D sheets to 3D networks. Thus, TMBs have different physical properties, based on different crystal structures, which are determined by the arrangement of boron atoms as depicted in **Figure 1.3**.[24]

The arrangement of boron atoms in TMBs can be determined by the metal to boron ratio, generally ranging from 4:1 to 1:12. Metal-rich borides can have compositions of M_4B, M_3B (e.g., Re_3B), M_5B_2, M_7B_3, or M_2B (e.g., Ta_2B, Mo_2B, and W_2B). These are structures, where boron atoms do not form any boron network. In M_5B_3 and M_3B_2 (e.g., Nb_3B_2 and Ta_3B_2), isolated boron pairs are observed. As the boron content increases, zigzag boron chains (MB; e.g., NbB, TaB, MoB and WB), double chains (M_3B_4; e.g., Nb_3B_4, V_3B_4, and Ta_3B_4), planar (MB_2; e.g.,NbB_2, TaB_2, MoB_2, and VB_2) and corrugated layers (MB_2; e.g., ReB_2) are described.[32] The various arrangement of boron in TMBs results in a multitude of properties. For example, TMBs have been used as catalysts for hydrogenations and reductions (Ni_2B)[33], permanent magnets ($Nd_2Fe_{14}B$)[34], superconductors (MgB_2), or hard and high-temperature materials (TiB_2, ZrB_2)[24]. However, commercial applications of borides are limited, because most TMB synthesis methods require high temperature.

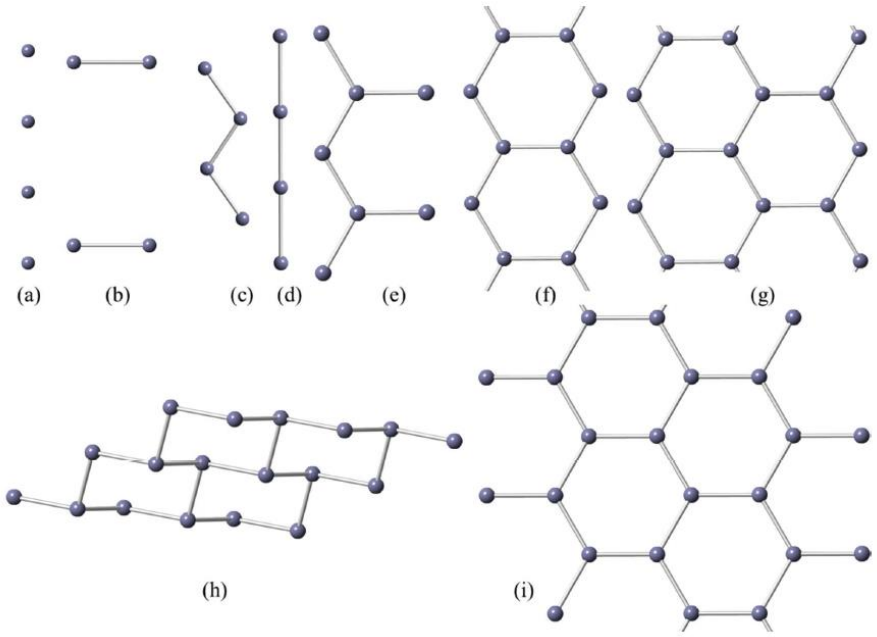

Figure 1.3. Different structural elements formed by boron atoms in TMBs: a) isolated boron atoms; b) pairs; c) zig-zag chains; d) straight (ordinary) chains; e) extended chains; f) double chains; g) triple chains; h) corrugated networks; and i) flat networks of boron atoms.[24]

1.4. Synthesis Method

1.4.1 Arc Melting

For the synthesis of polycrystalline samples, electric arc melting of pressed metal and boron powders of appropriate stoichiometry in an inert atmosphere is a widely used method in solid-state chemistry. In this system, the applied electric energy is directly heating the reactants, as the electrical current passes through the charged material between the electrodes of the furnace. It is a very practical and powerful method when a very high temperature is required to synthesize. Arc melting allows reaching temperatures higher than 3000 ^{o}C in a time as short as a few seconds. Lower metal borides like TiB, ReB_2, NbB_2, and WB_4, dodecaborides like ErB_{12}, YB_{12}, and ScB_{12}, and

β-rhombohedral boron can be synthesized *via* this method.[24] Today, several commercial arc melting furnaces for research laboratory applications are available. All these models have water-cooled copper crucibles for one or more samples. The furnaces are operated with a tungsten electrode under an inert atmosphere (argon), and the complete setups are equipped with a Schlenk (vacuum-argon) line. In general, the power supply is connected to a welding electric rectifier and the power can be controlled by a foot pedal during the melting process.[32]

1.4.2 Metal-flux assisted synthesis

High-temperature reactions between solid reactants are based on diffusion. Since the reactants are powders, it takes a lot of time to diffuse into each other, which means accelerating the rate of diffusion can reduce the activation energy barrier substantially. To achieve enhanced diffusion of reactants in solid-state synthesis, molten solids can be used as solvents. It is an excellent preparative tool for the explorative synthesis of new materials, as large single-crystals can be grown using this method as well. Several key characteristics must be fulfilled for a metal to be a viable flux for reaction chemistry: 1) the metal should melt at reasonably low temperatures; 2) there should be a large difference between its melting point and boiling point; 3) it should be possible to separate the metal from the products; 4) the metal flux should not form highly stable binary compounds with any of the reactants.[35] Single crystals of monoborides and diborides can be synthesized *via* this method with Al, Sn, and Bi which is most commonly used as flux metal.[24]

1.5. Characterization Techniques

1.5.1. Powder X-ray diffraction (PXRD)

PXRD measurements were performed using Rigaku Miniflex-600 (Japan). The scanning voltage was 40 kV, and the scanning current was 15 mA which generated Cu K_α radiation (λ=1.5418 Å). The recorded PXRD patterns were refined using the Rietveld method (full-matrix least-squares refinement) as carried out in the FULLPROF program suite. The crystal phases information was certified by the standard ICSD database.

1.5.2. XPS, SEM, and EDX

X-ray photoelectron spectroscopy (XPS) spectrum was recorded using a Kratos AXIS ULTRA ^{DLD} XPS (Japan) system equipped with an A1 Kα monochromated X-ray source and a 165 mm mean radius hemispherical electron energy analyzer. The surface morphology and mapping images were characterized using scanning electron microscopy (SEM) and energy-dispersive X-ray spectroscopy (EDS), respectively, on an ultra-high-resolution low-energy system of the type Nova NanoSEM450 equipped with a 50mm^2 X-Max50 SD EDX detector.

1.5.4. Electrochemical characterization

The electrochemical tests of the samples were carried out on a VSP electrochemical workstation (Bio-Logic Science Instruments, France) using a three-electrode system: prepared electrode of our sample as a working electrode, graphite rod, and saturated calomel electrode (SCE) as the counter and reference electrodes, respectively, in 0.5 M H_2SO_4 electrolyte solution. All the potentials are translated into the reversible hydrogen electrode (RHE) according to the equation: $E_{RHE} = E_{SCE} + 0.242\ V +$

0.059×pH. All the measurements were obtained by *iR*-drop compensation. Linear sweep voltammetry (LSV) plots were used to measure electrochemical HER activity with a scan rate of 5 mV/s. It was recorded after 10 cycles of cyclic voltammetry (CV) tests. The Tafel equation $\eta = b\,log\,j + a$ (where j is the current density, b is the Tafel slope, and a is the intercept relative to the exchange current density j_o) was used to calculate the Tafel slopes by fitting the linear part of the Tafel plots. Electrochemical impedance spectroscopy (EIS) was conducted at the overpotential at -10 mV/cm^2 current density by applying an AC voltage over the frequency range from 500 kHz to 100 mHz with an amplitude of 10 mV versus the open-circuit potential. The electrochemically active surface area was estimated through CV tests using different scan rates within a non-faradic reaction region. The double-layer capacitance was calculated by plotting the ΔJ (J_a-J_c) against the scan rate.

1.6. Reference

1. Agency, I. E. *World Energy Outlook 2017*; International Energy Agency: 2017.
2. Bard, A. J.; Fox, M. A., Artificial photosynthesis: solar splitting of water to hydrogen and oxygen. *Accounts of Chemical Research* **1995,** *28* (3), 141-145.
3. Chow, J.; Kopp, R. J.; Portney, P. R., Energy resources and global development. *Science* **2003,** *302* (5650), 1528-1531.
4. Crabtree, G. W.; Dresselhaus, M. S.; Buchanan, M. V., The hydrogen economy. *Physics today* **2004,** *57* (12), 39-44.
5. Marbán, G.; Valdés-Solís, T., Towards the hydrogen economy? *International Journal of Hydrogen Energy* **2007,** *32* (12), 1625-1637.
6. Edwards, P. P.; Kuznetsov, V. L.; David, W. I.; Brandon, N. P., Hydrogen and fuel cells: towards a sustainable energy future. *Energy policy* **2008,** *36* (12), 4356-4362.
7. Turner, J. A., Sustainable hydrogen production. *Science* **2004,** *305* (5686), 972-974.
8. Cook, T. R.; Dogutan, D. K.; Reece, S. Y.; Surendranath, Y.; Teets, T. S.; Nocera, D. G., Solar energy supply and storage for the legacy and nonlegacy worlds. *Chemical reviews* **2010,** *110* (11), 6474-6502.

9. Zhao, Y.; Kamiya, K.; Hashimoto, K.; Nakanishi, S., In situ CO2-emission assisted synthesis of molybdenum carbonitride nanomaterial as hydrogen evolution electrocatalyst. *Journal of the American Chemical Society* **2014,** *137* (1), 110-113.
10. Anantharaj, S.; Kennedy, J.; Kundu, S., Microwave-initiated facile formation of Ni3Se4 nanoassemblies for enhanced and stable water splitting in neutral and alkaline media. *ACS applied materials & interfaces* **2017,** *9* (10), 8714-8728.
11. Sivanantham, A.; Shanmugam, S., Nickel selenide supported on nickel foam as an efficient and durable non-precious electrocatalyst for the alkaline water electrolysis. *Applied Catalysis B: Environmental* **2017,** *203*, 485-493.
12. Chen, W.-F.; Muckerman, J. T.; Fujita, E., Recent developments in transition metal carbides and nitrides as hydrogen evolution electrocatalysts. *Chemical communications* **2013,** *49* (79), 8896-8909.
13. Ng, V. M. H.; Huang, H.; Zhou, K.; Lee, P. S.; Que, W.; Xu, J. Z.; Kong, L. B., Recent progress in layered transition metal carbides and/or nitrides (MXenes) and their composites: synthesis and applications. *Journal of Materials Chemistry A* **2017,** *5* (7), 3039-3068.
14. Chia, X.; Pumera, M., Layered transition metal dichalcogenide electrochemistry: journey across the periodic table. *Chemical Society Reviews* **2018**.
15. Lu, Q.; Yu, Y.; Ma, Q.; Chen, B.; Zhang, H., 2D Transition-metal-dichalcogenide-nanosheet-based composites for photocatalytic and electrocatalytic hydrogen evolution reactions. *Advanced Materials* **2016,** *28* (10), 1917-1933.
16. Jaramillo, T. F.; Jørgensen, K. P.; Bonde, J.; Nielsen, J. H.; Horch, S.; Chorkendorff, I., Identification of active edge sites for electrochemical H2 evolution from MoS2 nanocatalysts. *science* **2007,** *317* (5834), 100-102.
17. Li, H.; Wen, P.; Li, Q.; Dun, C.; Xing, J.; Lu, C.; Adhikari, S.; Jiang, L.; Carroll, D. L.; Geyer, S. M., Earth-Abundant Iron Diboride (FeB2) Nanoparticles as Highly Active Bifunctional Electrocatalysts for Overall Water Splitting. *Advanced Energy Materials* **2017,** *7* (17), 1700513.
18. Xu, N.; Cao, G.; Chen, Z.; Kang, Q.; Dai, H.; Wang, P., Cobalt nickel boride as an active electrocatalyst for water splitting. *Journal of Materials Chemistry A* **2017,** *5* (24), 12379-12384.
19. Pu, Z.; Amiinu, I. S.; Zhang, C.; Wang, M.; Kou, Z.; Mu, S., Phytic acid-derivative transition metal phosphides encapsulated in N, P-codoped carbon: an efficient and durable hydrogen evolution electrocatalyst in a wide pH range. *Nanoscale* **2017,** *9* (10), 3555-3560.
20. Hong, H.; Liu, C.; Cao, T.; Jin, C.; Wang, S.; Wang, F.; Liu, K., Interfacial engineering of van der waals coupled 2D layered materials. *Advanced Materials Interfaces* **2017,** *4* (9), 1601054.
21. Jothi, P. R.; Zhang, Y.; Scheifers, J. P.; Park, H.; Fokwa, B. P., Molybdenum diboride nanoparticles as a highly efficient electrocatalyst for the hydrogen evolution reaction. *Sustainable Energy & Fuels* **2017,** *1* (9), 1928-1934.

22. Sun, H.; Meng, J.; Jiao, L.; Cheng, F.; Chen, J., A review of transition-metal boride/phosphide-based materials for catalytic hydrogen generation from hydrolysis of boron-hydrides. *Inorganic Chemistry Frontiers* **2018,** *5* (4), 760-772.
23. Mazánek, V.; Nahdi, H.; Luxa, J.; Sofer, Z.; Pumera, M., Electrochemistry of layered metal diborides. *Nanoscale* **2018**.
24. Akopov, G.; Yeung, M. T.; Kaner, R. B., Rediscovering the crystal chemistry of borides. *Advanced Materials* **2017,** *29* (21), 1604506.
25. Albert, B.; Hillebrecht, H., Boron: elementary challenge for experimenters and theoreticians. *Angewandte Chemie International Edition* **2009,** *48* (46), 8640-8668.
26. Zou, X.; Zhang, Y., Noble metal-free hydrogen evolution catalysts for water splitting. *Chemical Society Reviews* **2015,** *44* (15), 5148-5180.
27. Lasia, A., Handbook of fuel cells. *Fundamentals, Technology and Applications* **2010,** *2*, 416-440.
28. Tilak, B.; Chen, C.-P., Generalized analytical expressions for Tafel slope, reaction order and ac impedance for the hydrogen evolution reaction (HER): mechanism of HER on platinum in alkaline media. *Journal of Applied Electrochemistry* **1993,** *23* (6), 631-640.
29. Sabatier, P., *La catalyse en chimie organique*. Nouveau Monde éditions: 2014.
30. Zheng, Y.; Jiao, Y.; Jaroniec, M.; Qiao, S. Z., Advancing the electrochemistry of the hydrogen-evolution reaction through combining experiment and theory. *Angewandte Chemie International Edition* **2015,** *54* (1), 52-65.
31. Wang, J.; Xu, F.; Jin, H.; Chen, Y.; Wang, Y., Non-noble metal-based carbon composites in hydrogen evolution reaction: fundamentals to applications. *Advanced materials* **2017,** *29* (14), 1605838.
32. Kayhan, M. Transition Metal Borides: Synthesis, Characterization and Superconducting Properties. Technische Universität, 2013.
33. Ganem, B.; Osby, J. O., Synthetically useful reactions with metal boride and aluminide catalysts. *Chemical Reviews* **1986,** *86* (5), 763-780.
34. Givord, D.; Li, H.; De La Bâthie, R. P., Magnetic properties of Y2Fe14B and Nd2Fe14B single crystals. *Solid state communications* **1984,** *51* (11), 857-860.
35. Kanatzidis, M. G.; Pöttgen, R.; Jeitschko, W., The metal flux: a preparative tool for the exploration of intermetallic compounds. *Angewandte Chemie International Edition* **2005,** *44* (43), 6996-7023.
36. Park, H.; Zhang, Y.; Lee, E.; Shankhari, P.; Fokwa, B. P., High-Current-Density HER Electrocatalysts: Graphene-like Boron Layer and Tungsten as Key Ingredients in Metal Diborides. *ChemSusChem* **2019,** *12* (16), 3726-3731.
37. Chen, Y.; Yu, G.; Chen, W.; Liu, Y.; Li, G.-D.; Zhu, P.; Tao, Q.; Li, Q.; Liu, J.; Shen, X., Highly active, nonprecious electrocatalyst comprising borophene subunits for the hydrogen evolution reaction. *Journal of the American Chemical Society* **2017,** *139* (36), 12370-12373.

Chapter 2.

Unexpected Correlation Between Boron Chain Condensation and Hydrogen Evolution Reaction (HER) Activity in Highly Active Vanadium Borides : Enabling Predictions

In this chapter, we show for the first time that VB and V_3B_4 have high electrocatalytic HER activity. Furthermore, we show that the HER activity (in 0.5 M H_2SO_4) increases with increasing boron chain condensation in vanadium borides: Using a -23 mV overpotential decrement derived from -0.296 mV (for VB at -10 $mAcm^2$ current density) and -0.273 mV (for V_3B_4), we accurately predict the overpotential of VB_2 (-0.204 mV) as well as that of unstudied V_2B_3 (-0.250 mV) and hypothetical "V_5B_8" (-0.227 mV). We then derived an exponential equation that predicts the overpotentials of known and hypothetical V_xB_y phases containing at least a boron chain. These results provide a direct correlation between crystal structure and HER activity, thus paving the way for the design of even better electrocatalytic materials through structure-activity relationships.

***E. Lee**, H. Park, H. Joo, and B. P.T. Fokwa, **Angew. Chem. Int. Ed. 2020, 59, 11774 – 11778** (10.1002/anie.202000154)*

2.1. Introduction

Concerns about severe environmental issues and rapid fossil fuel depletion have triggered global efforts to develop clean and sustainable alternative energy sources. Hydrogen is a promising fuel because of its broad applications, easiness of produce, and much higher energy density than that of many other fuels such as methane.[1-3] There are three main technologies for producing H_2: coal gasification, methane reforming, and electrochemical water splitting.[4] Although coal gasification and methane reforming generate the most hydrogen, its exhaust gas such as carbon dioxide inevitably brings about air pollution and global warming. Therefore, electrochemical water splitting, through hydrogen evolution reaction (HER), is the best prospect to produce hydrogen.[5-8] Although, Platinum group metals have been the most active HER catalysts to date, their scarcity and high cost represent major issues that should be addressed for large-scale application.[9]

Low-cost HER electrocatalysts, such as transition metal carbides[10-11], chalcogenides[12-14], and phosphides[15-16] have been widely studied as substitutes for precious metal electrocatalysts. Transition metal borides(TMBs) have emerged as promising HER electrocatalysts because of their low cost, a high activity already in bulk form, and stability in both acidic and basic electrolytes.[17-21] Furthermore, their various compositions and crystal structures (depending on the boron substructures such as various chains or sheets)[22-23] coupled with their competitive activity in the bulk make them suitable for studying structure-activity relationships. For example, our group has recently reported that molybdenum borides show increased HER activity with increasing

boron content from Mo_2B (less active) to MoB_2 (most active).[24] Furthermore, we have also shown that different boron layers in molybdenum borides can affect their HER activity. In fact, our experiments and DFT calculations show that hexagonal AlB_2-type MoB_2 (containing graphene-like flat boron layers) is more active than rhombohedral MoB_2 (containing both flat and puckered phosphorene-like boron layers) due to intrinsically higher activity of the flat boron layers compared to the puckered ones.[25] These findings point to the crucial role of boron in the HER activity of TMBs and thus can be used to study the structure-activity relationships in these materials. Besides MoB_2, other highly active HER electrocatalysts with the AlB_2-type structure such as FeB_2 (in alkaline solution)[17] and VB_2 (in acid solution)[26] were recently reported.

Vanadium borides are very interesting materials, which have been studied in the last few decades for their mechanical hardness[27-28] and as anodes for non-rechargeable batteries[29-31]. Following the discovery of highly HER active VB_2, we report in the present work on two very active new members of the vanadium-boron system (VB and V_3B_4). Importantly, we show that the high activity of VB_2 can be rationalized by studying the effect of aggregating boron chains as a function of HER activity in vanadium borides. The HER activity is found to increase with boron chain aggregation from a single chain in VB to a double chain (or chain of hexagons) in V_3B_4 and to layers (infinite chain aggregation) VB_2 (cf. crystal structures in **Figure 2.1**).

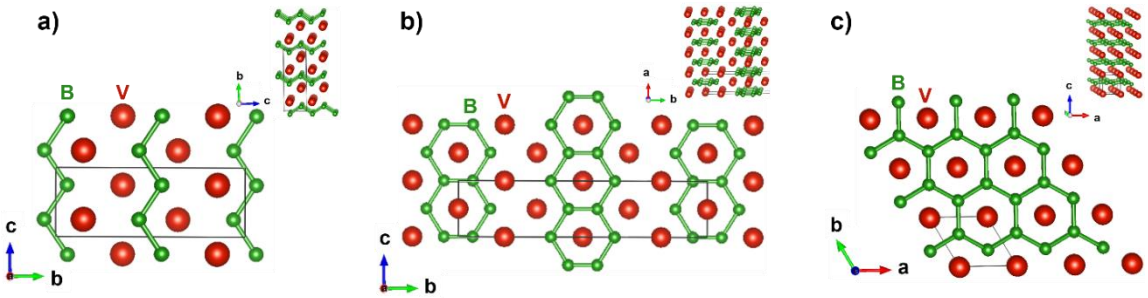

Figure 2.1. Projections of the crystal structures of (a) VB (CrB-type structure, *Cmcm*), (b) V_3B_4 (Cr_3B_4-type structure, *Immm*) and (c) VB_2 (AlB_2-type layered structure, *P6/mmm*).

2.2. Experimental Section

2.2.1. Sample preparation

An appropriate amount of vanadium (V) powder and boron (B) powder (total mass 0.2 g, atomic ratio of 1:1.2 for VB, 1:1.5 for V_3B_4, and 1:2.2 for VB_2) were weighed, mixed, and pressed into pallets. The pellets were melted in a copper crucible, which is cooled by water, using a tungsten tip at 40 A current under an argon atmosphere until homogeneous melting occurred.

2.2.2. Electrode preparation

1 mg of 20% Pt/C powder was sonicated in 95 µl IPA and 5 µl Nafion solution. Then, the 7.5 µl of the solution was dropwise on carbon cloth (0.5×0.5 cm^2). The carbon cloth was dried for 5 h at 50 °C in an oven (the catalyst loading: ~0.3 mg/cm^2). The dried carbon cloth was attached to a copper sheet using conductive silver paste. The exposed surface of the copper sheet was covered with epoxy adhesive and dried overnight at room temperature.

Arc-melted samples of the vanadium borides and elemental vanadium were put into the epoxy adhesive and dried overnight at room temperature. The top and bottom of the dried samples were ground using a grinder (South Bay Technology, USA) until it forms a disk shape. The ground samples were attached to the copper sheet using conductive silver paste. The exposed surface of the copper sheet was covered with epoxy adhesive and dried overnight at room temperature.

2.3. Results and Discussion

The three phases were successfully synthesized by the arc melting according to the detailed procedures given in the sample preparation method. As shown by the powder X-ray diffraction (PXRD) patterns in **Figure 2.2** and **Table 2.1**, the diffraction peaks and refined lattice parameters of all samples matched very well with reported data for VB (CrB-type structure, space group *Cmcm*),[32] V_3B_4 (Cr_3B_4-type structure, *Immm*),[33] and VB_2 (AlB_2-type layered structure *P6/mmm*).[34] However, some impurity phases were initially observed in the PXRD patterns (**Figure 2.2**): The VB and VB_2 samples contain ca. 3 wt. % V_4O_9 impurity, while the V_3B_4 sample contains ca. 5.2 wt. % VB and 7.8 wt. % V_4O_9 (**Table 2.1**). To purify these samples, we have treated them with a 0.5 M H_2SO_4 solution for 3 h (the same conditions were used for the electrochemical measurements below). Interestingly, in the PXRD patterns of the purified samples (**Figure 2.2**) no peaks of V_4O_9 were visible as confirmed by the Rietveld refinement data (**Table 2.1**), indicating that V_4O_9 has been dissolved by the acid. However, the peaks of the VB impurity (5.7 wt. %) remained in the PXRD pattern of the V_3B_4 sample, thus confirming the stability of

borides under these conditions. Nevertheless, the amount of VB impurity is too small to significantly affect the HER activity of V_3B_4. The elemental composition and sample homogeneity were studied by energy-dispersive X-ray spectroscopy (EDX) and EDX mapping (**Figure 2.3**) showing that V and B are uniformly distributed over the samples indicating good homogeneity.

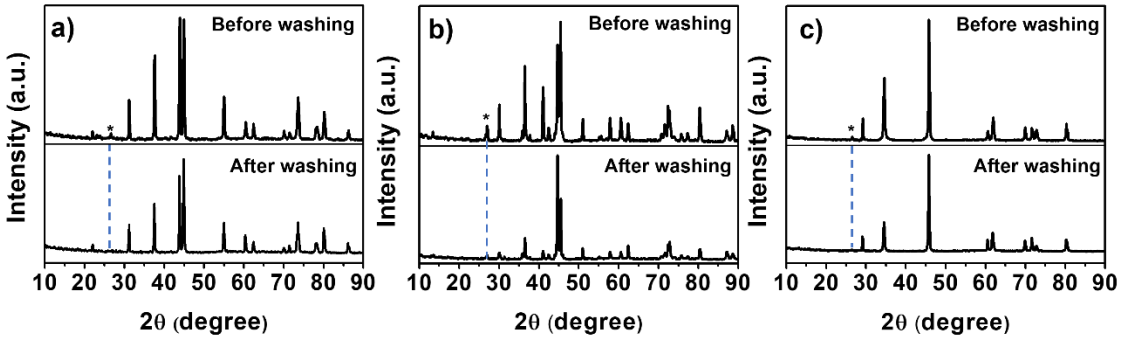

Figure 2.2. Powder X-ray diffraction patterns of (a) VB, (b) V_3B_4, and (c) VB_2 before and after washing with 0.5 M H_2SO_4 for 3 h.

Table 2.1. Rietveld refinement results of the PXRD data for the vanadium boride samples obtained before and after acid washing. The reported lattice parameters from the ICSD database are given in square brackets.

Phase	**VB**	**After washing**
Crystal system	Orthorhombic	Orthorhombic
Space group	*Cmcm*	*Cmcm*
a [Å]	3.059(4)-[3.100]	3.061(1)-[3.100]
b [Å]	8.04(1)-[8.170]	8.045(1)-[8.170]
c [Å]	2.972(4)-[2.980]	2.973(1)-[2.980]
V [Å^3]	73.1(2)-[75.47]	73.19(1)-[75.47]
Calc. density [g/cm^3]	5.605	5.604
Main phase (VB) [wt.-%]	96.78	99.95
Impurity (V_4O_9) [wt.-%]	3.22	0.05
Phase	**V_3B_4**	**After washing**
Crystal system	Orthorhombic	Orthorhombic
Space group	*Immm*	*Immm*
a [Å]	3.061(5)-[3.030]	3.057(8)-[3.030]
b [Å]	13.23(2)-[13.18]	13.22(4)-[13.18]
c [Å]	2.982(4)-[2.986]	2.978(8)-[2.986]
V [Å^3]	120.6(3)-[119.2]	120.3(6)-[119.2]
Calc. density [g/cm^3]	5.392	5.413
Main phase (V_3B_4) [wt.-%]	86.95	91.72
Impurity (VB) [wt.-%]	5.25	5.67
Impurity (V_4O_9) [wt.-%]	7.80	2.61
Phase	**VB_2**	**After washing**
Crystal system	Hexagonal	Hexagonal
Space group	*P6̄/mmm*	*P6̄/mmm*
a [Å]	2.997(6)-[3.006]	2.997(8)-[3.006]
c [Å]	3.057(8)-[3.058]	3.057(1)-[3.058]
V [Å^3]	23.77(9)-[23.69]	23.77(1)-[23.69]
Calc. density [g/cm^3]	5.068	5.067
Main phase (VB_2) [wt.-%]	96.50	99.49
Impurity (V_4O_9) [wt.-%]	3.50	0.51

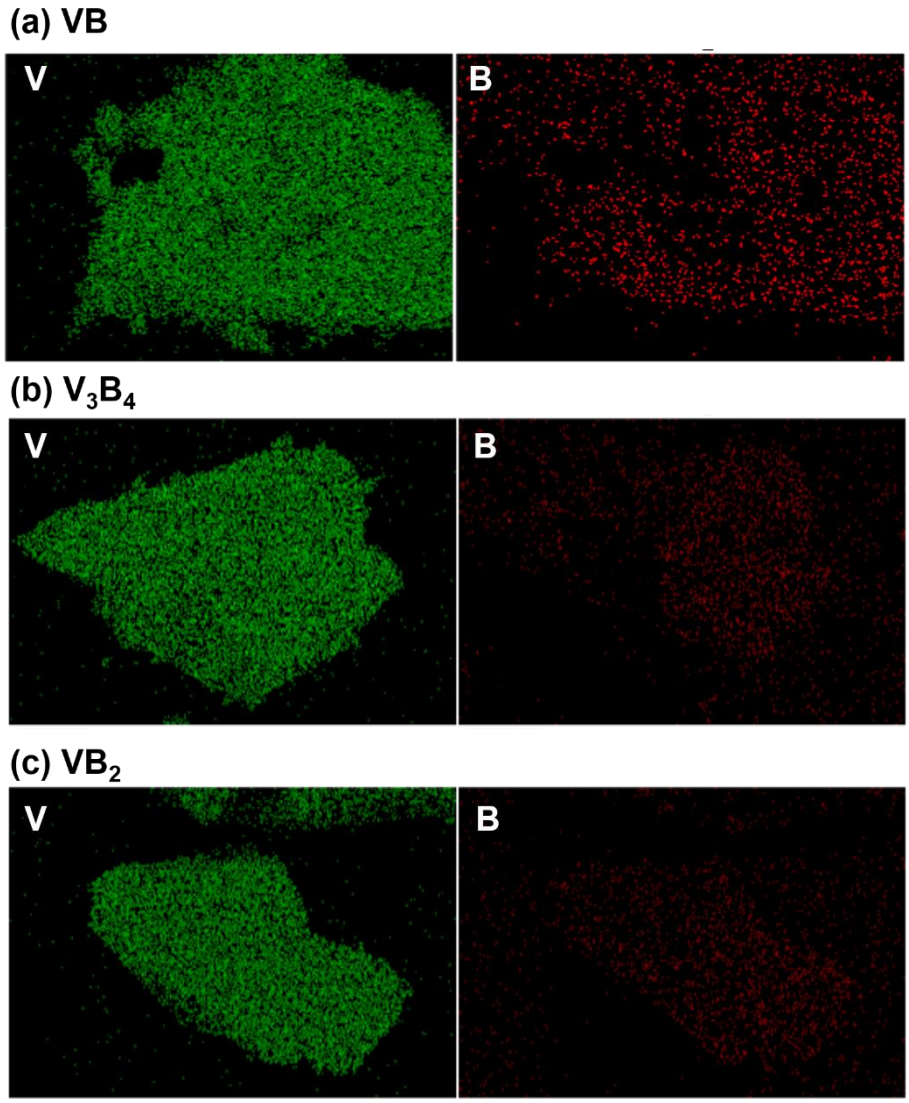

Figure 2.3. EDX mapping of (a) VB, (b) V_3B_4, and (c) VB_2

X-ray photoelectron spectroscopy (XPS) was used to characterize the surface species. As shown in **Figure 2.4(a-c),** the V 2p spectrum of each vanadium boride sample could be decomposed into V $2p_{1/2}$ and V $2p_{3/2}$ due to the spin-orbit peak splitting.[35-36] Each V 2p spectrum was then deconvoluted into three peaks corresponding to V^0 in vanadium boride, as well as V^{2+} and V^{4+} in vanadium oxide.[35-36] Furthermore,

Figure 2.4(d-f) shows the B 1s spectrum of all samples, and it was deconvoluted into two peaks corresponding to B^0 in vanadium boride and B^{3+} which is attributed to B_2O_3.[37] These XPS results reveal that the surfaces of the synthesized bulk vanadium borides are contaminated by boron and vanadium oxide species due to exposure in air.[38] However, both V^0 and B^0 peaks have by far the highest intensities, suggesting that the vanadium boride dominates the surface in all cases. Furthermore, the oxides of vanadium are soluble in 0.5 M H_2SO_4 (electrochemical measurement condition) as found during the purification step of the borides (see synthesis section above) and supported by previous observations,[39] thus it is expected that the active species during HER will be V^0 and B^0.

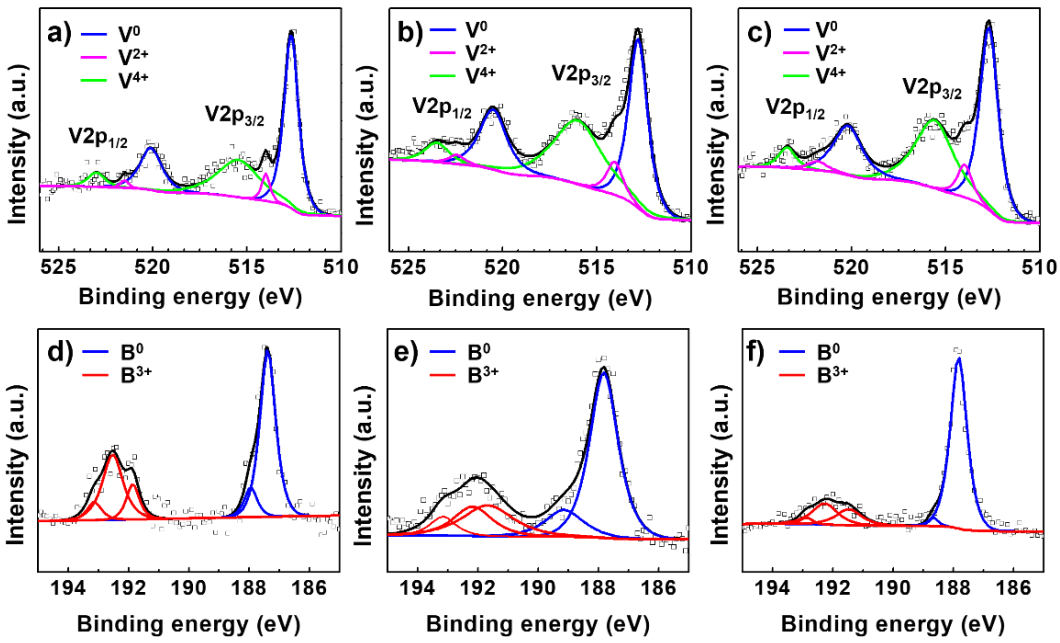

Figure 2.4. X-ray photoelectron spectroscopy spectra of V 2p and B 1s of VB (a, d), V_3B_4 (b, e), and VB_2 (c, f). Experimental and fitting data are indicated as (□) and solid lines, respectively.

For electrochemical measurements, we have used a typical three-electrode system which is composed of the counter electrode (graphite rod), reference electrode (saturated calomel electrode), and the working electrode (polished dense sample). **Figure 2.5a** shows the *iR*-corrected polarization curves of VB, V_3B_4, and VB_2 recorded at a scan rate of 5 mV/s in 0.5 M H_2SO_4. For comparison, the HER activity of 20 % Pt/C and bulk elemental vanadium and boron were also investigated under the same conditions. The resulting linear sweep voltammetry (LSV) shows that nanoscale Pt/C has the best HER performance as expected, while bulk V and B have the worse activities. Nevertheless, V has a significantly better HER activity than B, suggesting that a high vanadium content in vanadium borides may be advantageous. However, the opposite trend is found: The V-richer VB has the lowest activity with the highest overpotential (-0.296 V vs. RHE to drive a current density of -10 mA/cm^2) which then decreases to -0.273 V for V_3B_4 and then to -0.204 V for the V-poorest VB_2. These results are also supported by electrochemical impedance spectroscopy (EIS) measurements given in **Figure 2.5c.** The EIS (or Nyquist) plot, which is related to the charge transfer resistance, has a semicircular diameter for all vanadium borides (**Figures 2.5c**) indicating their fast transfer abilities. The charge transfer resistance (R_{ct}) derived from the Nyquist plot fitting increases as the vanadium content increases, which is counterintuitive as one would have expected a decrease of resistance with increasing vanadium (metal) content. In fact, R_{ct} dramatically increases by threefold (or 290%) from 43.37 Ω in VB_2 to 125.7 Ω inV_3B_4, implying a huge decrease in charge transferability as the V-content increases, then it further

decreases but by only 27 % from 125.7 Ω in V_3B_4 to 172.0 Ω in VB. This trend is the same as that found through the polarization analysis above.

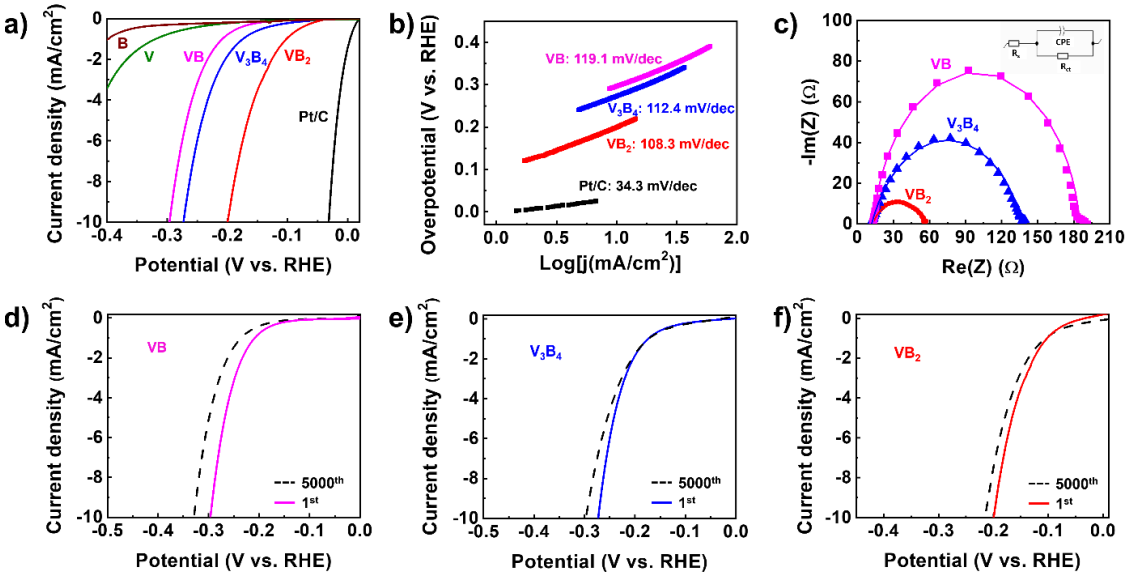

Figure 2.5. (a) Polarization curves of various materials were recorded in 0.5 M H_2SO_4 at a scan rate of 5 mV/s with *iR*-correction. (b) Tafel plots were obtained using the polarization curves in (a). (c) Electrochemical impedance spectra (Nyquist plots): The points represent the experimental data and the solid lines indicate the fitting line. Polarization curves of (d) VB, (e) V_3B_4, and (f) VB_2 were recorded in 0.5 M H_2SO_4 at a scan rate of 5 mV/s (with *iR*-correction) after the first and 5000 CV cycles at a scan rate of 100 mV/s.

Insights into the HER reaction mechanism on the catalyst's surface were provided by the Tafel plots given in **Figure 2.5b.** According to the HER mechanism in an acidic electrolyte, there are three possible reactions that can be the rate-determining step (RDS); Volmer reaction (Tafel slope ~120 mV/dec), Heyrovsky reaction (Tafel slope ~40 mV/dec), and Tafel reaction (Tafel slope ~30 mV/dec).[40-41] Analysis of our Tafel plots yielded the following Tafel slopes: 34.3, 119.1, 112.4, and 108.3 mV/dec for Pt/C, VB, V_3B_4, and VB_2, respectively. Pt/C's Tafel slope value suggests the Tafel reaction as the

RDS, as expected. The Tafel slope value of VB matches the theoretical Tafel slope of the Volmer reaction, indicating that the Volmer reaction is likely the RDS. While the Tafel slope values of V_3B_4 and VB_2 are still closer to that of the Volmer reaction, they significantly deviate (8 and 12 mV/dec less, respectively) from the theoretical value, indicating a more complex mechanism for V_3B_4 and VB_2. VB_2 has the lowest Tafel slope value, which indicates a more efficient HER process, followed by V_3B_4 and then VB, which is the least efficient, a further confirmation of decreasing activity with increasing V-content.

To assess the durability of the vanadium boride electrocatalysts in the acidic electrolyte, we have conducted a stability test using CV measurements. According to the measurements, even after 5000 CV cycles (**Figure 2.5d-f**), the overpotential of VB, V_3B_4, and VB_2 required to achieve 10 mA/cm^2 current density increased only by 33, 24, and 11 mV, respectively. The increased overpotential is more pronounced as the V-content increases, which hints at increased corrosion of the samples' surface as the amount of metal component (vanadium) increases. Nevertheless, all catalysts remained very active after 5000 cycles and are thus durable in acidic electrolytes.

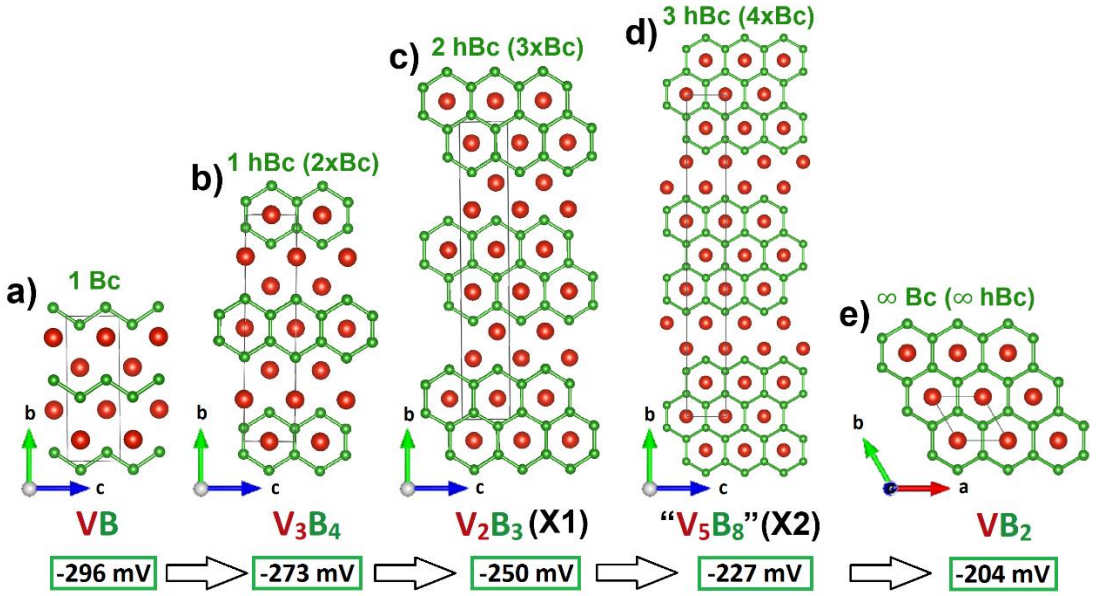

Figure 2.6. Projections of the crystal structures of (a) VB (CrB-type structure, *Cmcm)*, (b) V_3B_4 (Cr_3B_4-type structure, *Immm*), (c) V_2B_3 (space group *Cmcm*), and (e) VB_2 (AlB_2-type layered structure, *P6/mmm*). (d) The crystal structure of hypothetical "V_5B_8" is predicted to have 3 hexagonal boron chains: Bc = boron chain; hBc = hexagonal boron chain.

Figure 2.6a shows a large gap (difference of 92 mV) between the overpotentials of VB_2 and V_3B_4, while the gap is significantly smaller (difference of 23 mV) between those of V_3B_4 and VB. This trend shows that there is a much closer relationship between VB and V_3B_4 than between VB_2 and V_3B_4. Let's examine what factors play a role in this trend. We have shown above already that the V-content would have predicted the opposite trend, thus boron should be mainly responsible for this trend. Indeed, analyzing the trend in boron content reveals a 2B increment between VB_2 (or "V_3B_6") and V_3B_4, while only a 1B increment exists between VB (or "V_3B_3") and V_3B_4, thus it mimics the activity trend but does not exactly since this would imply a 2x larger overpotential difference (i.e. only 2 x 23 mV = 46 mV instead of 92 mV) for the larger overpotential

gap. Therefore, the change in boron content alone cannot justify this trend. Trying to fill this large overpotential gap with potential phases, we assumed a 23 mV increment, which led to the following result: -296 mV (VB), -273 mV (V_3B_4), -250 mV (X1), -227 mV (X2), and -204 mV (VB_2). First, it is astonishing that the correct overpotential of VB_2 is accurately predicted this way, second, the overpotentials of two unknown phases (X1 and X2) are also predicted. A closer look at the boron substructures in the V-B system reveals a direct correlation with the activity trend. In fact, the boron substructures between V_3B_4 and VB_2 (**Figure 2.6**) can be reconstructed based on the condensation of the zigzag boron chain (Bc) present in VB: 2 x Bc gives the hexagonal boron chain (hBc) in V_3B_4, 3 x Bc leads to the 2 hBc in V_2B_3, 4 x Bc accounts for the still unknown 3 hBc that we predict to exist in the hypothetical phase "V_5B_8" using structural analogies with the known V_xB_y structures (**Figure 2.6**). Therefore, matching these compositions with the above-predicted HER activities leads to X1 = V_2B_3 and X2 = "V_5B_8". The fourth and last step is an infinite Bc condensation which leads to VB_2 (boron layer), thereby suggesting that a phase containing more than 3 hBc units will likely be as active as VB_2. Given that the last step is disproportionately larger (infinite) than the previous steps, we have derived (using the experimental overpotentials) an exponential equation (1) that accurately predicts the overpotential (η) at -10 mA/cm^2 of vanadium boride phases based on a variable *n (1,2,…∞),* which is the ratio of the number of 3-bonded to that of 2-bonded boron atoms in the unit cell (see **Table 2.2**).

$$\eta(mV) = -90e^{-0.25n} - 205 \qquad (1)$$

Interestingly, equation (1) can also be used to predict the overpotential of V_5B_6, the structure (**Figure 2.7**) of which contains a hybrid boron substructure (1 Bc + 1 hBc), hinting at potentially unknown hybrid structures (n = 1.5, 2.5…) with higher HER activities. The synthesis of V_5B_6 and V_2B_3 with high enough purity for HER analysis is still in progress, while the hypothetical "V_5B_8" is still elusive.

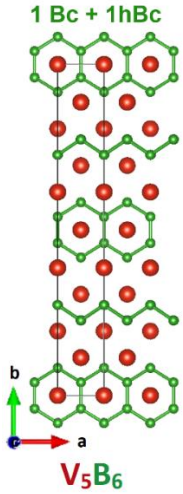

Figure 2.7. Projections of the crystal structure of V_5B_6 (space group *Cmmm*). Boron build a hybrid substructure composed of Bc (as in VB) and hBC (as in V_3B_4).

Table 2.2. Calculated *n* values of the vanadium borides and their experimental and predicted overpotential values (based on the equation $\eta(mV) = -90e^{-0.25n} - 205$, where $n = n_3/n_2$). "V_5B_8" is a predicted phase.

Sample	VB	V_5B_6	V_3B_4	V_2B_3	"V_5B_8"	VB_2
n_3: # of 3 bonded boron atom in unit cell	0	4	4	8	12	2
n_2: # of 2 bonded boron atom in unit cell	4	8	4	4	4	0
n	**0**	**0.5**	**1**	**2**	**3**	∞
Experimental overpotential (mV)	-296	-	-273	-	-	-204
Predicted Overpotential (mV)	-295	-284	-275	-260	-248	-205

2.4. Conclusion

We have synthesized highly crystalline single phases of VB (CrB-type structure) and V_3B_4 (Cr_3B_4-type structure) by arc-melting and studied their HER activity for the first time. All studied phases have high electrocatalytic HER activities. Furthermore, a structure-activity relationship is found in the V-B system that helps to predict new phases, their structures, and HER overpotentials. This study will pave the way for the rational discovery of HER catalysts using structure-activity relationships.

2.5. References

1. Bard, A. J.; Fox, M. A., Artificial photosynthesis: solar splitting of water to hydrogen and oxygen. *Accounts of Chemical Research* **1995,** *28* (3), 141-145.
2. Chow, J.; Kopp, R. J.; Portney, P. R., Energy resources and global development. *Science* **2003,** *302* (5650), 1528-1531.
3. Turner, J. A., Sustainable hydrogen production. *Science* **2004,** *305* (5686), 972-974.
4. Thiyagarajan, N.; Joseph, N. A.; Gopinathan, M., Noble-Metal-Free Nanoelectrocatalysts for Hydrogen Evolution Reaction. In *Nanostructured Materials for Energy Related Applications*, Springer: 2019; pp 73-120.
5. Holladay, J. D.; Hu, J.; King, D. L.; Wang, Y., An overview of hydrogen production technologies. *Catalysis today* **2009,** *139* (4), 244-260.
6. Katsounaros, I.; Cherevko, S.; Zeradjanin, A. R.; Mayrhofer, K. J., Oxygen electrochemistry as a cornerstone for sustainable energy conversion. *Angewandte Chemie International Edition* **2014,** *53* (1), 102-121.
7. Vesborg, P. C.; Seger, B.; Chorkendorff, I., Recent development in hydrogen evolution reaction catalysts and their practical implementation. *The journal of physical chemistry letters* **2015,** *6* (6), 951-957.
8. Koper, M. T., Hydrogen electrocatalysis: A basic solution. *Nature chemistry* **2013,** *5* (4), 255.
9. Qin, Y.; Wu, H.-H.; Zhang, L. A.; Zhou, X.; Bu, Y.; Zhang, W.; Chu, F.; Li, Y.; Kong, Y.; Zhang, Q., Aluminum and nitrogen codoped graphene: Highly active and durable electrocatalyst for oxygen reduction reaction. *ACS Catalysis* **2018,** *9* (1), 610-619.
10. Chen, W.-F.; Muckerman, J. T.; Fujita, E., Recent developments in transition metal carbides and nitrides as hydrogen evolution electrocatalysts. *Chemical communications* **2013,** *49* (79), 8896-8909.
11. Ng, V. M. H.; Huang, H.; Zhou, K.; Lee, P. S.; Que, W.; Xu, J. Z.; Kong, L. B., Recent progress in layered transition metal carbides and/or nitrides (MXenes) and their composites: synthesis and applications. *Journal of Materials Chemistry A* **2017,** *5* (7), 3039-3068.
12. Chia, X.; Pumera, M., Layered transition metal dichalcogenide electrochemistry: journey across the periodic table. *Chemical Society Reviews* **2018**.
13. Lu, Q.; Yu, Y.; Ma, Q.; Chen, B.; Zhang, H., 2D Transition-metal-dichalcogenide-nanosheet-based composites for photocatalytic and electrocatalytic hydrogen evolution reactions. *Advanced Materials* **2016,** *28* (10), 1917-1933.
14. Jaramillo, T. F.; Jørgensen, K. P.; Bonde, J.; Nielsen, J. H.; Horch, S.; Chorkendorff, I., Identification of active edge sites for electrochemical H2 evolution from MoS2 nanocatalysts. *science* **2007,** *317* (5834), 100-102.
15. Pu, Z.; Amiinu, I. S.; Zhang, C.; Wang, M.; Kou, Z.; Mu, S., Phytic acid-derivative transition metal phosphides encapsulated in N, P-codoped carbon: an

efficient and durable hydrogen evolution electrocatalyst in a wide pH range. *Nanoscale* **2017,** *9* (10), 3555-3560.
16. Hong, H.; Liu, C.; Cao, T.; Jin, C.; Wang, S.; Wang, F.; Liu, K., Interfacial engineering of van der waals coupled 2D layered materials. *Advanced Materials Interfaces* **2017,** *4* (9), 1601054.
17. Li, H.; Wen, P.; Li, Q.; Dun, C.; Xing, J.; Lu, C.; Adhikari, S.; Jiang, L.; Carroll, D. L.; Geyer, S. M., Earth-Abundant Iron Diboride (FeB2) Nanoparticles as Highly Active Bifunctional Electrocatalysts for Overall Water Splitting. *Advanced Energy Materials* **2017,** *7* (17), 1700513.
18. Jothi, P. R.; Zhang, Y.; Scheifers, J. P.; Park, H.; Fokwa, B. P., Molybdenum diboride nanoparticles as a highly efficient electrocatalyst for the hydrogen evolution reaction. *Sustainable Energy & Fuels* **2017,** *1* (9), 1928-1934.
19. Xu, N.; Cao, G.; Chen, Z.; Kang, Q.; Dai, H.; Wang, P., Cobalt nickel boride as an active electrocatalyst for water splitting. *Journal of Materials Chemistry A* **2017,** *5* (24), 12379-12384.
20. Sun, H.; Meng, J.; Jiao, L.; Cheng, F.; Chen, J., A review of transition-metal boride/phosphide-based materials for catalytic hydrogen generation from hydrolysis of boron-hydrides. *Inorganic Chemistry Frontiers* **2018,** *5* (4), 760-772.
21. Vrubel, H.; Hu, X., Molybdenum boride and carbide catalyze hydrogen evolution in both acidic and basic solutions. *Angewandte Chemie International Edition* **2012,** *51* (51), 12703-12706.
22. Akopov, G.; Yeung, M. T.; Kaner, R. B., Rediscovering the crystal chemistry of borides. *Advanced Materials* **2017,** *29* (21), 1604506.
23. Albert, B.; Hillebrecht, H., Boron: elementary challenge for experimenters and theoreticians. *Angewandte Chemie International Edition* **2009,** *48* (46), 8640-8668.
24. Park, H.; Encinas, A.; Scheifers, J. P.; Zhang, Y.; Fokwa, B. P., Boron-dependency of molybdenum boride electrocatalysts for the hydrogen evolution reaction. *Angewandte Chemie International Edition* **2017,** *56* (20), 5575-5578.
25. Park, H.; Zhang, Y.; Scheifers, J. P.; Jothi, P. R.; Encinas, A.; Fokwa, B. P., Graphene-and phosphorene-like boron layers with contrasting activities in highly active Mo2B4 for hydrogen evolution. *Journal of the American Chemical Society* **2017,** *139* (37), 12915-12918.
26. Jothi, P. R.; Zhang, Y.; Yubuta, K.; Culver, D.; Conley, M. P.; Fokwa, B. P., Abundant vanadium diboride with graphene-like boron layers for hydrogen evolution. *ACS Applied Energy Materials* **2018**.
27. Wei, S.; Li, D.; Lv, Y.; Liu, Z.; Tian, F.; Duan, D.; Liu, B.; Cui, T., Strong covalent boron bonding induced extreme hardness of VB3. *Journal of Alloys and Compounds* **2016,** *688*, 1101-1107.
28. Bulfon, C.; Leithe-Jasper, A.; Sassik, H.; Rogl, P., Microhardness of Czochralski-grown single crystals of VB2. *Journal of Solid State Chemistry* **1997,** *133* (1), 113-116.

29. Stuart, J.; Lefler, M.; Rhodes, C. P.; Licht, S., High Energy Capacity TiB2/VB2 Composite Metal Boride Air Battery. *Journal of The Electrochemical Society* **2015,** *162* (3), A432-A436.
30. Licht, S.; Wu, H.; Yu, X.; Wang, Y., Renewable highest capacity VB 2/air energy storage. *Chemical Communications* **2008,** (28), 3257-3259.
31. Yu, X.; Licht, S., High capacity alkaline super-iron boride battery. *Electrochimica Acta* **2007,** *52* (28), 8138-8143.
32. Schob, O. t.; Parthé, E., AB compounds with Sc, Y and rare earth metals. I. Scandium and yttrium compounds with CrB and CsCl structure. *Acta Crystallographica* **1965,** *19* (2), 214-224.
33. Moskowitz, D., New Vanadium Boride of the Composition V 3 B 4. *JOM* **1956,** *8* (10), 1325-1325.
34. Post, B.; Glaser, F. W.; Moskowitz, D., Transition metal diborides. *Acta Metallurgica* **1954,** *2* (1), 20-25.
35. Wang, P.; Kumar, R.; Sankaran, E. M.; Qi, X.; Zhang, X.; Popov, D.; Cornelius, A. L.; Li, B.; Zhao, Y.; Wang, L., Vanadium diboride (VB2) synthesized at high pressure: elastic, mechanical, electronic, and magnetic properties and thermal stability. *Inorganic chemistry* **2018,** *57* (3), 1096-1105.
36. Biesinger, M. C.; Lau, L. W.; Gerson, A. R.; Smart, R. S. C., Resolving surface chemical states in XPS analysis of first row transition metals, oxides and hydroxides: Sc, Ti, V, Cu and Zn. *Applied Surface Science* **2010,** *257* (3), 887-898.
37. Terlan, B. r.; Levin, A. A.; Börrnert, F.; Simon, F.; Oschatz, M.; Schmidt, M.; Cardoso-Gil, R.; Lorenz, T.; Baburin, I. A.; Joswig, J.-O., Effect of surface properties on the microstructure, thermal, and colloidal stability of VB2 nanoparticles. *Chemistry of Materials* **2015,** *27* (14), 5106-5115.
38. Xiao, X.; Tao, L.; Li, M.; Lv, X.; Huang, D.; Jiang, X.; Pan, H.; Wang, M.; Shen, Y., Electronic modulation of transition metal phosphide via doping as efficient and pH-universal electrocatalysts for hydrogen evolution reaction. *Chemical science* **2018,** *9* (7), 1970-1975.
39. Toh, R. J.; Sofer, Z.; Pumera, M., Transition metal oxides for the oxygen reduction reaction: influence of the oxidation states of the metal and its position on the periodic table. *ChemPhysChem* **2015,** *16* (16), 3527-3531.
40. Chung, D. Y.; Park, S.-K.; Chung, Y.-H.; Yu, S.-H.; Lim, D.-H.; Jung, N.; Ham, H. C.; Park, H.-Y.; Piao, Y.; Yoo, S. J., Edge-exposed MoS 2 nano-assembled structures as efficient electrocatalysts for hydrogen evolution reaction. *Nanoscale* **2014,** *6* (4), 2131-2136.
41. Sheng, W.; Gasteiger, H. A.; Shao-Horn, Y., Hydrogen oxidation and evolution reaction kinetics on platinum: acid vs alkaline electrolytes. *Journal of The Electrochemical Society* **2010,** *157* (11), B1529-B1536.

Chapter 3.

Vacancy-Enhanced Hydrogen Evolution in Extraordinarily High Current Density-performing $V_{1-x}Mo_xB_2$ Solid Solution

Revealing the structure-activity relationships of materials is an important factor in our quest to replace platinum-based hydrogen evolution reaction (HER) electrocatalysts with non-noble metal ones. Herein, the full solid solution range of $V_{1-x}Mo_xB_2$ (x = 0 - 1) has been synthesized and we discovered an outlier trend of the *c* lattice parameter, a volcano-like shape where *c* first increases with x reaching a maximum at x = 0.7 ($V_{0.3}Mo_{0.7}B_2$) then decreases. DFT calculations show that this interesting trend is caused by the presence of strong antibonding metal-boron interactions at the Fermi level of metal-deficient samples. The metal vacancy affects not only the *c* lattice parameter but also the HER activity. As x increases, the HER activity also increases, peaking at $V_{0.3}Mo_{0.7}B_2$ (η_{150} = 0.243 V) and then decreasing. Moreover, at a high current density of 1000 mA/cm^2, $V_{0.3}Mo_{0.7}B_2$ requires the overpotential of 0.391 V which is far less than that of Pt/C (η_{1000}= 0.837 V). Besides, it has outstanding long-term stability without any degradation for 24 h operation at 12 mA/cm^2 and after 5000 CV cycles. This study offers new avenues for designing abundant high-current-density HER electrocatalysts and emphasizes the key role of structure-activity relationships.

3.1. Introduction

The production of hydrogen from electrochemical water splitting through the hydrogen evolution reaction (HER) is a promising method to replace the current carbon-based fuels. One of the merits of water splitting is that hydrogen can be produced by various renewable resources such as wind, solar, and geothermal which means that it is the ultimate eco-friendly method.[1-2] Moreover, hydrogen can be used in high-efficiency power generation systems for fuel cells due to its high energy density.[3-5] For these reasons, related research is being actively conducted in various fields. However, there are numerous obstacles to enabling a replacement of fossil fuel with hydrogen due to the high cost of hydrogen production. The most active catalysts for HER found so far are platinum-based catalysts, however, they are too expensive to be used in the industry.[6-8] Therefore, research on non-noble metal-based electrocatalysts is required.

To discover the new electrocatalysts for replacing platinum-based catalysts, revealing the structure-activity relationship of materials is important to design optimal electrocatalysts. Recently, transition metal borides (TMBs) have been the focus of such studies due to their various crystal structures. For instance, AlB_2-type MoB_2 containing flat boron layers (α-MoB_2) shows higher HER activity than rhombohedral MoB_2 (β-MoB_2) containing both flat and puckered boron layers. This is because the intrinsic activity of flat boron layers based on DFT calculation is higher than that of puckered boron layers.[9] This concept is further applied to the V-B system. We found a relationship between the boron chain condensation in vanadium borides and HER activity, which made it possible to predict the activity of new V_xB_y catalysts.[10] Beyond the binary

systems, ternary diborides also show meaningful results. Firstly, α-MoB_2 is a better catalyst than WB_2, though elemental W has better activity than elemental Mo.[11] This is because WB_2 contains the puckered boron layer (the same boron structure as β-MoB_2) which has a worse activity than the flat boron layer. To take advantage of the higher activities of elemental W and the flat boron layer structure, W was added to the α-MoB_2 structure. As a result, α-$Mo_{0.7}W_{0.3}B_2$ containing the flat boron layer showed the best activity among the $Mo_{1-x}W_xB_2$ ($0 \leq x \leq 0.3$) samples. These data clearly showed the crucial role of the boron layer in HER activity. Furthermore, Cr was used instead of W to make a full solid solution range of $Cr_{1-x}Mo_xB_2$ because CrB_2 and MoB_2 have the same AlB_2-type structure.[12] The range of solid solution ($0 \leq x \leq 1$) showed an unexpected canonic-like (or volcano-like) behavior of the *c* lattice parameter, which was also perfectly matched by the HER activity. The peak activity found for $Cr_{0.4}Mo_{0.6}B_2$ with the largest *c* lattice parameter, thus emphasizing the importance of structure-activity relationships in designing highly active electrocatalysts.

Following the above studies on VB_2, which just like α-MoB_2, has higher HER activity than CrB_2, the study of $V_{1-x}Mo_xB_2$ solid solution as HER electrocatalyst was the next obvious target: We hypothesize that the high HER activity of VB_2 and its larger *c* lattice parameter if compared to those of CrB_2, will lead to a highly active $V_{1-x}Mo_xB_2$ solid solution. Herein, we present the experimental and computational investigations of the full solid solutions of $V_{1-x}Mo_xB_2$ and complete structural investigations including metal vacancy analysis and HER activity. As we will demonstrate below, control over the crystal and electronic structures and defects has led to the design of an incredibly robust

bulk HER electrocatalyst that significantly outperforms nanoscale Pt/C at high current density.

3.2. Experimental Section

3.2.1. Sample preparation

Molybdenum (powder, 99.95 %), vanadium (powder, 99.95 %), boron (amorphous powder, 99 %), Pt/C (20 %), and Nafion (5%) were obtained from Alfa Aesar. Sulfuric acid (H_2SO_4, 98 %) was purchased from Fisher Scientific. Copper sheets and conductive silver glue were supplied by Basic copper and Ted Pella, respectively. All of the chemicals were used without further purification. In order to synthesize $V_{1-x}Mo_xB_2$, appropriate amount of vanadium (V), molybdenum (Mo), and boron (B) powder (total mass 0.3 g, x=0.1, 0.3, 0.5, 0.7, and 0.9) were weighed, mixed and pressed into pellets. The pellets were arc melted in a copper crucible, which is cooled by water, using a tungsten tip at 50 A current under an argon atmosphere until homogeneous melting occurred.

3.2.2. Electrode preparation

Electrode preparation of $V_{1-x}Mo_xB_2$: Arc-melted $V_{1-x}Mo_xB_2$ sample was put into the epoxy adhesive and dried overnight at room temperature. The top and bottom of the dried samples were ground using a grinder (South Bay Technology, USA) until it forms a disk shape. The ground samples were attached to a copper sheet using conductive silver paste. The exposed surface of the copper sheet was covered with epoxy adhesive and dried overnight at room temperature.

Electrode preparation of Pt/C: 1 mg of 20% Pt/C powder was sonicated in 95 µl IPA and 5 µl Nafion solution. Then, the 3.0 µl of the solution was dropwise on carbon cloth (0.3×0.3 cm^2). The carbon cloth was dried for 5 h at 50 °C in an oven (the catalyst loading: ~0.3 mg/cm^2). The dried carbon cloth was attached to the copper sheet using a conductive silver paste. The exposed surface of the copper sheet was covered with epoxy adhesive and dried overnight at room temperature.

3.3. Computational Details

General Settings: The density functional theory (DFT) was used on all the modeled bulk structures of $V_xMo_{1-x}B_2$ for the DOS, COHP, and surface structures of the solid solution to determine the H-binding energy (ΔE_H). The total energy calculations were done using the projector augmented wave[13]coded in the Vienna ab initio simulation package (VASP).[14] In addition, all the VASP calculations done here employed the generalized gradient approximation (GGA) with the exchange and correlation functionals treated by the Perdew-Burke-Enzerhoff (PBE)[15] method for structure relaxations and single-point energy calculations of the bulk models and revised PBE[16] method for the single-point energy calculations of surface models. The convergence threshold for the ionic relaxation loop was set to 0.02 eV/Å in force and the cutoff energy for the plane wave calculations was set to 500 eV. The Brillouin zone integrations were carried a k-point mesh density of 0.0167 points $Å^{-1}$ using the Monkhorst-Pack automatic grid generation mode.

DOS and COHP: For the DOS and COHP calculations, the Local-Orbital Basis Suite Towards Electronic-Structure Reconstruction (LOBSTER) program[17] was used. As for the computational settings the energy range analyzed relative to the Fermi level was between -16 to 9 eV with interactions generated with atoms between 1.5 to 4.0 Å. The basis set used was the pbeVaspFit2015 with basis sets with the following basic functions: 5s, 4d, and 4p for Mo. 4s, 3d, and 3p, for V. 2s and 2p for B. As for the DFT computational settings used here, the tetrahedron method with Blöchl corrections and smearing value of 0.2 eV was done to treat partial occupancies. A 2 x 2 x 2 supercell was used with 3 metal layers with a total of 8 metal sites (Mo or V) and 2 boron layers, the k-point mesh grid used was 11 x 11 x 11. For the Mo deficient MoB_2 and $V_{0.25}Mo_{0.75}B_2$ models, random metal sites were allocated to either Mo or V to the correct chemical formula ratio while for metal deficient models a random Mo site in the models was removed leading to a vacancy value of 12.5% (1/8 metal sites unoccupied) leading to compounds with the chemical formula $Mo_{0.875}B_2$ and $V_{0.25}Mo_{0.625}B_2$.

HER & H-Coverage: We begin constructing the surfaces In this work, by cleaving the bulk $Mo_{0.875}B_{2.00}$ and $V_{0.250}Mo_{0.626}B_2$ into 2-dimensional (2D) slabs with the mixed [110] layer exposed at both the top and bottom and then about 15 Å of vacuum space was added in the [110] direction for the supercells to ensure that there would be no inter-slab interaction which resulted in a surface slab. During the structural relaxation step, the cell shape and volume were kept frozen while the positions of all the atoms were allowed to move and the lattice parameters were allowed to change. To calculate the

hydrogen coverage on the surfaces, the number of H atoms adsorbed on the surface by half the number of B atoms.

To calculate the Gibbs free energy (ΔG_H) for H adsorption to predict the HER activity of the different HER active sites on the surface the equation $\Delta G_H = \Delta E_H + \Delta E_{ZPE} - T\Delta S$ was used, where ΔE_H is the H-surface binding energy computed using DFT, ΔE_{ZPE} is the zero-point energy difference between adsorbed H and free H_2 and $T\Delta S$ is the temperature and entropy contribution terms. ΔE_{ZPE} is usually very small, between 0.01 to 0.05 eV[5] which is around or less than the chemical accuracy target of $1\ kcal \cdot mol^{-1}$ or 0.043 eV that is desired for ab initio computational methods, so it can be neglected here and the equation can be simplified to $\Delta G_H = \Delta E_H - T\Delta S$. Here $T\Delta S$ is calculated with the approximation, $T\Delta S \approx \frac{1}{2} TS°(H_2)$ where $T = 298.15\ K$ and $S°(H_2) = 130.7\ J \cdot mol^{-1}\ k^{-1}$.[15] Lastly, the equation used to solve for the binding energy of hydrogen ΔE_H was $\Delta E_H = E[surface + nH] - E[surface + (n-1)H] - \frac{1}{2}E[H_2]$. and $E[surface + nH]$ $E[surface + (n — 1)H]$ are the total energies of the surface with n and $n-1$ hydrogen atoms adsorbed on it respectively and calculated using VASP, and $\frac{1}{2}E[H_2]$ is half of the energy of one gas phase, a diatomic hydrogen molecule.

3.4. Results and Discussion

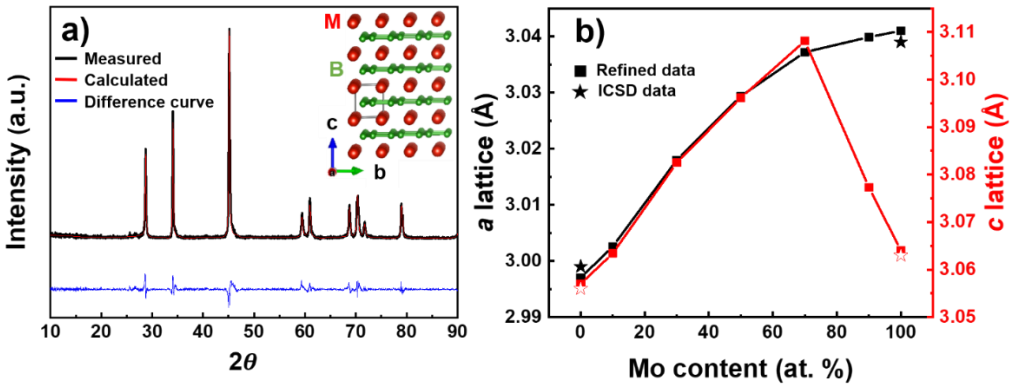

Figure 3.1. a) Refined powder XRD pattern of $V_{0.3}Mo_{0.7}B_2$, inset: Projection of the crystal structure of MB_2 (M=V and Mo, B=boron), b) plot of refined *a* and *c* lattice parameters of $V_{1-x}Mo_xB_2$ as a function of the molybdenum content

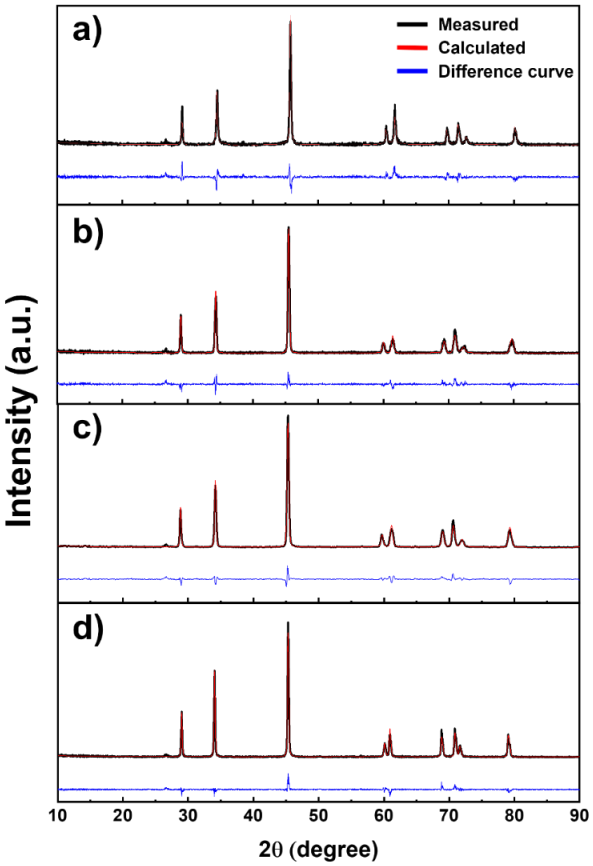

Figure 3.2. Refined powder X-ray diffraction data of a) $V_{0.9}Mo_{0.1}B_2$, b) $V_{0.7}Mo_{0.3}B_2$, c) $V_{0.5}Mo_{0.5}B_2$, and d) $V_{0.1}Mo_{0.9}B_2$.

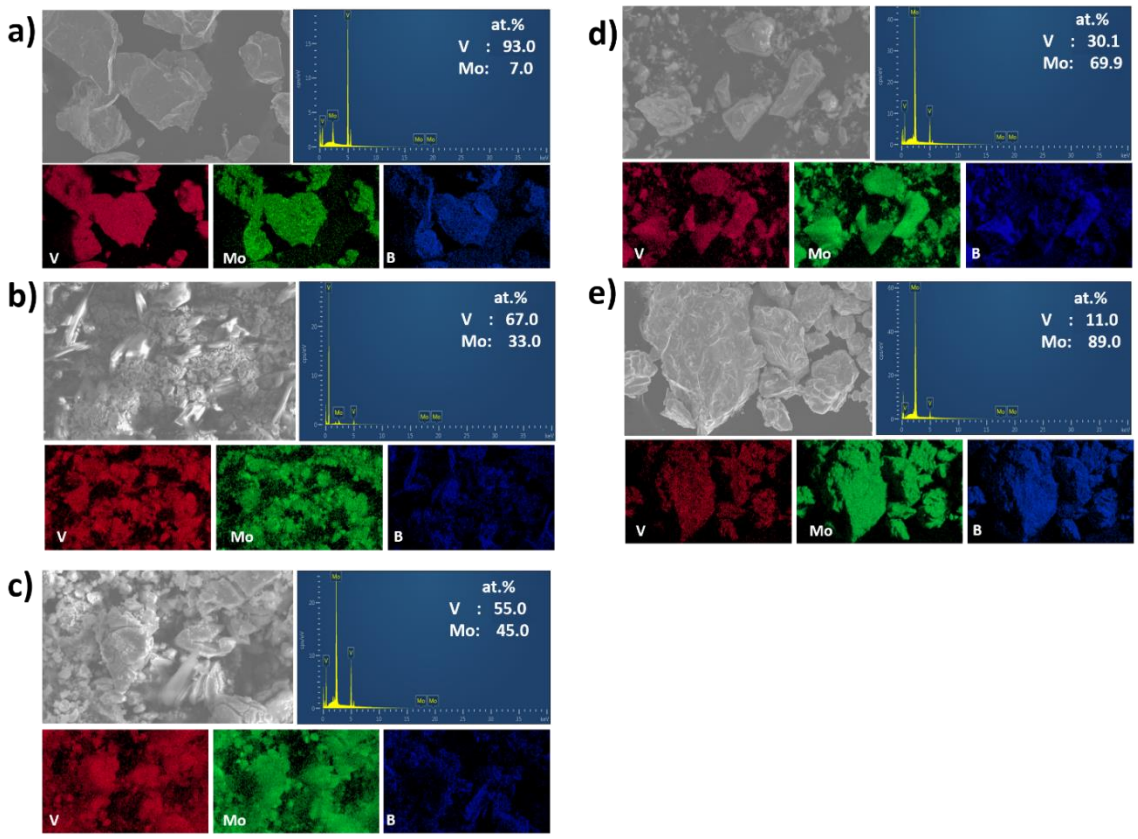

Figure 3.3. EDS mapping of a) $V_{0.9}Mo_{0.1}B_2$, b) $V_{0.7}Mo_{0.3}B_2$, c) $V_{0.5}Mo_{0.5}B_2$, d) $V_{0.3}Mo_{0.7}B_2$, and e) $V_{0.1}Mo_{0.9}B_2$.

$V_{1-x}Mo_xB_2$ (x=0.1, 0.3, 0.5, 0.7, and 0.9) was successfully synthesized by the arc-melting. As shown in **Figure 3.1a** and **Figure 3.2**, the whole solid solution range of $V_{1-x}Mo_xB_2$ could be synthesized in the AlB_2-type structure and Rietveld refinements of the powder X-ray diffraction (PXRD) patterns indicate a single-phase crystalline samples. To support the successful synthesis, an energy-dispersive X-ray spectroscopy (EDS) analysis was conducted (**Figure 3.3**). The quantitative EDS analysis demonstrates the atomic ratio of V and Mo that matched the refined compositions well. Besides, the EDS mapping data in **Figure 3.3** shows the uniform distribution of V, Mo, and B in each sample, which not

only means successful synthesis but also proves the random distribution of V (or Mo) atoms in the crystal structure. The refined lattice parameters plotted as a function of the Mo content show different trends (**Figure 3.1b):** The *a* lattice parameter plot follows Vegard's law[18] due to the larger atomic size of Mo compared to V, while the *c* lattice parameter plot adopts a volcano-like shape where the Mo content increases until 70 at.% then decreases. Our previous report[12] introduced the same unexpected *c* lattice parameter trend in the solid solution of $Cr_{1-x}Mo_xB_2$, and DFT calculations suggested that magnetism may contribute to this trend since the spin-polarized (magnetic) model could reproduce the same *c* lattice parameter trend as experimental data while the non-spin polarized model showed a linear trend instead. However, all the elements in the V-Mo-B system as well as their respective binaries do not show magnetic ordering properties, which means that magnetic property but also other factors are responsible for the unexpected behavior of the *c* lattice parameter.

To explain the unexpected trend of the *c* lattice parameter, the projected density of states (pDOS) and projected crystal orbital Hamilton population (pCOHP) of VB_2, MoB_2, Mo-deficient $Mo_{0.875}B_2$, and Mo-deficient $V_{0.250}Mo_{0.625}B_2$ were calculated. Firstly, the DOS plots of all four models in **Figures 3.4b** and **3.4c** have states at the Fermi level indicating metallic behavior which is a beneficial property for efficient electrocatalysts. There is also a strong overlap between the B (green) sp orbitals and M (red, lavender, and purple) d_{xz}, d_{yz}, and d_z^2-orbitals which means hybridization between these orbitals will occur, so studying the interaction between the M and B atoms in the structures will be crucial in explaining the c-lattice parameter behavior of the solid solution.

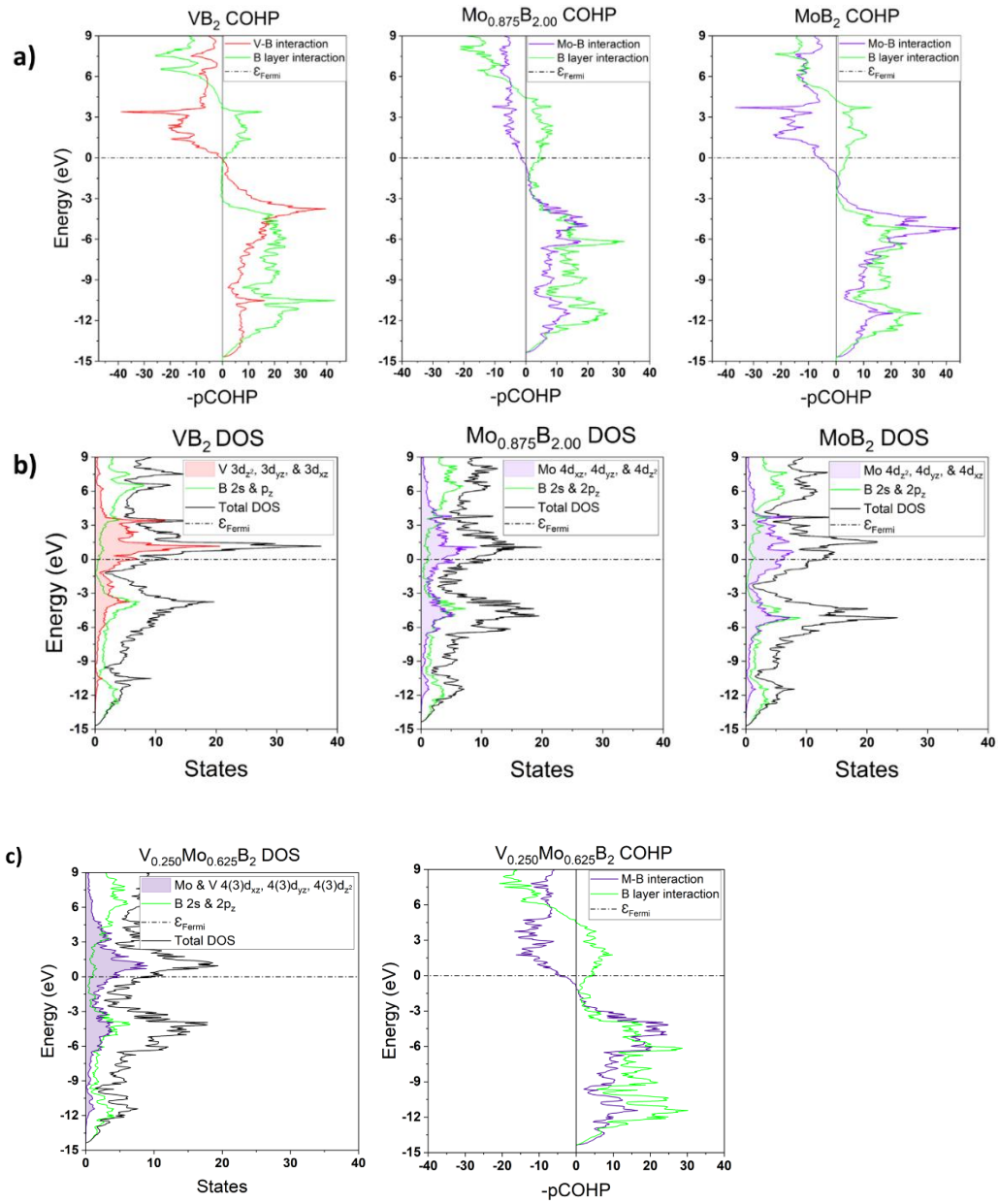

Figure 3.4. a) COHP plots with the metal-boron (red, purple) and boron-boron (green) interactions and b) DOS plots with the projected orbitals states with z-axis contributions for the 3 binary borides VB_2, Mo-deficient $Mo_{0.875}B_2$, and MoB_2. d) The DOS and COHP plots for Mo-deficient $V_{0.25}Mo_{0.625}B_2$.

Table 3.1. Crystallographic information for the prepared $V_{1-x}Mo_xB_2$.

Sample	$V_{0.9}Mo_{0.1}B_2$	$V_{0.7}Mo_{0.3}B_2$
Crystal system	Hexagonal	Hexagonal
Space group	*P6/mmm*	*P6/mmm*
a [Å]	3.0026(9)	3.0180(5)
c [Å]	3.063(1)	3.0825(6)
V [Å^3]	23.92(1)	24.32(7)
Sample	$V_{0.5}Mo_{0.5}B_2$	$V_{0.3}Mo_{0.7}B_2$
Crystal system	Hexagonal	Hexagonal
Space group	*P6/mmm*	*P6/mmm*
a [Å]	3.0293(5)	3.0372(8)
c [Å]	3.0962(7)	3.108(1)
V [Å^3]	24.61(8)	24.83(1)
Sample	$V_{0.1}Mo_{0.9}B_2$	**VB_2[1]**
Crystal system	Hexagonal	Hexagonal
Space group	*P6/mmm*	*P6/mmm*
a [Å]	3.0399(3)	2.997(8)
c [Å]	3.0773(3)	3.057(1)
V [Å^3]	24.627(3)	23.77(1)
Sample	**MoB_2[2]**	
Crystal system	Hexagonal	
Space group	*P6/mmm*	
a [Å]	3.039(6)	
c [Å]	3.064(6)	
V [Å^3]	24.55(9)	

Table 3.2. Refined occupancy of the metal site

Sample	Occupancy refinement factor			Metal site vacancy (%)	Mo:V atomic ratio
	Mo	V	total		
MoB_2	0.036250	-	0.03625	13.0	-
$V_{0.1}Mo_{0.9}B_2$	0.030086	0.00536	0.03622	13.1	0.85 : 0.15
$V_{0.3}Mo_{0.7}B_2$	0.02352	0.01144	0.03496	16.1	0.67 : 0.33
$V_{0.5}Mo_{0.5}B_2$	0.01657	0.01999	0.03656	12.3	0.45 : 0.55
$V_{0.7}Mo_{0.3}B_2$	0.01068	0.02844	0.03912	6.1	0.27 : 0.73
$V_{0.9}Mo_{0.1}B_2$	0.00308	0.03687	0.03995	4.1	0.08 : 0.92
VB_2	-	0.04270	0.04270	0	-

The -pCOHP plots in **Figure 3.4a represent** the metal-boron (M-B) interaction of VB_2 and MoB_2.At the Fermi level (E_F), the V-B interaction lies in the nonbonding region while the Mo-B interaction is near a peak in the antibonding region. This indicates that most of the anti-bonding states for Mo-B interaction are being filled compared to that of V-B interaction and since the M-B interactions, suggesting stronger V-B interactions. Given that these M-B interactions are mostly along the *c*-axis of the cell it would suggest that the *c* lattice parameter of MoB_2 should be much larger than that of VB_2. However, the refined data indicate that MoB_2 and VB_2 have similar *c* lattice parameters (**Figure 3.1 and Table 3.1**). This finding prompted a refinement of the PXRD data taking into account a possible metal vacancy. Indeed, the vacancy on the Mo site could be identified experimentally. The refined PXRD data in **Table 3.2** show that there is a not only 13.0 %

Mo vacancy in MoB_2 but also a range from 4.1 to 16.1 % of vacancy in $V_{1-x}Mo_xB_2$. To account for this the -pCOHP of Mo-deficient MoB_2 ($Mo_{0.875}B_2$) was then calculated (**Figure 3.4a,** middle), the results of which showed that the Mo-B antibonding interactions at E_F are now closer to the non-bonding region which would lead to a decrease in the *c*-lattice parameter close to that of VB_2.

Next, the COHP and DOS of Mo-deficient $V_{0.25}Mo_{0.75}B_2$ ($V_{0.25}Mo_{0.625}B_2$) were calculated and shown in **Figure 3.4c.** At the Fermi level, it shows that the combined M-B interaction from both Mo and V lies just under a peak in the antibonding region indicating that almost all of the local antibonding states are being filled. In addition to that, $V_{0.25}Mo_{0.75}B_2$ also has the highest % Mo vacancy at 16.1% which would also further weaken the interplane bonding studied by Shein and Ivanovskii[19] and would lead to further enlargement of the c lattice parameter which is especially prevalent in Mo containing borides as studied by Shein and Ivanovskii[19]. Therefore, the volcano-like shape of the *c* lattice parameter can be explained by both the increasing amount of antibonding Mo-B interaction and the % of Mo vacancies within the solid solution.

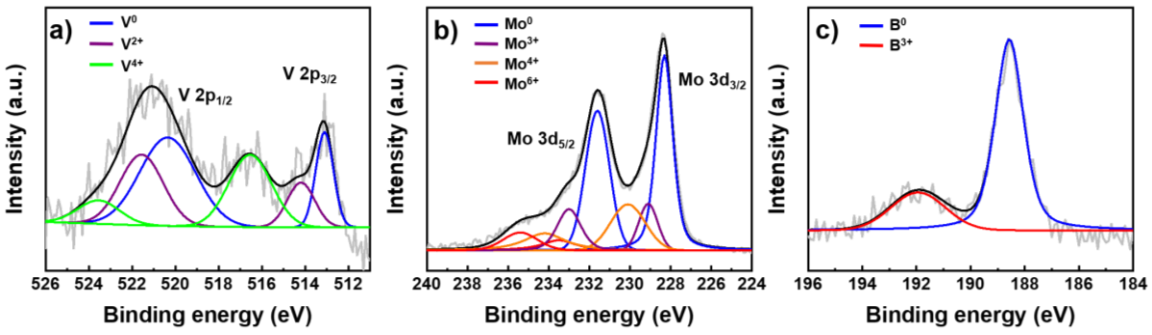

Figure 3.5. X-ray photoelectron spectroscopy spectra of a) V 2p, b) Mo 3d, and c) B 1s of $V_{0.3}Mo_{0.7}B_2$.

Table 3.3. XPS peak position and full width at half maximum (FWHM) parameters for V 2p, Mo 3d, and B1s of $V_{0.3}Mo_{0.7}B_2$ before and after HER measurement.

Phase	Species	Peak position (eV)	FWHM (eV)
$V_{0.3}Mo_{0.7}B_2$ Before HER	V^0	513.1, 520.4	0.96, 3.04
	V^{2+}	514.2, 521.6	1.50, 2.35
	V^{4+}	516.5, 523.6	2.33, 2.26
	Mo^0	228.3, 231.6	0.98, 1.40
	Mo^{3+}	229.1, 233.5	1.10, 2.00
	Mo^{4+}	230.1, 234.2	2.01, 2.40
	Mo^{6+}	233.0, 235.4	1.37, 2.00
	B^0	188.6	1.23
	B^{3+}	191.9	2.36
$V_{0.3}Mo_{0.7}B_2$ After HER	V^0	513.0, 520.4	1.03, 1.96
	V^{2+}	514.1, 521.6	2.00, 2.72
	V^{4+}	516.5, 523.6	2.54, 2.50
	Mo^0	228.3, 231.6	1.15, 1.56
	Mo^{3+}	229.1, 233.5	0.98, 1.00
	Mo^{4+}	230.1, 234.2	1.08, 1.92
	Mo^{6+}	232.9, 235.4	0.95, 2.43
	B^0	188.6	1.49
	B^{3+}	191.9	1.50

The surface chemical composition and the core-level binding energy of the $V_{0.3}Mo_{0.7}B_2$ were investigated by X-ray photoelectron spectroscopy (XPS). **Figure 3.5** and **Table 3.3** show the oxidation states of the V 2p, Mo 3d, and B 1s species on the analyzed surfaces. As shown in **Figure 3.5a**, the high-resolution V 2p spectrum is deconvoluted into V $2p_{1/2}$ and V $2P_{3/2}$: The two peaks at 513.1/520.4 eV originate from the metallic vanadium (V^0). The two other doublets at 514.2/521.6 eV and 516.5/523.6 eV can be ascribed to V^{2+} and V^{4+} respectively from the surface oxide layer.[10, 20-21] The

Mo 3d spectrum (**Figure 3.5b**) is deconvoluted into Mo $3d_{3/2}$ and Mo $3d_{5/2}$, with Mo^0 assigned to metallic molybdenum, Mo^{3+}, Mo^{4+}, and Mo^{6+} correspondingly to molybdenum oxide peaks.[12, 22-23] Finally, the B 1s spectrum (**Figure 3.5c**) is deconvoluted into B^0 (188.6 eV) in $V_{0.3}Mo_{0.7}B_2$ and B^{3+} (191.9 eV) which is attributed to B_2O_3.[10, 12, 24] The oxide peaks of all the elements originate from exposing the materials in the air, and especially vanadium is oxidized more due to the air sensitivity. However, the XPS data after HER measurements (**Figure 3.6**) show decreased intensities of the oxide peaks for all the ions because the oxides are dissolved by the acidic solution, as found by previous reports on borides electrocatalysts[10]. Therefore, the impact of the catalytic activity of metal oxide in 0.5 M H_2SO_4 electrolytes can be neglected.

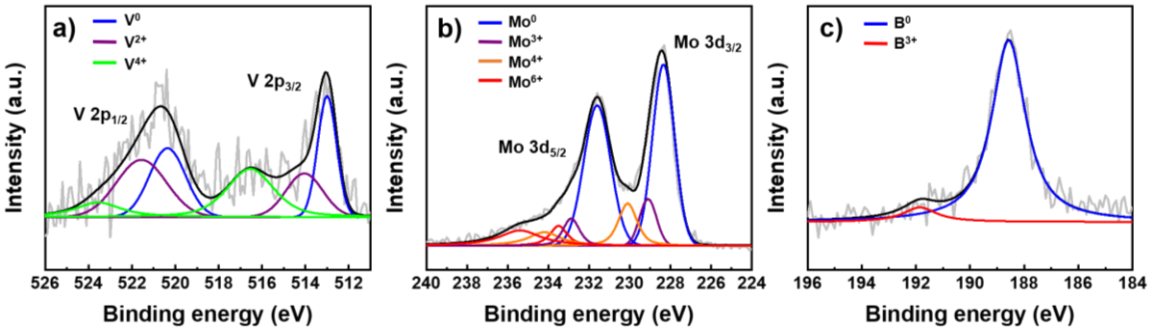

Figure 3.6. X-ray photoelectron spectroscopy spectra of a) V 2p, b) Mo 3d, and c) B 1s of $V_{0.3}Mo_{0.7}B_2$ after HER measurement.

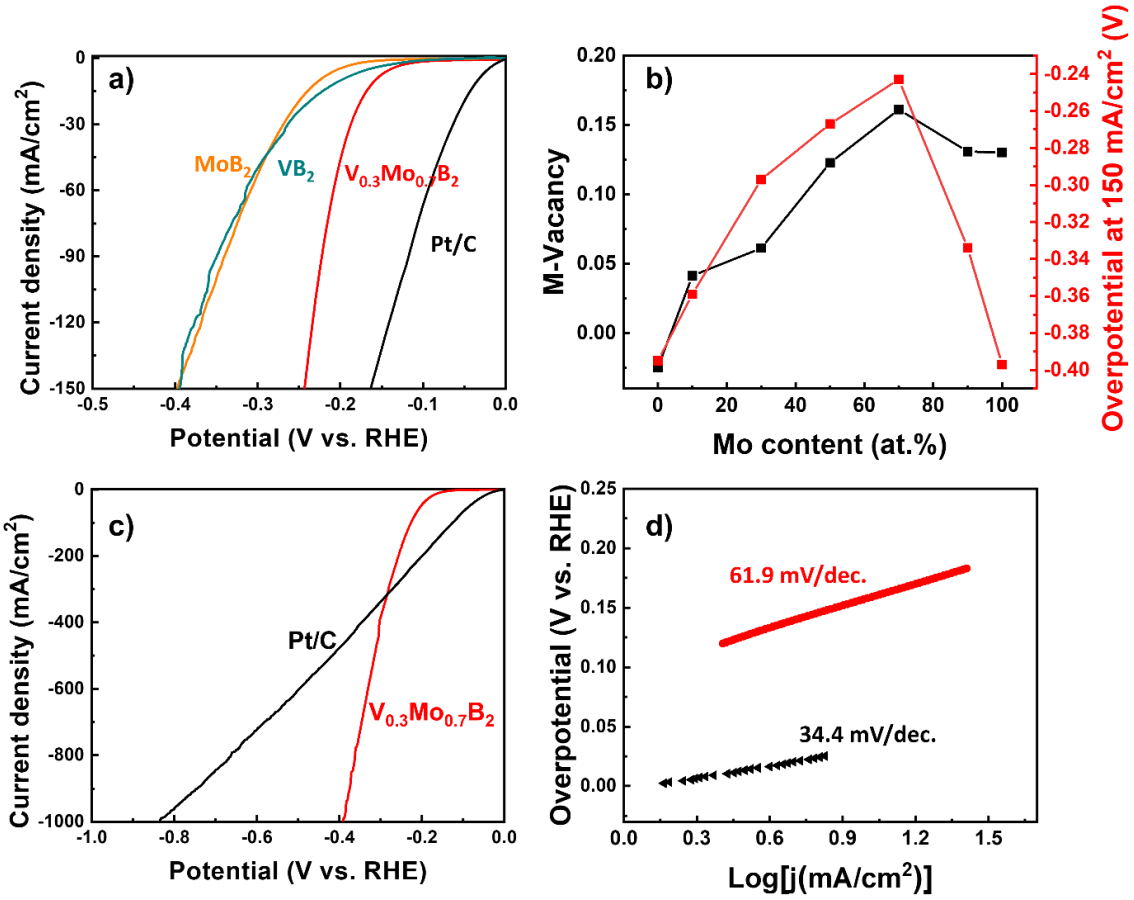

Figure 3.7. a) Linear sweep polarization curves of different materials recorded at a scan rate of 5 mV/s in 0.5 M H_2SO_4, b) Plots of the metal vacancy (M-vacancy) and the overpotential (at 150 mA/cm^2 current density) as a function of molybdenum content, c) Linear sweep polarization curves showing the high current density behaviors of $V_{0.3}Mo_{0.7}B_2$ and 20 % Pt/C, d) Tafel plots of $V_{0.3}Mo_{0.7}B_2$ and 20 % Pt/C.

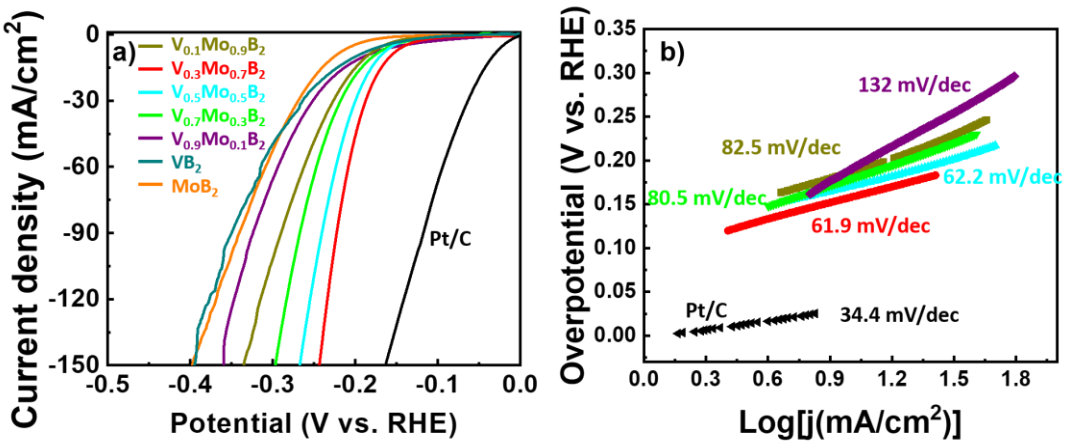

Figure 3.8. a) Linear sweep polarization curves of $V_{1-x}Mo_xB_2$ (x = 0.1, 0.3, 0.5, 0.7, and 0.9), VB_2, and MoB_2 obtained in 0.5 M H_2SO_4, b) The corresponding Tafel slopes.

For electrochemical measurements, a typical three-electrode system which is composed of the counter electrode (graphite rod), reference electrode (saturated calomel electrode), and the working electrode has been used. **Figure 3.7a** shows the *iR*-corrected polarization curves of $V_{0.3}Mo_{0.7}B_2$, Pt/C, and previously reported data of VB_2[10] and MoB_2.[11] As shown in **Figure 3.7a**, the $V_{0.3}Mo_{0.7}B_2$ sample with the highest HER activity among $V_{1-x}Mo_xB_2$ has better HER activity (overpotential at a current density of 150 mA/cm^2 (η_{150}) is 0.243 V) than binary diboride VB_2 (η_{150}= 0.395 V) and MoB_2 (η_{150}= 0.397 V). Besides, all the $V_{1-x}Mo_xB_2$ (x=0.1, 0.3, 0.5, 0.7, and 0.9) ternary diboride have higher HER activity than VB_2 and MoB_2 (**Figure 3.7b and Figure 3.8a**). It indicates that some factors in the ternary diboride system may have influenced HER activity. One possible factor that we suggest here is the metal vacancy (M-vacancy). As shown in **Figure 3.7b**, the plot of the M-vacancy as function of the Mo atomic content has a volcano-like shape reminiscent of the *c* lattice parameter plot. Interestingly, the trend of overpotential as a function of Mo atomic content also follows a similar volcano-trend as

the M-vacancy and *c* lattice parameter. **Figure 3.9** shows the DFT-predicted Gibbs free energy (ΔG_H) for atomic hydrogen (H) adsorption on the $V_{1-x}Mo_xB_2$ system at both low (25%) and high (100%) hydrogen coverages for the mixed (M and B) {110} surfaces which is one of the HER-active surfaces previously found[25] to have contrasting activity for VB_2 (favors H adsorption) and MoB_2 (favors H desorption) and reproduced in **Figure 3.9**. Hydrogen (H) binds the strongest on VB_2 since ΔG_H is lowest at both low and high hydrogen coverages (-0.42 eV < ΔG_H < -0.23 eV) which means that it will be less active. Conversely, the ΔG_H values for MoB_2 range from -0.08 eV to 0.11 eV crossing 0 eV at around 60% H coverage, thereby showing better activity. A similar range (-0.14 eV to 0.07 eV) was found for the Mo-deficient MoB_2. However, 60% H coverage is low and not ideal for a high-performing catalyst, especially at high current densities. Interestingly, the ΔG_H values for the {110} surface of the ternary Mo-deficient $V_{0.250}Mo_{0.625}B_2$ range from -0.25 eV to -0.12 eV (low to high H coverages), effectively placing it in between those of the binaries. This finding suggests that there is a synergy between the two metals within the ternary catalyst at high current densities: At 100% H coverage hydrogen would be held strongly by V (good for adsorption) but loosely by Mo (good for desorption) making the ternary more effective catalyst than the two binaries.

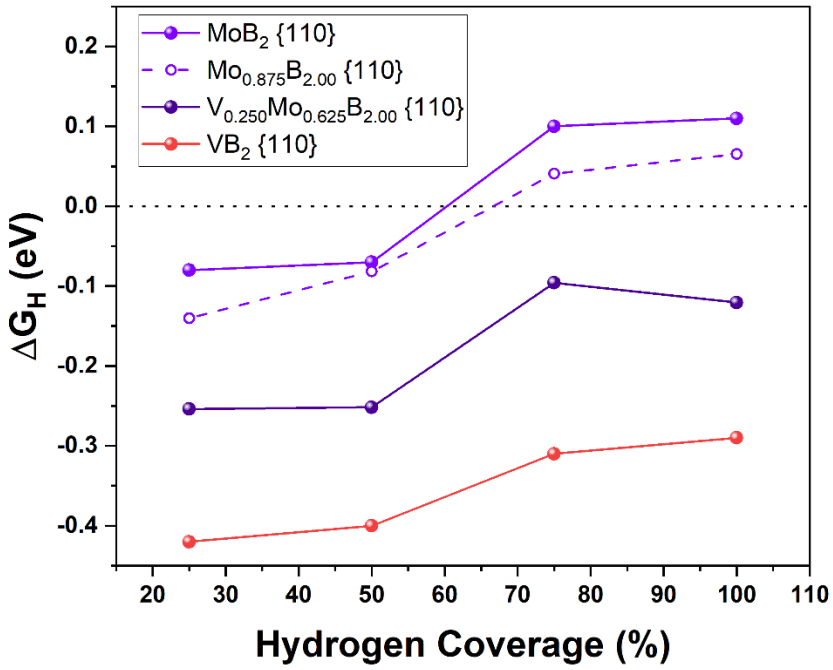

Figure 3.9. Gibbs free energy (ΔG_H) for H adsorption on the {110} surfaces of Mo deficient $V_{0.250}Mo_{0.625}B_2$ and $Mo_{0.875}B_2$ as a function of hydrogen coverage. Included are also the values for MoB_2 and VB_2 which were previously calculated in reference.[25]

Another explanation for this trend of HER activity can also be given by the analysis of the M-B covalent bonds using the COHP plots. For example, Liu et al studied the nature of d-d orbital interactions in metallic WO_2 and its effects on HER activity[26] they showed that replacing some of the W atoms in the oxide with a late-transition metal (Fe, Co, Ni, & Cu) weakened the bond between W-M and brought the DFT calculated ΔG_H closer to 0 with Ni-WO_2 found to be most active. The bond weakening is due to the increase of the antibonding orbital filling of the W-M bond, with the E_F of Ni-doped WO_2 being at an antibonding orbital peak for the COHP. In the case of TMBs however, relating the M-B covalent bonds (instead of the weaker M-M bonds) to the HER activity

is crucial, since there is strong hybridization between M d-orbitals and the B sp orbitals as seen from the DOS and the pCOHP plots in **Figure 3.4.** The pCOHP plots of the M-B interactions (**Figure 3.4a)** show that for both VB_2 and Mo-deficient MoB_2 ($Mo_{0.875}B_2$) the E_F lies near the non-bonding region, in other words, COHP would predict that the two TMBs would have similar HER activities as was found experimentally (**Figure 3.7a).** Meanwhile, for the pCOHP plots of the M-B interaction of $V_{0.250}Mo_{0.625}B_2$ (**Figure 3.4c)** the E_F lies near a peak in the antibonding region which implies that increased filling of the antibonding states between M and B atoms would lead to low H adsorption energy (ΔE_H) and ΔG_H according to the d-band theory.[27]

The above-discussed experimental and theoretical results suggest that the new ternary phase is a better electrocatalyst than the binaries at low and moderate current densities (10 and 150 mA/cm^2). To combine with renewable resources (such as a solar water-splitting device) for producing hydrogen, an overpotential value at the current density of 10 mA/cm^2 is regarded as a reference because 10 mA/cm^2 is expected for a 12.3 % efficient solar water-splitting device.[28] However, a much higher current density is required in industry for water electrolysis. For instance, a prototype of an alkaline electrolyzer has been designed to operate under a current density of 1250 mA/cm^2.[29] Therefore, we will compare the HER activity at a current density of 1000 mA/cm^2. As shown in **Figure 3.7c**, $V_{0.3}Mo_{0.7}B_2$ requires only 0.391 V to deliver 1000 mA/cm^2 which is less than half of the overpotential needed for Pt/C (η_{1000}= 0.837 V). It shows the outstanding performance of our material at a very high current density, which makes it more suitable for practical industrial applications than Pt/C.

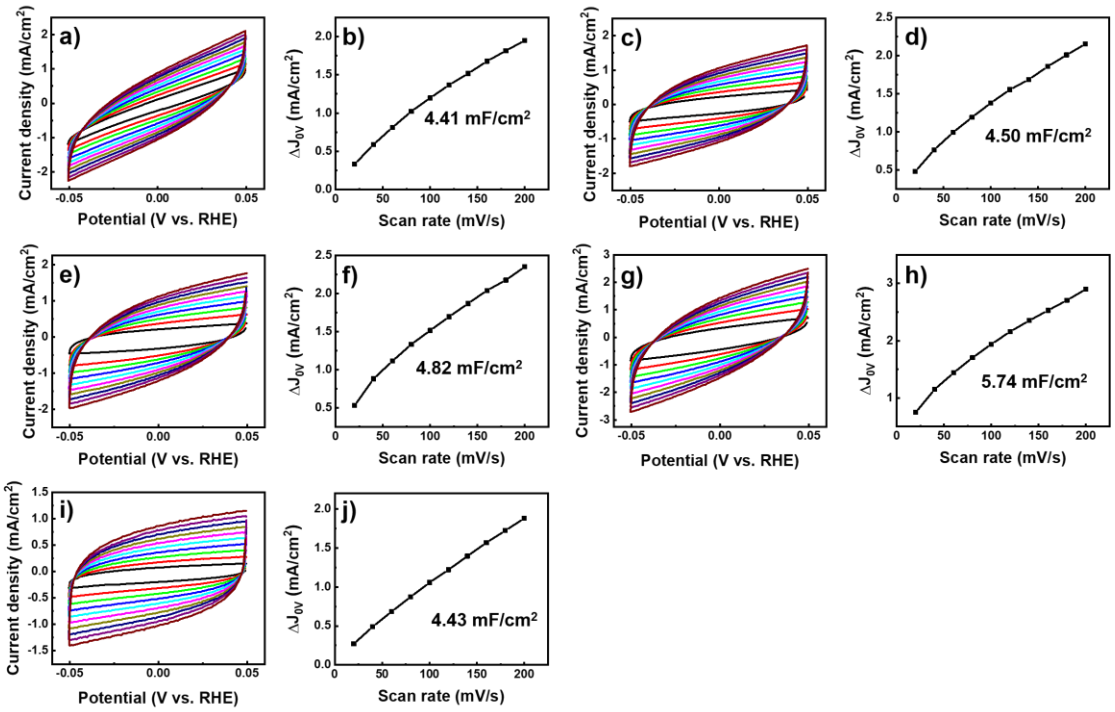

Figure 3.10. Cyclic voltammetry profiles and linear fitting of the capacitive currents versus scan rates obtained from cyclic voltammetry tests at 0.0 V vs. RHE to estimate C_{dl} for (a, b) $V_{0.9}Mo_{0.1}B_2$, (c, d) $V_{0.7}Mo_{0.3}B_2$, (e, f) $V_{0.5}Mo_{0.5}B_2$, (g, h) $V_{0.3}Mo_{0.7}B_2$, and (i, j) $V_{0.1}Mo_{0.9}B_2$.

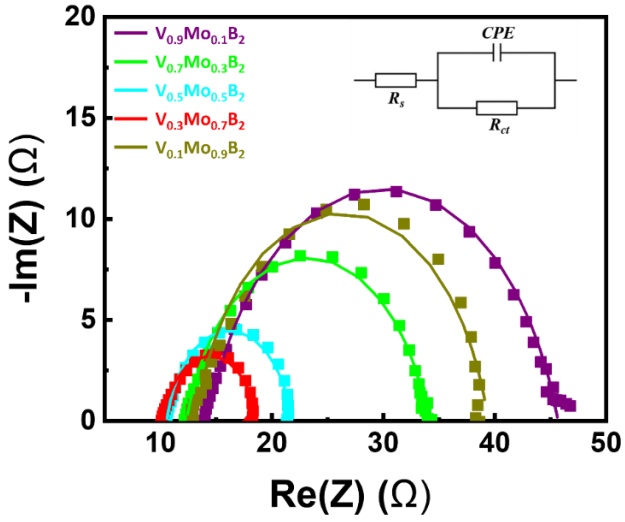

Figure 3.11. Nyquist plot representations of the electrochemical impedance spectra of $V_{1-x}Mo_xB_2$ electrode in 0.5 M H_2SO_4. The point is experimental data and the line is the fitting line.

Table 3.4. Fitted EIS data

Electrolyte	Eletrode	R_s [3]	R_{ct} [3]	CPE [F s^{a-1}]	a
0.5 M H_2SO_4	$V_{0.9}Mo_{0.1}B_2$	14.28	31.39	1.57 e^{-4}	0.806
	$V_{0.7}Mo_{0.3}B_2$	12.33	21.68	1.31 e^{-4}	0.846
	$V_{0.5}Mo_{0.5}B_2$	10.57	11.18	1.46 e^{-4}	0.861
	$V_{0.3}Mo_{0.7}B_2$	9.75	8.95	2.08 e^{-4}	0.831
	$V_{0.1}Mo_{0.9}B_2$	13.15	26.25	1.27 e^{-4}	0.847

Figure 3.7d and **Figure 3.8b** show the Tafel plots of $V_{1-x}Mo_xB_2$ (x = 0.1, 0.3, 0.5, 0.7, and 0.9) and Pt/C near the onset potential to reveal the HER catalytic mechanism. According to the HER mechanism in an acid electrolyte, three possible reactions can be the rate-determining step (RDS); Volmer reaction (Tafel slope ~120 mV/dec), Heyrovsky reaction (Tafel slope ~40 mV/dec), and Tafel reaction (Tafel slope ~30 mV/dec).[30-31] The Tafel plot for Pt/C exhibits a Tafel slope of 34.4 indicating that the Tafel reaction is likely the RDS. The Tafel slopes of the $V_{1-x}Mo_xB_2$ phases deviate from the theoretical values, indicating that the bulk HER catalysts follow a more complex mechanism than Pt/C in accordance with literature findings. However, $V_{0.3}Mo_{0.7}B_2$ has the lowest Tafel slope (61.9 mV/dec) among the $V_{1-x}Mo_xB_2$ phases, which means that it has the highest HER efficiency.[11] The highest HER efficiency of $V_{0.3}Mo_{0.7}B_2$ can be supported by the electrochemically active surface area (ECSA) and electrochemical impedance spectroscopy (EIS). Firstly, the ECSA can be estimated from the electrochemical double-

layer capacitance (C_{DL}) of the catalyst surface[32] and it can be obtained from cyclic voltammetry (CV) measurements at various scan rates (20-200 mV/s) within a non-faradic reaction region from -0.05 to 0.05 V vs RHE (**Figure 3.10**). As we expected, $V_{0.3}Mo_{0.7}B_2$ has the highest C_{DL} (5.74 mF/cm^2) among all $V_{1-x}Mo_xB_2$ indicating that it has the highest number of active sites. Besides, EIS data in **Figure 3.11** shows the electron transfer resistance of $V_{1-x}Mo_xB_2$. The plot is fitted using an equivalent circuit model which consists of a solution resistance (R_s), a charge transfer resistance (R_{ct}), and a constant phase element (CPE), and each derived value is given in **Table 3.4**. As shown in **Figure 3.11** and **Table 3.4**, the R_s of all the samples is similar because the same electrode preparation method was used. The R_{ct} of the samples, which is related to the electron transfer efficiency, follows the same trend as the overpotential. Therefore, these data are in good agreement with the HER activity trend and support the highest HER activity for $V_{0.3}Mo_{0.7}B_2$.

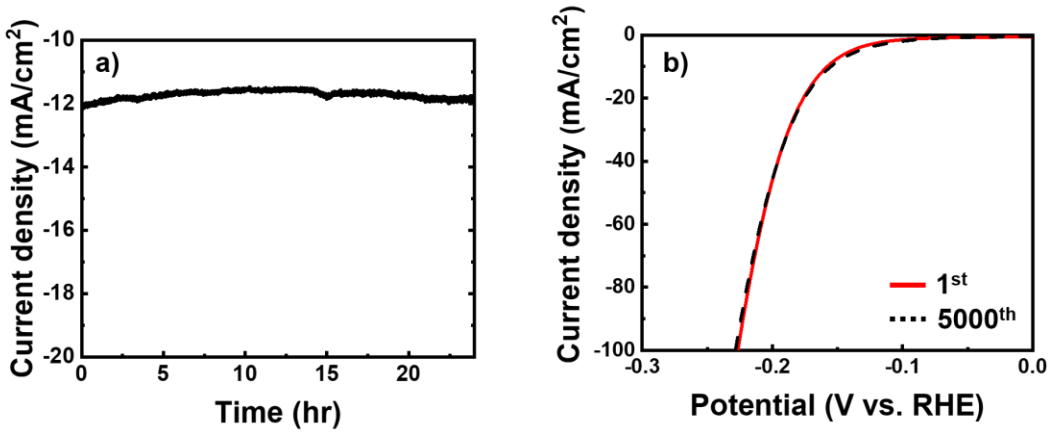

Figure 3.12. a) Chronoamperometry curve of $V_{0.3}Mo_{0.7}B_2$ electrode for 24 h, b) HER stability measurement of $V_{0.3}Mo_{0.7}B_2$ electrode before and after 5000 cycles with a scan rate of 100 mV s^{-1} in 0.5 M H_2SO_4.

The long-cycle stability of the catalysts is also an important part of practical application. For the durability test of the $V_{0.3}Mo_{0.7}B_2$ electrode, a chronoamperometry measurement was carried out at 12 mA/cm^2 for 24 h (**Figure 3.12a**). It shows that the electrocatalyst maintains a stable current density over 24 h of operation. Moreover, further long-term electrochemical stability tests using CV measurements were continuously conducted for 5000 cycles (**Figure 3.12b**). The polarization curves after 5000 cycles exhibit highly efficient HER activity without degradation. These two tests reveal that the $V_{0.3}Mo_{0.7}B_2$ catalyst is exceedingly stable in an acid electrolyte.

3.5. Conclusion

In summary, the full solid solution $V_{1-x}Mo_xB_2$ (x = 0.1, 0.3, 0.5, 0.7, and 0.9) has been synthesized by an arc-melting method and tested as HER electrocatalyst in the acid solution for the first time. Interestingly, the *c* lattice parameter of $V_{1-x}Mo_xB_2$ shows a volcano-like shape due to an increase in the filling of the antibonding states between the metal (M = V/Mo) and boron atoms. Moreover, the M-vacancy also affects ΔG_H as it shows a consistent trend with that of HER activity. Among the $V_{1-x}Mo_xB_2$, $V_{0.3}Mo_{0.7}B_2$ catalyst, which has the largest M-vacancy and *c* lattice parameter, exhibits the highest HER activity and shows outstanding long-term stability without any degradation for 24 h operation at 12 mA/cm^2 and after 5000 CV cycles. Through this work, a new path, using the c lattice parameter trend driven by vacancy formation, for designing high current density-performing non-noble metal HER electrocatalysts is suggested.

3.6. Reference

1. Edwards, P. P.; Kuznetsov, V. L.; David, W. I.; Brandon, N. P., Hydrogen and fuel cells: towards a sustainable energy future. *Energy policy* **2008,** *36* (12), 4356-4362.
2. Kosmala, T.; Coy Diaz, H.; Komsa, H. P.; Ma, Y.; Krasheninnikov, A. V.; Batzill, M.; Agnoli, S., Metallic twin boundaries boost the hydrogen evolution reaction on the basal plane of molybdenum selenotellurides. *Advanced Energy Materials* **2018,** *8* (20), 1800031.
3. Bard, A. J.; Fox, M. A., Artificial photosynthesis: solar splitting of water to hydrogen and oxygen. *Accounts of Chemical Research* **1995,** *28* (3), 141-145.
4. Chow, J.; Kopp, R. J.; Portney, P. R., Energy resources and global development. *Science* **2003,** *302* (5650), 1528-1531.
5. Turner, J. A., Sustainable hydrogen production. *Science* **2004,** *305* (5686), 972-974.
6. Zhao, Y.; Kamiya, K.; Hashimoto, K.; Nakanishi, S., In situ CO2-emission assisted synthesis of molybdenum carbonitride nanomaterial as hydrogen evolution electrocatalyst. *Journal of the American Chemical Society* **2014,** *137* (1), 110-113.
7. Anantharaj, S.; Kennedy, J.; Kundu, S., Microwave-initiated facile formation of Ni3Se4 nanoassemblies for enhanced and stable water splitting in neutral and alkaline media. *ACS applied materials & interfaces* **2017,** *9* (10), 8714-8728.
8. Sivanantham, A.; Shanmugam, S., Nickel selenide supported on nickel foam as an efficient and durable non-precious electrocatalyst for the alkaline water electrolysis. *Applied Catalysis B: Environmental* **2017,** *203*, 485-493.
9. Park, H.; Zhang, Y.; Scheifers, J. P.; Jothi, P. R.; Encinas, A.; Fokwa, B. P., Graphene-and phosphorene-like boron layers with contrasting activities in highly active Mo2B4 for hydrogen evolution. *Journal of the American Chemical Society* **2017,** *139* (37), 12915-12918.
10. Lee, E.; Park, H.; Joo, H.; Fokwa, B. T. P., Unexpected Correlation Between Boron Chain Condensation and HER Activity in Highly Active Vanadium Borides: Enabling Predictions. *Angewandte Chemie International Edition* **2020**.
11. Park, H.; Zhang, Y.; Lee, E.; Shankhari, P.; Fokwa, B. P., High-Current-Density HER Electrocatalysts: Graphene-like Boron Layer and Tungsten as Key Ingredients in Metal Diborides. *ChemSusChem* **2019,** *12* (16), 3726-3731.
12. Park, H.; Lee, E.; Lei, M.; Joo, H.; Coh, S.; Fokwa, B. P., Canonic-Like HER Activity of Cr1–xMoxB2 Solid Solution: Overpowering Pt/C at High Current Density. *Advanced Materials* **2020**, 2000855.
13. Kresse, G.; Joubert, D., From ultrasoft pseudopotentials to the projector augmented-wave method. *Physical review b* **1999,** *59* (3), 1758.
14. Kresse, G.; Furthmüller, J., Efficient iterative schemes for ab initio total-energy calculations using a plane-wave basis set. *Physical review B* **1996,** *54* (16), 11169.
15. Perdew, J. P.; Burke, K.; Ernzerhof, M., Generalized gradient approximation made simple. *Physical review letters* **1996,** *77* (18), 3865.

16. Hammer, B.; Hansen, L. B.; Nørskov, J. K., Improved adsorption energetics within density-functional theory using revised Perdew-Burke-Ernzerhof functionals. *Physical review B* **1999,** *59* (11), 7413.
17. Maintz, S.; Deringer, V. L.; Tchougréeff, A. L.; Dronskowski, R., LOBSTER: A tool to extract chemical bonding from plane-wave based DFT. Wiley Online Library: 2016.
18. Vegard, L., Die konstitution der mischkristalle und die raumfüllung der atome. *Zeitschrift für Physik* **1921,** *5* (1), 17-26.
19. Shein, I.; Ivanovskii, A., Influence of lattice vacancies on the structural, electronic, and cohesive properties of niobium and molybdenum borides from first-principles calculations. *Physical Review B* **2006,** *73* (14), 144108.
20. Wang, P.; Kumar, R.; Sankaran, E. M.; Qi, X.; Zhang, X.; Popov, D.; Cornelius, A. L.; Li, B.; Zhao, Y.; Wang, L., Vanadium diboride (VB2) synthesized at high pressure: elastic, mechanical, electronic, and magnetic properties and thermal stability. *Inorganic chemistry* **2018,** *57* (3), 1096-1105.
21. Biesinger, M. C.; Payne, B. P.; Grosvenor, A. P.; Lau, L. W.; Gerson, A. R.; Smart, R. S. C., Resolving surface chemical states in XPS analysis of first row transition metals, oxides and hydroxides: Cr, Mn, Fe, Co and Ni. *Applied Surface Science* **2011,** *257* (7), 2717-2730.
22. Mavel, G.; Escard, J.; Costa, P.; Castaing, J., ESCA surface study of metal borides. *Surface Science* **1973,** *35*, 109-116.
23. Escamilla, R.; Carvajal, E.; Cruz-Irisson, M.; Morales, F.; Huerta, L.; Verdin, E., XPS study of the electronic density of states in the superconducting Mo 2 B and Mo 2 BC compounds. *Journal of materials science* **2016,** *51* (13), 6411-6418.
24. Terlan, B. r.; Levin, A. A.; Börrnert, F.; Simon, F.; Oschatz, M.; Schmidt, M.; Cardoso-Gil, R.; Lorenz, T.; Baburin, I. A.; Joswig, J.-O., Effect of surface properties on the microstructure, thermal, and colloidal stability of VB2 nanoparticles. *Chemistry of Materials* **2015,** *27* (14), 5106-5115.
25. Jothi, P. R.; Zhang, Y.; Yubuta, K.; Culver, D.; Conley, M.; Fokwa, B., Abundant vanadium diboride with graphene-like boron layers for hydrogen evolution. *ACS Applied Energy Materials* **2018,** *2* (1), 176-181.
26. Liu, J.; Tang, C.; Ke, Z.; Chen, R.; Wang, H.; Li, W.; Jiang, C.; He, D.; Wang, G.; Xiao, X., Optimizing Hydrogen Adsorption by d–d Orbital Modulation for Efficient Hydrogen Evolution Catalysis. *Advanced Energy Materials* **2022,** *12* (9), 2103301.
27. Ai, X.; Zou, X.; Chen, H.; Su, Y.; Feng, X.; Li, Q.; Liu, Y.; Zhang, Y.; Zou, X., Transition-Metal–Boron Intermetallics with Strong Interatomic d–sp Orbital Hybridization for High-Performance Electrocatalysis. *Angewandte Chemie International Edition* **2020,** *59* (10), 3961-3965.
28. Wang, J.; Xu, F.; Jin, H.; Chen, Y.; Wang, Y., Non-noble metal-based carbon composites in hydrogen evolution reaction: fundamentals to applications. *Advanced materials* **2017,** *29* (14), 1605838.
29. Navarro, R.; Guil, R.; Fierro, J., Introduction to hydrogen production. In *Compendium of Hydrogen Energy*, Elsevier: 2015; pp 21-61.

30. Chung, D. Y.; Park, S.-K.; Chung, Y.-H.; Yu, S.-H.; Lim, D.-H.; Jung, N.; Ham, H. C.; Park, H.-Y.; Piao, Y.; Yoo, S. J., Edge-exposed MoS 2 nano-assembled structures as efficient electrocatalysts for hydrogen evolution reaction. *Nanoscale* **2014,** *6* (4), 2131-2136.
31. Sheng, W.; Gasteiger, H. A.; Shao-Horn, Y., Hydrogen oxidation and evolution reaction kinetics on platinum: acid vs alkaline electrolytes. *Journal of The Electrochemical Society* **2010,** *157* (11), B1529-B1536.
32. Trasatti, S.; Petrii, O., Real surface area measurements in electrochemistry. *Pure and applied chemistry* **1991,** *63* (5), 711-734.

Chapter 4.

Non-Precious Metal Borides: Emerging Electrocatalysts for Hydrogen Production

The development of highly active noble metal-free catalysts for the hydrogen evolution reaction (HER) is the focus of current fundamental research, aiming for a more efficient and economically affordable water splitting process. While most HER catalysts are only studied at the nanoscale (small particle size and high surface area), metal borides (MBs) are mostly studied in bulk form. This offers a unique opportunity for designing highly efficient and non-precious HER MBs electrocatalysts based on structure-activity relationships, especially because of their rich compositional and structural diversity.

In this chapter, we focus on the importance of the boron and its substructures in achieving extraordinary HER performances and the importance of using structure-activity relationships to design next-generation MBs electrocatalysts. Studying the Mo-B system, we found that the HER activity of molybdenum borides increases with increasing boron content: From Mo_2B (no B-B bonds in the structure, least active) to α-MoB and β-MoB (zigzag boron chains, intermediate activity) and MoB_2 (planar graphene-like boron layer, most active). Density functional theory (DFT) calculations have shown that the (001) boron layer in hexagonal MoB_2 (α-MoB_2) is the most active surface and has a similar HER activity behavior to the benchmark Pt (111) surface. However, puckering this flat boron layer to the chair-like configuration (phosphorene-like layer) drastically reduces its activity, thereby making the rhombohedral modification of MoB_2 (Mo_2B_4 or β-MoB_2) less active than α-MoB_2. This discovery was then further supported by studies of the Mo-W-B system: the binary WB_2, which also contains the puckered boron layer, is also less

active than α-MoB_2, despite containing the more active transition metal W which performs better in elemental form than Mo. To design a superior catalyst, the more active W was then stabilized in the hexagonal α-MoB_2 structure through the synthesis of α-$Mo_{0.7}W_{0.3}B_2$ that indeed proved to be a better HER electrocatalyst than α-MoB_2. Using the isoelectronic Cr instead of W led to the α-$Cr_{1-x}Mo_xB_2$ solid solution, the HER activity of which followed an unexpected canonic-like (or volcano-like) behavior that perfectly matched that of the c lattice parameter trend, thereby producing the best catalyst α-$Cr_{0.4}Mo_{0.6}B_2$ that outperformed Pt/C at high current density, thus underscoring the effectiveness of the structure-activity concept in designing highly active catalysts. This concept was further applied to the V-B system, leading to the discovery of an unexpected boron chain dependency of the HER activity that ultimately led to the prediction of new V_xB_y catalysts, their crystal structures, and overpotentials. Finally, reducing the particle sizes of all these bulk crystalline catalysts is also possible and offers even greater potential as demonstrated for nanoscale α-MoB_2 and VB_2. Nevertheless, these crystalline nanomaterials are still highly agglomerated due to the high temperature required for their synthesis, thus the synthesis of highly dispersed MBs is an urgent goal that will enable the fulfillment of their extraordinary potential in the future.

E. Lee *and B. P.T. Fokwa,* ***Acc. Chem. Res. 2022, 55, 56-64***

(10.1021/acs.accounts.1c00543)

4.1. Introduction

Metal borides (MBs) constitute a class of materials that are still exotic to most chemists and material scientists, despite some excellent properties that have led to many industrial applications such as permanent magnets ($Nd_2Fe_{14}B$), superconductors (MgB_2), bulk refractory and conductive ceramics (ZrB_2, HfB_2), just to name a few.[1-2] Structurally, metal borides can be divided into three groups depending on their relative boron content and the type of bonds that characterize each group. The first group concerns boron-rich borides and has a small metal-to-boron ratio (M:B < 0.5), with the highest boron content found for example in the phase YB_{66}, which is an exciting phase used as a monochromator for synchrotron radiation. These boron-rich borides are structurally characterized by the presence of three-dimensional (3D) boron networks and have no metal-metal bonds. The second group concerns metal-rich borides (M:B > 2), the permanent magnet $Nd_2Fe_{14}B$ being one of the metal-richest compositions. In contrast to the previous group, here the 3D network is built by the metal atoms and therefore there are no boron-boron bonds. The third group comprises borides with moderate boron content ($0.5 \leq$ M:B ≤ 2), the structures of which mostly contain all possible bonds. However, the boron atoms in this group usually build low-dimensional substructures (boron dumbbells, boron chains, boron layers).[1-3]

Some exciting properties of bulk metal borides have been the focus of recent investigations, these include super hardness, thermoelectric and magnetic properties.[1-2] Especially, transition metal borides are attracting considerable attention as catalytic and battery materials because they are easy to synthesize on a large scale and are

inexpensive.[4] Therefore, unlike precious metals, large-scale applications are possible. For example, nickel boride (NiB) and cobalt boride (CoB) are being explored as catalysts for the hydrodesulfurization reaction.[5] Furthermore, TiB_2, VB_2, FeB, and CoB are considered multi-electron transfer anode materials for high-energy density batteries.[6] Also, it was shown that PtB clusters (sub-nanoscale) supported on alumina have improved selectivity in dehydrogenation if compared with boron-less Pt clusters.[7] Recently, crystalline metal borides have attracted attention as active catalysts for oxidative dehydrogenation and nitrogen reduction reactions.[8-9] However, MBs as electrocatalysts for hydrogen evolution reaction (HER) and oxygen evolution reaction (OER) have seen the most interest, as demonstrated by three recent reviews of these rapidly evolving research areas.[10-12] Initially, the MBs studied as HER electrocatalysts were mostly amorphous.[13-15] However, bulk and nanoscale crystalline MBs have seen a rapid rise in recent years. For example, the crystalline FeB_2, RuB, and VB_2 nanomaterials are found to be even better HER electrocatalysts than the nanoscale amorphous binary borides.[16-18] Nanoscale RuB_2 is reported to have similar activity as the benchmark Pt/C in acidic solution and performs better than Pt/C in alkaline solution, but it still contains the precious Ru metal.[19] Despite the recent success as demonstrated in these newly published reviews,[10-12] if compared to sulfides, carbides, or phosphides, which are considered for similar applications and mostly studied at the nanoscale,[20] metal borides are far from being extensively explored, owing mainly to the difficulties encountered during their nanoscale synthesis.[21]

Conventionally, metal borides have been synthesized from the direct combination of a metal with boron at high temperatures and/or high pressures (for example by arc melting

above 2500 °C), reduction of a metal oxide or salts with boron compounds such as alkali borohydrides ($NaBH_4$), boron oxide (B_2O_3) and dehydrated borax ($Na_2B_4O_7$) in molten metal, the reaction of a boron halide with a metal or metal oxide and hydrogen, and fused salt electrolysis of metal oxide with boron oxide.[21] For large-scale preparation, borides are typically made from a carbothermal reduction of metal oxides using B_2O_3 or B_4C and carbon at temperatures above 1400 °C followed by high-temperature purification techniques. The high-temperature synthesis undoubtedly leads to large particle sizes, uncontrolled crystallization, and mixed-phase products. As an example, even the commercially available crystalline α-MoB is still contaminated by β-MoB.[22] At the nanoscale, the situation is even worse, as the stabilization of the complex bonding patterns (often a mixture of strongly covalent and metallic bonds) found in these materials usually requires high temperatures, leading to severe particle agglomeration that is detrimental to catalytic activity.[21]

As mentioned above, the challenges encountered during the synthesis of nanocrystalline MBs had initially led to the HER studies of amorphous nanoscale metal borides instead.[13-15] While such research is important and can even lead to useful applications, it is inadequate for structure-activity relationship studies because of the lack of long-range ordering and (in some cases) the lack of precise compositions. Interestingly, the high HER activity of nanocrystalline MBs, despite their high particle agglomeration, is due to the fact that these materials are already highly active in the bulk, a discovery made in 2012 by Vrubel and Hu.[22] Consequently, the structure-activity relationships can be leveraged in MBs by taking advantage of their extraordinary

structural and compositional diversity coupled to their excellent HER activity in the bulk. We have initiated this route in 2017 and recent developments focusing on non-precious metal borides are summarized below.

4.2. Boron Dependency of HER Activity in Metal Borides

Vrubel and Hu firstly found in 2012 that the commercially available polycrystalline molybdenum boride, α-MoB (particle size 1-3 μm, CrB-type structure) exhibited excellent HER activity in both acidic and basic solutions and showed a 100% Faradaic yield for hydrogen evolution.[22] Furthermore, they found that the oxides present on the surface of the material, MoO_2 and MoO_3, as well as Mo metal are not efficient catalysts for HER and that the oxides dissolved in the acid electrolyte after activation according to the XPS measurements.[22] This finding suggested that the HER activity was due to the surface boride and not the oxide. Our first contribution to this field aimed at (1) finding out if the other MoB polymorph, β-MoB (MoB-type), was as active as α-MoB, (2) studying the HER activity of other phases in the Mo-B system, and (3) to find out if a structure-activity relationship could be derived in the Mo-B system. Therefore, we synthesized, by arc-melting, four binary bulk molybdenum borides, Mo_2B, α-MoB, β-MoB, and α-MoB_2, and studied their HER activities in an acidic electrolyte, in comparison with the elements Mo and B.[23] We found that Mo and B are non-competitive HER catalysts, but Mo is more active than B because Mo is metallic while B is semiconducting. Surprisingly, when Mo and B form compounds, the HER activity increases (overpotential decreases) with increasing boron content (**Figure 4.1, left**),

indicating that boron is playing a crucial role. Especially, the presence of boron-boron bonds (**Figure 4.1, right**) favors the HER activity: While α-Mo_2B (no B-B bonds) is a less active HER catalyst, α-MoB, β-MoB, and α-MoB_2 are highly active, hexagonal α-MoB_2 (AlB_2-type structure) being the best. This discovery has since enabled the study of other boride systems such as W-B and Ru-B by other groups who found the same trend of higher HER activity for the diborides MB_2 (M = W, Ru).[17, 24] Interestingly, the crystal structures of the diborides α-MoB_2, WB_2 and RuB_2 are all different, but they differ mainly by their B substructure which is a planar graphene-like B layer in α-MoB_2, a 50:50 mixture of planar and chair-like puckered B layers in WB_2 and a boat-like puckered B layer in RuB_2.[1-2] While the remarkably high Pt/C-like HER activity of RuB_2 can be attributed to the additional contribution of the highly active platinum group and precious element Ru, the high HER activities of α-MoB_2 and WB_2 originate mainly from the B substructure because the elements W and Mo are not as HER active as Ru. This in turn raises the question of the role of the type of B layer conformation on the different activities of these diborides.

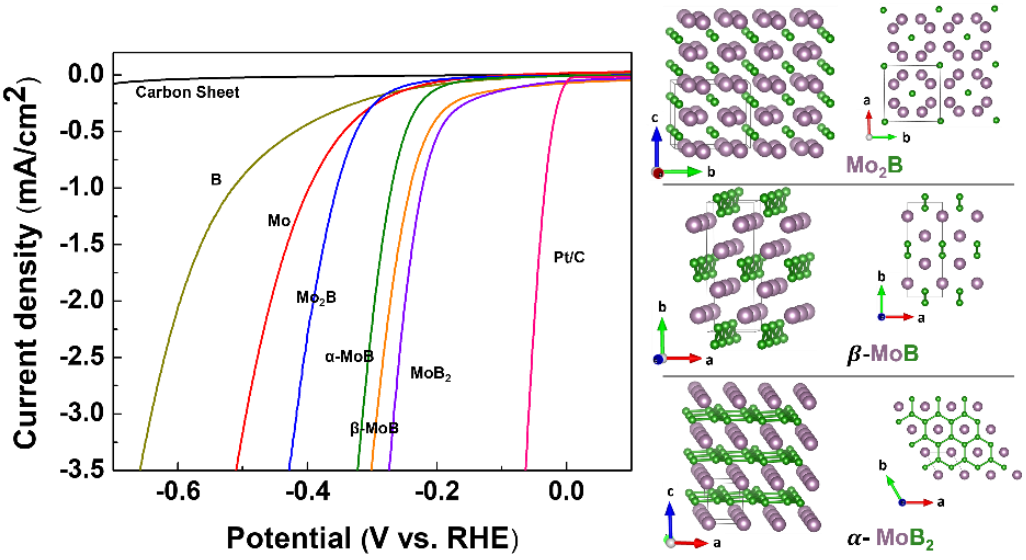

Figure 4.1. (left) Polarization curves for amorphous B, Mo, Mo_2B, α-MoB, β-MoB, and α-MoB_2 were measured in 0.5 M H_2SO_4. *IR*-drop was corrected; (right) crystal structures of Mo_2B, β-MoB, and α-MoB_2.

Density functional theory (DFT) calculations, specifically the Gibbs free energy (ΔG_H) of H adsorption, were performed on different surfaces of α-MoB_2 as well as the (111) layer of Pt and the (110) layer of elemental Mo (for comparison) to understand the origin of the high HER activity of this boride phase.[25] An optimal activity is achieved at a ΔG_H value close to zero, where the overall reaction of both H adsorption and H_2 desorption has the maximum rate.[26] The results showed that boron is indeed playing a prominent role in the catalytic activity of α-MoB_2: In fact, the graphene-like B (001) layer showed a similar HER activity behavior to the benchmark Pt (111) layer (compare black and dashed red lines in **Figure 4.2**).[25] Specifically, with increasing H coverage, ΔG_H increases in both cases and reaches zero at high H coverages. However, the Mo (001) and (100) layers were far less active as their ΔG_H curves never reached zero. However, they

perform better than elemental Mo (110) at high H coverages. Interestingly, the other identified highly active surface, the Mo/B (110) layer, also contains boron, further confirming the importance of boron in the HER activity of this phase. Consequently, multiple B-containing surfaces are active in this phase, which may explain the high HER activity of bulk borides. Nevertheless, the most active surface is the graphene-like boron layer, a discovery that suggested that AlB_2-type borides can be an ideal playground for discovering highly active HER electrocatalysts. The viability of this approach was confirmed by a different research group which found that nanocrystalline α-FeB_2 is highly active mainly because of its flat boron layer.[16] Our subsequent DFT calculations showed that puckering the flat boron layer to the chair-like conformation (phosphorene-like layer, **Figure 4.3**) drastically reduces its activity. Consequently, the rhombohedral modification of MoB_2 (β-MoB_2, also known as Mo_2B_4) that contains both boron layer types was predicted to be less active than its hexagonal variant, α-MoB_2, a finding confirmed experimentally (**Figure 4.4**).[27] This result was further supported by the study by us and others of WB_2, which has an overpotential value closer to that of β-MoB_2 than α-MoB_2 (**Figure 4.4**).[24, 28] Moreover, the lower activity of WB_2 can be explained by electrochemically active surface area (ECSA). ECSA was estimated from double-layer capacitance (C_{dl}), which can be obtained via cyclic voltammetry (CV) measurements. CV was performed at the non Faradaic potential range with various scan rates, and the difference in current density variation is plotted against scan rate. C_{dl} is obtained from half the slope of this linear plot.[29] The calculated C_{dl} values of α-MoB_2 and WB_2 (2.3 and 1.6 mF/cm^2, respectively) confirm the above finding. These results show that despite the

higher HER activity of elemental W if compared to elemental Mo, WB_2 still has a lower activity than α-MoB_2, thereby suggesting that the lower HER activity can indeed be attributed mainly to the presence of the 50% puckered chair-like B layer in WB_2.

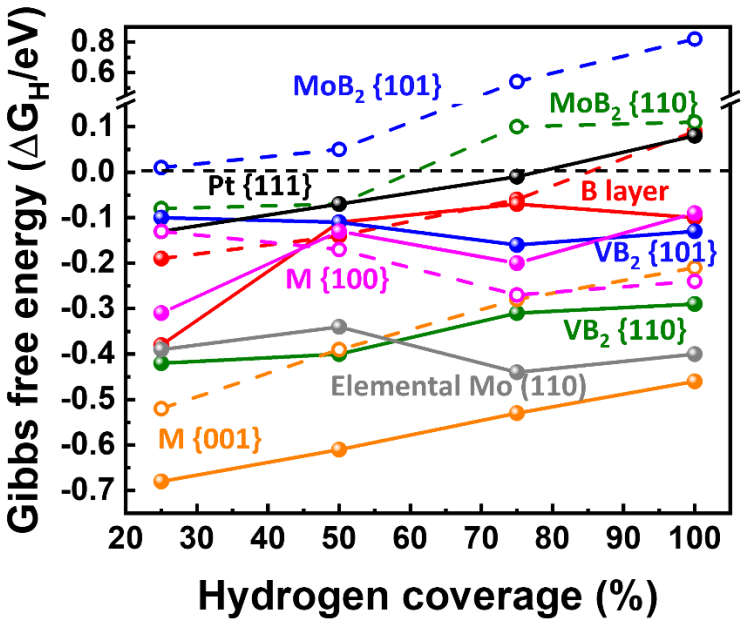

Figure 4.2. Gibbs free energy (ΔG_H) for H adsorption on surfaces of Pt, elemental Mo, and α-MoB_2 plotted as a function of hydrogen coverage. The Gibbs free energy (ΔG_H) for H adsorption on surfaces of {111} Pt (black), elemental {001} Mo (gray), and multiple surfaces for MoB_2 (dashed lines) and VB_2 (plain lines) plotted as a function of hydrogen coverage. {hkl} represents a set of (hkl) planes.

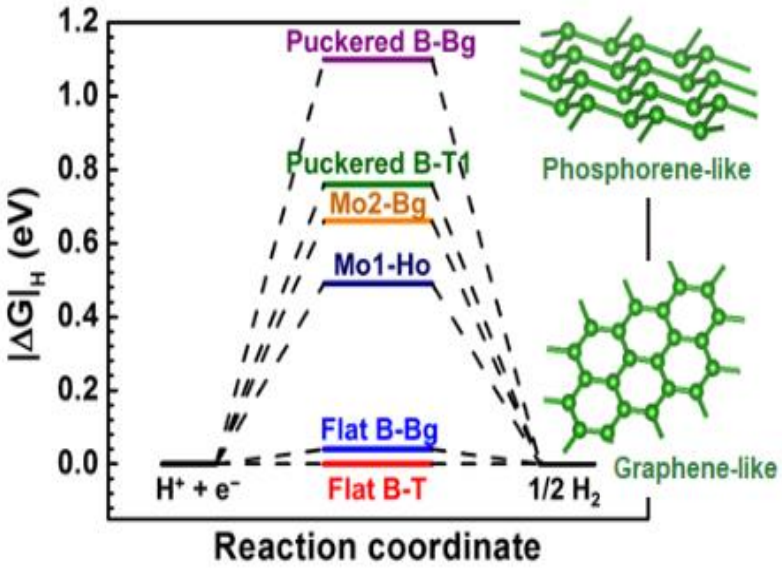

Figure 4.3. Calculated free-energy diagram for HER over different surfaces at 50% H coverage in β-MoB_2. (Right) Substructures of the two types of boron layers are present in β-MoB_2.

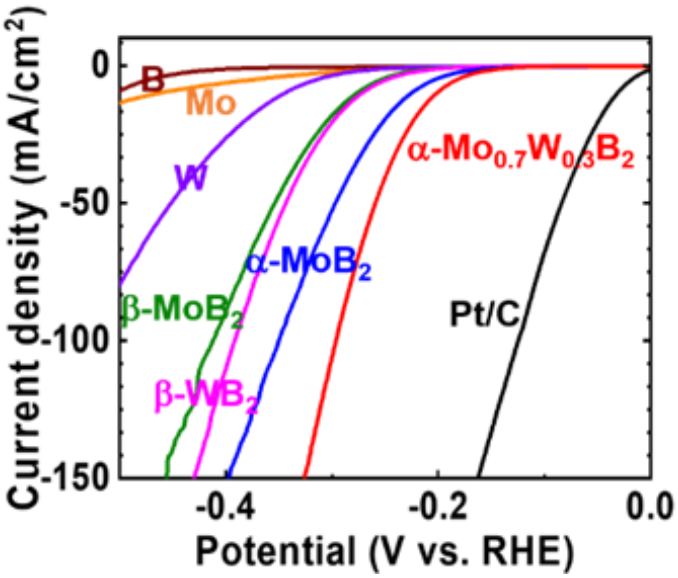

Figure 4.4. Polarization curves for β-MoB_2, α-MoB_2, WB_2, α-$Mo_{0.7}Mo_{0.3}B_2$, and Pt/C were measured in 0.5 M H_2SO_4. *IR*-drop was corrected.

4.3 Increasing HER Activity by Solid Solution Formation in AlB_2-type Borides

4.3.1. The complex $Mo_{1-x}W_xB_2$ solid solution

By taking advantage of the higher activity of W if compared to Mo, we designed a superior catalyst than α-MoB_2 by studying the HER activity of the $Mo_{1-x}W_xB_2$ solid solution.[28] In this complex solid solution, the following phases are present depending on the value of x: α-MoB_2 (x = 0), WB_2 (x = 1), single-phase α-$Mo_{1-x}W_xB_2$ ($x \leq 0.3$) and mixed ternary phases for $x > 0.3$ (dominated by the WB_2-type phase). Out of all these phases, the lowest overpotential was found for α-$Mo_{0.7}W_{0.3}B_2$ (**Figure 4.4**). The high HER activity of α-$Mo_{0.7}W_{0.3}B_2$ can be rationalized by the fact that the preferred AlB_2-type structure is maintained (due to the high Mo content) and additionally a significant amount of the more active W is present. Moreover, the ECSA of α-$Mo_{0.7}W_{0.3}B_2$ estimated by C_{dl} was larger than those of other phases in this complex solid solution. Interestingly, at higher W concentrations the activity of $Mo_{1-x}W_xB_2$ ($x > 0.3$) solid solution decreases, a behavior ascribed to the presence of the less active WB_2-type phase in these samples. This finding perfectly illustrates the importance of maintaining the flat boron layer (AlB_2-type structure) when incorporating a more active element to boost the HER activity of non-precious metal diborides. To understand the increased HER activity at high current density (at 150 mA/cm^2) in α-$Mo_{0.7}W_{0.3}B_2$, we examined the optimized structural configurations of H adsorption on the Mo/W/B (110) surface of a model phase α-$Mo_{0.75}W_{0.25}B_2$ at 100 % H coverage. Interestingly, two hydrogen atoms bonded to boron atoms were found to be attracted by W and repelled by Mo on this surface (**Figures 4.5a and 4.5b**). Consequently, W facilitates the bonding between these nearby H atoms

toward producing H_2, a behavior not found in Mo. Therefore, W is mainly responsible for the increased activity at high current density.[28] This finding suggests W as an interesting non-precious element for boosting the high-current density activity of electrocatalysts in general.

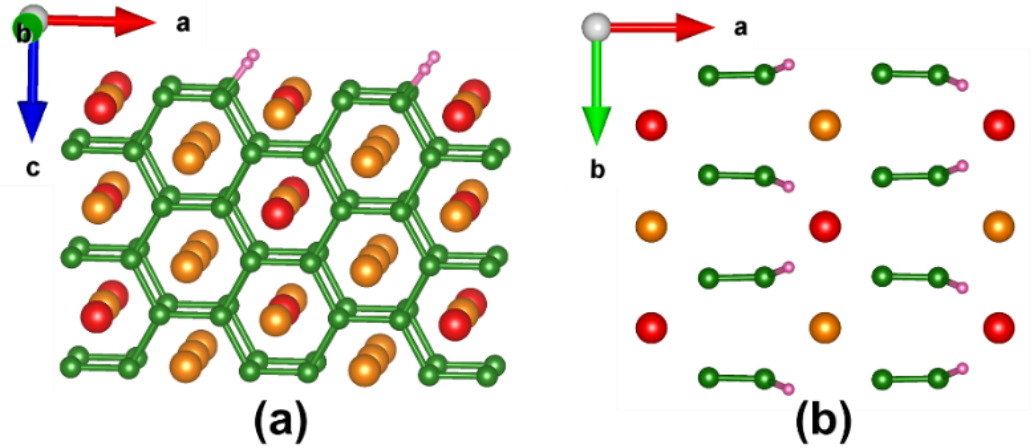

Figure 4.5. (a) The optimized structural configuration on the mixed Mo/W/B (110) surface of α-$Mo_{0.75}W_{0.25}B_2$ at 100% H-coverage. (b) The ab-plane projection of the 100% H-coverage configuration on the mixed Mo/W/B (110). Mo, W, B, and H atoms are indicated by orange, red, green, and pink spheres, respectively.

4.3.2. The full $Cr_{1-x}Mo_xB_2$ solid solution

Building on the design of highly HER-active α-$Mo_{0.7}W_{0.3}B_2$, we targeted a 3d transition metal (Cr) and maintained the number of valence electrons to allow for an atomic size-dependent study within the AlB_2-type α-$Cr_{1-x}Mo_xB_2$ solid solution while lowering the materials cost.[30] Unlike WB_2, α-CrB_2 is stable in the AlB_2-type structure, enabling the study of the full α-$Cr_{1-x}Mo_xB_2$ solid solution. The a-lattice parameter plot of α-$Cr_{1-x}Mo_xB_2$ increases linearly with increasing Mo content (x) as expected from

Vegard's law, but the *c*-lattice parameter plot surprisingly shows a canonic-like (or volcano-like) behavior (**Figure 4.6, left**) with the maximum at x = 0.6. Interestingly, the high current density activity (at 150 mA/cm^2) of this solid solution correlates very well with the canonic-like behavior of the *c*-lattice parameter plot (**Figure 4.6, left**).[30] Furthermore, α-$Cr_{0.4}Mo_{0.6}B_2$ showed the largest C_{dl} value of 5.15 mF/cm^2 which is consistent with the highest HER activity. This is a significant finding because it shows that variation of a lattice parameter can have a drastic influence on the HER activity of catalysts, thus hinting at the future design of more efficient catalysts by leveraging the structure-activity relationships in borides or in other non-precious materials. Furthermore, excellent long-term stability and durability were observed for this solid solution, with no significant activity loss after 5000 cycles and 25 h of operation in acid. To understand the high activity of the x = 0.6 composition, first-principles calculations were carried out for the (110) metal/B layers of x = 0.66 and x = 0.5. We discovered that this mixed layer promotes hydrogen evolution more efficiently for x = 0.66 than for x = 0.5: In fact, we found that at all H coverages (20 – 100 %), ΔG_H reaches zero between 85% and 90% H coverage for x = 0.66 while it never reaches zero for x = 0.5, indicating that the (110) layer performs much better for x = 0.66, thus supporting the experimental results. Furthermore, for the above-mentioned α-$Mo_{0.6}W_{0.4}B_2$, the ΔG_H plot for the (110) surface crossed zero below 60%, a much smaller percentage than that of α-$Cr_{0.33}Mo_{0.66}B_2$, indicating a better performance of the latter at high H-coverages.[30] This result corroborates experimental findings of much smaller overpotential at 150 mA/cm^2 current density for the Cr-based phase (cf. **Figures 4.4 and 4.6**). In addition, the best member of

the solid solution, α-$Cr_{0.4}Mo_{0.6}B_2$, was found to outperform Pt/C at very high current densities (**Figure 4.6, right**), as it needs 180 mV less overpotential to drive an 800 mA/cm^2 current density.[30] This discovery paves the way for the realization of the potential of non-precious MBs as suitable candidates to replace Pt/C.

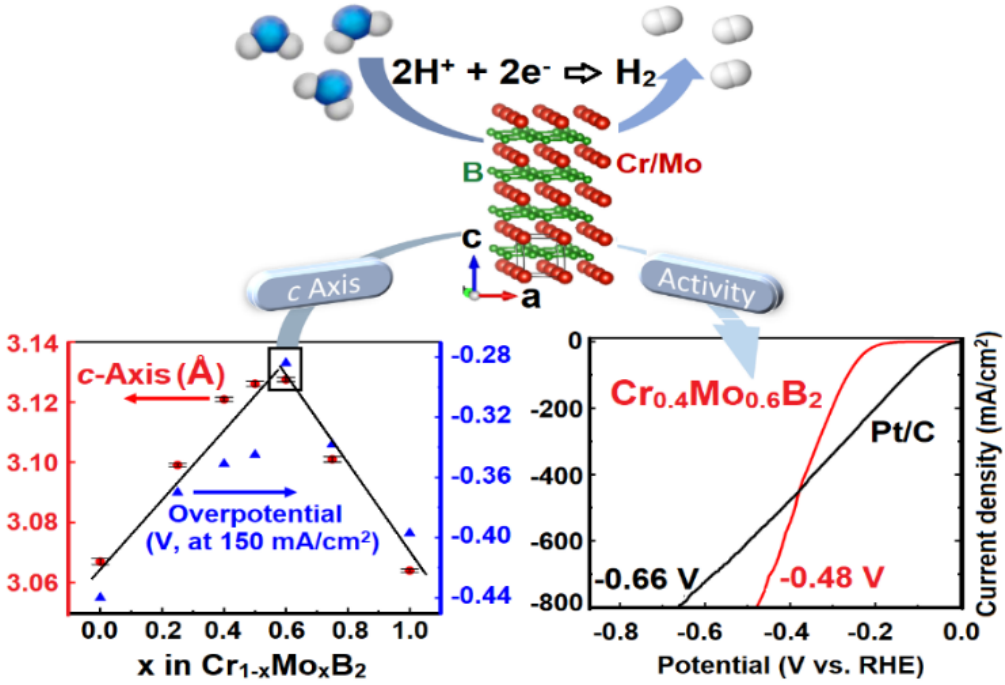

Figure 4.6. (Top) Schematic of HER reaction and crystal structure of α-$Cr_{1-x}Mo_xB_2$. (Left) Plots of *c* lattice parameter and overpotential as a function of *x*. (Right) Polarization curves for α-$Cr_{0.4}Mo_{0.6}B_2$ and 20% Pt/C were measured in 0.5 M H_2SO_4.

4.4. MBs with Boron Chain Substructures: Leveraging Boron Chain Condensation in HER.

As shown above, monoborides containing zigzag single chains of boron atoms such as α-MoB and β-MoB are as competitive toward HER as diborides containing layers

of boron atoms. Therefore, the extraordinarily rich crystal chemistry of MBs allows for an exploration of the effect of boron substructure variations on the HER activity of these materials. For example, in the V-B system, several phases exist between the monoboride VB and the diboride VB_2, namely V_5B_6 (space group *Cmcm*), V_3B_4 (Cr_3B_4-type structure, *Immm*), and V_2B_3 (*Cmcm*). Interestingly, we recently found that V_3B_4, the structure of which contains double boron chains (or chain of hexagons, **Figure 4.7**) has a lower overpotential than VB but higher than VB_2, a discovery that suggested a relationship between HER activity and boron chain condensation in V_xB_y phases.[31] Indeed, using the idea of boron chain condensation from 1 chain to double chain…, to infinite chains (boron layer) we could derive an exponential equation (e1) that helped not only to predict the overpotential of all known V_xB_y phases but also to predict unknown phases (e.g., V_5B_8 with 4 condensed boron chains, **Figure 4.7**), their crystal structures and their overpotentials.

$$\eta(mV) = -90e^{-0.25n} - 205 \qquad \text{(e1)}$$

In (e1), η is the overpotential at -10 mA/cm^2 current density, and *n (1, 2,…∞)* is the ratio of the number of 3-bonded to that of 2-bonded boron atoms in the unit cell of a given vanadium boride. Interestingly, equation (e1) can also be used to even predict the overpotentials of hybrid structures, i.e., structures containing a combination of different boron chains. For example, the overpotential of the known hybrid V_5B_6 (n = 1.5) is predicted to be between that of VB and V_3B_4, because its structure contains 50% single boron chain and 50% double boron chain. This finding also hints at potentially unknown hybrid structures (n = 2.5, 3.5…) with competitive HER activities. As we have seen for

the diborides above, the HER activity of all these boron-chain-based MBs can be further improved by solid solution formation, and such studies are in progress.

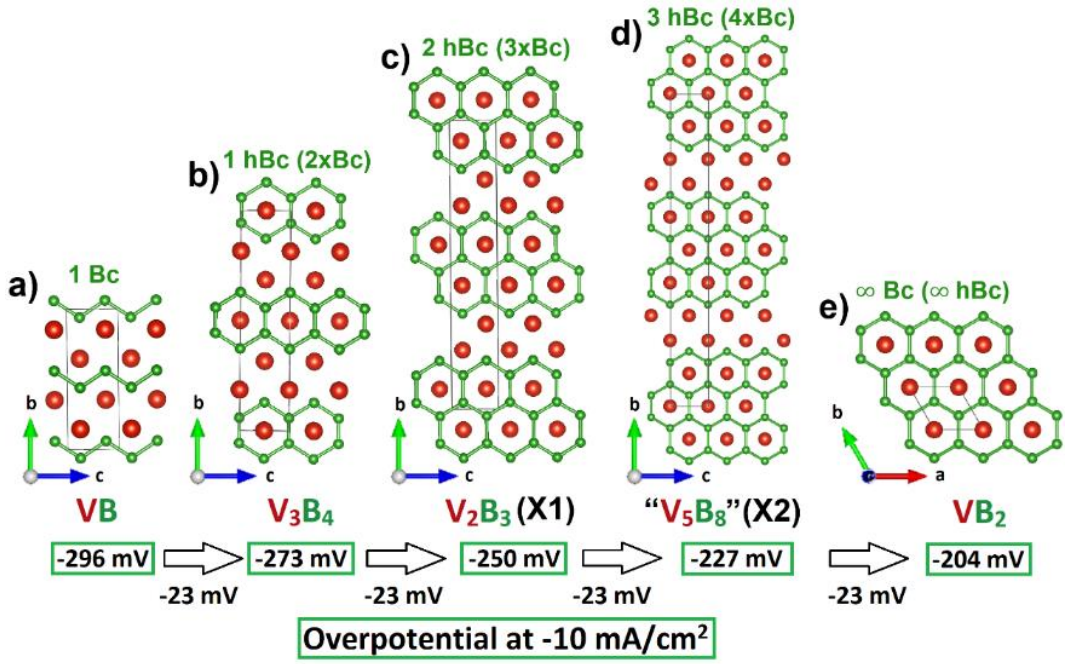

Figure 4.7. Projected crystal structures of known a) VB, b) V_3B_4, c) V_2B_3, and e) VB_2 phases. Projected crystal structure of d) hypothetical "V_5B_8". Bc = boron chain; hBc = hexagonal boron chain. Predicted overpotentials (using a -23 mV decrement) for studied and unstudied (X1 and X2) phases.

4.5. Understanding the HER Activity of Non-Precious Bulk Metal Borides

Per definition, an active electrocatalyst should have high electrical conductivity, thus making all metallic systems potentially interesting candidates. However, their activity will further depend on their ability to moderately (not too tightly and not too loosely) bind atomic hydrogen on their surfaces. As mentioned in the introduction, MBs can be divided into three groups depending on the metal to boron ratio (M:B): Metal-rich borides (M:B > 2), boron-rich borides (M:B < 2), and borides with intermediate boron content. The electrical conductivity of the boron-rich borides usually varies from poorly

conductive to semiconductive, making them unattractive electrocatalysts.[1-2] Metal-rich borides are highly conductive, and they can be attractive electrocatalysts if the metal is precious (e.g. Ru_7B_3).[17] If non-precious metals are used, their HER activity is non-competitive due to the dominating amount of the non-precious metal.[24, 28] However, increasing the number of boron atoms in these metal-rich non-precious MBs changes their electronic structures, thus leading to a significant downshift of the metal's d-band center compared to that of the pure metal.[32] This method has proven effective in predicting the HER activity of electrocatalysts in general. While the method explains the overall electrocatalytic behavior, the actual catalytic activity is surface-dependent, so the surface termination is crucial. Therefore, for a bulk electrocatalyst to be efficient, several of the exposed surfaces must be active to maximize the activity of these low-surface area materials. Consequently, the distinct HER activities of different potentially exposed surfaces of the bulk electrocatalyst have been investigated via calculations of ΔG_H. For example, high-resolution transmission electron microscopy (HRTEM) identified several surfaces on the MB_2 (M = Mo, V) particles: (001), (100), (110), and (101). Different terminations of these surfaces were then investigated via ΔG_H calculations at various H coverages. It was found (see **Figure 4.2**, plain lines), at 25% H coverage, that ΔG_H for mixed M/B-terminated (110) and (101) surfaces, B-terminated (001) and V-terminated (100) surfaces have better HER activities than the M-terminated (001), the Mo- and B-terminated (100) surfaces.[18] It should be noted that all active surfaces have comparable free energies to the noble metal Pt (**Figure 4.2**), thus underscoring their high HER activity at 25% H coverage. However, to fully understand the HER activity it is important

to examine the behavior of ΔG_H as a function of H coverage since the high percentage H coverage can be related to the behavior of the catalyst at high current density. In general, ΔG_H increases with increasing H coverage for all surfaces except for the Mo-terminated (100) surface which slightly decreases. Also at higher H coverages, the (101) surface of MoB_2 becomes far less active at 100 % H coverage. Based on these findings, the two binary bulk borides should have very competitive and similar HER activities.[18, 25] Evidently, their high activity in the bulk can be explained by the high number of active surfaces. Nevertheless, the activity of these MBs can be further improved by using nanomaterials instead of bulk samples.

4.6. Crystalline Nanomaterials of Non-Precious MBs for Improved HER Activity

Most nanomaterials such as transition metal carbides, phosphides, nitrides, and chalcogenides, have been extensively studied for their various properties in recent years. Nanomaterials of transition metal borides on the contrary have seen little interest from the chemistry and material science communities, mainly because single-phase and nanomaterials are notoriously difficult to synthesize. Therefore, the search for new synthetic strategies for single-phase nanocrystalline MBs remains a hot topic. Many synthetic methods have been recently attempted such as metal flux synthesis (Al and Sn), wet-chemical synthesis, borohydride reduction and inorganic molten salt approach, solid-state metathesis based on MgB_2.[21] Recently, we discovered a simple, general synthetic method toward crystalline MBs nanomaterials.[33] This new method takes advantage of the redox chemistry of $Sn/SnCl_2$, the volatility and recrystallization of $SnCl_2$ at the synthesis

conditions, as well as the immiscibility of tin with boron, to produce nanocrystalline MBs of 3d, 4d, and 5d transition metals. While numerous shapes of nanoborides can be synthesized by all these synthetic methods, the use of high temperatures (700 – 900 ^{o}C) always leads to highly agglomerated particles, in fact, this issue remains the most important puzzle to be solved to boost the adoption of borides in many nanoscale applications including electrocatalysis. Despite this disadvantage, we recently showed that even agglomerated nanoborides outperform their bulk counterparts when studied under the same conditions, for example, the HER overpotentials of agglomerated MoB_2 and VB_2 nanoparticles have been improved by ca. 150 mV if compared with those found for their bulk under the same conditions.[18, 25] This improved HER activity is due to the increased surface area and higher density of active sites which can be proven by ECSA measurements (via C_{dl} values). MoB_2 and VB_2 nanoparticles have significantly higher C_{dl} values (27.8 mF/cm^2 for MoB_2 and 8.1 mF/cm^2 for VB_2) than their respective bulk particles. Furthermore, the two nanocatalysts yield Tafel slopes of 49 and 68 mV/dec which are much smaller than those of bulk samples (~126 mV/dec), thus indicating an increase in HER rate with decreasing particle size.

4.7. Electrode Preparation of Bulk versus Nanomaterials

Electrode preparation is very important to accurately assess the activity of materials. This is because a preparation method affects the electrochemical performance, and the activity of the studied material can be maximized. For instance, drop-casted bulk α-MoB_2 showed an overpotential of 300 mV for HER to drive 10 mA/cm^2 (η_{10} =300 mV). However, α-

MoB_2 disk-type electrode prepared by cutting and polishing an arc-melted sample required 74 mV less overpotential to achieve the same current density (η_{10} =226 mV).[28] Moreover, the activity of the pressed disk-type electrode, which was synthesized at high pressure, was improved by 2 times (η_{10} =149 mV) compared to the drop-casted electrode even though it is the same α-MoB_2 phase.[34] The lower activity of drop-casted bulk electrodes comes from the inefficient surface coverage of the electrode. While the disk-type electrode surface is completely covered, that of the drop-casted electrode cannot be covered completely because the particle size of the bulk powder is too large to be dispersed in the solution. This difference can lead to misinterpretation of the intrinsic activity. Therefore, to evaluate the catalytic performance precisely, it is very important to apply the appropriate electrode preparation method according to the type of material. The most common electrode preparation method is drop-casting, which is suitable for nanomaterials but unsuitable for bulk samples. Typically, a drop-casting electrode is prepared by dispersing 1 mg of catalyst in 95 μl of isopropanol (or ethanol) and 5 μl of Nafion. Then the catalyst mixture is coated dropwise on a carbon cloth or glassy carbon to achieve a catalyst loading of approximately 0.3~0.5 mg/cm^2, followed by drying for 5 h at 50 ^{o}C. This method, which relies on the homogeneous dispersion catalyst in solution to cover the holistic electrode surface, is the proper method for nano-sized powder. On the contrary, for bulk materials, such as arc-melted spherical samples or pressed pellets of powder samples, a dense disk-shaped sample can be used as an electrode directly. As shown in **Figure 4.8**, a dense synthesized sample or pressed bulk powder is put into an epoxy glue and dried overnight at room temperature. Then, the top and bottom of the

dried sample are polished, followed by attaching it to a copper plate using conductive silver paste. The exposed surface of the copper plate is covered with epoxy adhesive and dried overnight at room temperature. This method is proper for bulk materials because the whole electrode surface is covered by the catalyst.

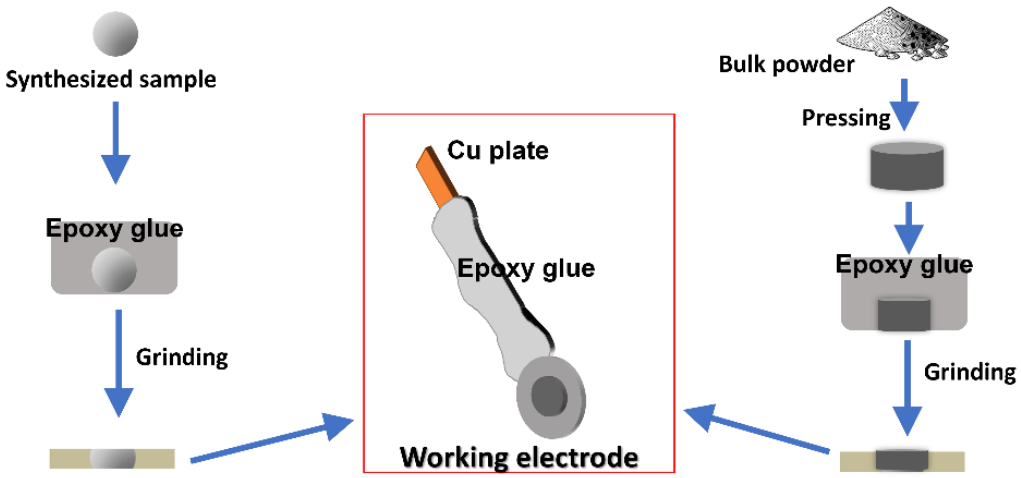

Figure 4.8. The electrode preparation process for bulk materials

4.8. Conclusion and Perspectives

In this chapter, we have demonstrated how experimental and computational methods can be effectively used to understand and predict new non-precious MBs HER electrocatalysts. We focused on the importance of the boron and its substructures in achieving extraordinary HER performances and the importance of using structure-activity relationships to design next-generation electrocatalysts. Studies of the Mo-B system have shown that the diborides MBs are the most active, however, those containing the flat graphene-like boron layers are more active than those with puckered phosphorene-like

layers. Density functional theory (DFT) calculations have shown that the (001) boron layer in hexagonal diborides MB_2 (h-MoB_2) is the most active surface and has a similar HER activity behavior to the benchmark Pt (111) surface. However, free energy calculations have also shown that several layers are active in these materials, thus explaining their high activity in the bulk. In the V-B system, these findings were confirmed and extended to the discovery of boron chain dependence of the HER activity in MBs. In fact, as the boron chains are condensed from single to double, all the way to infinite (layer) the HER activity incrementally increases, leading to an accurate mathematical prediction of the HER activity of unknown MBs and the crystal structures. Moreover, lowering the particle size of these MBs leads to a significant improvement in their activity from their bulk counterparts. However, strong particle agglomeration still hinders the fulfillment of their full potential, thus future work should focus on the synthesis of highly dispersed MBs. Finally, the electrode preparation must be done properly to maximize the activity of MBs, especially in cases of bulk samples or agglomerated nanomaterials, where the traditional drop-casting is ineffective due to the inefficient surface coverage, thus densified disk-shaped electrodes are more suitable.

4.9. References

1. Fokwa, B. P., Borides: Solid-State Chemistry. *Encyclopedia of Inorganic and Bioinorganic chemistry* **2011**, 1-14.
2. Akopov, G.; Yeung, M. T.; Kaner, R. B., Rediscovering the crystal chemistry of borides. *Advanced Materials* **2017,** *29* (21), 1604506.
3. Albert, B.; Hillebrecht, H., Boron: elementary challenge for experimenters and theoreticians. *Angewandte Chemie International Edition* **2009,** *48* (46), 8640-8668.

4. Dinh, K. N.; Liang, Q.; Du, C.-F.; Zhao, J.; Tok, A. I. Y.; Mao, H.; Yan, Q., Nanostructured metallic transition metal carbides, nitrides, phosphides, and borides for energy storage and conversion. *Nano Today* **2019,** *25*, 99-121.
5. Skrabalak, S. E.; Suslick, K. S., On the possibility of metal borides for hydrodesulfurization. *Chemistry of materials* **2006,** *18* (13), 3103-3107.
6. Gao, X.-P.; Yang, H.-X., Multi-electron reaction materials for high energy density batteries. *Energy & Environmental Science* **2010,** *3* (2), 174-189.
7. Ha, M.-A.; Baxter, E. T.; Cass, A. C.; Anderson, S. L.; Alexandrova, A. N., Boron switch for selectivity of catalytic dehydrogenation on size-selected Pt clusters on Al2O3. *Journal of the American Chemical Society* **2017,** *139* (33), 11568-11575.
8. Grant, J. T.; McDermott, W. P.; Venegas, J. M.; Burt, S. P.; Micka, J.; Phivilay, S. P.; Carrero, C. A.; Hermans, I., Boron and boron-containing catalysts for the oxidative dehydrogenation of propane. *ChemCatChem* **2017,** *9* (19), 3623-3626.
9. Qin, G.; Cui, Q.; Du, A.; Wang, W.; Sun, Q., Transition metal diborides: A new type of high-performance electrocatalysts for nitrogen reduction. *ChemCatChem* **2019,** *11* (11), 2624-2633.
10. Gupta, S.; Patel, M. K.; Miotello, A.; Patel, N., Metal boride-based catalysts for electrochemical water-splitting: A review. *Advanced Functional Materials* **2020,** *30* (1), 1906481.
11. Chen, Z.; Duan, X.; Wei, W.; Wang, S.; Zhang, Z.; Ni, B.-J., Boride-based electrocatalysts: Emerging candidates for water splitting. *Nano Research* **2020,** *13* (2), 293-314.
12. Chen, H.; Zou, X., Intermetallic borides: structures, synthesis and applications in electrocatalysis. *Inorganic Chemistry Frontiers* **2020,** *7* (11), 2248-2264.
13. Pei, Y.; Zhou, G.; Luan, N.; Zong, B.; Qiao, M.; Tao, F. F., Synthesis and catalysis of chemically reduced metal–metalloid amorphous alloys. *Chemical Society Reviews* **2012,** *41* (24), 8140-8162.
14. Masa, J.; Weide, P.; Peeters, D.; Sinev, I.; Xia, W.; Sun, Z.; Somsen, C.; Muhler, M.; Schuhmann, W., Amorphous cobalt boride (Co2B) as a highly efficient nonprecious catalyst for electrochemical water splitting: oxygen and hydrogen evolution. *Advanced Energy Materials* **2016,** *6* (6), 1502313.
15. Gupta, S.; Patel, N.; Miotello, A.; Kothari, D., Cobalt-boride: An efficient and robust electrocatalyst for hydrogen evolution reaction. *Journal of Power Sources* **2015,** *279*, 620-625.
16. Li, H.; Wen, P.; Li, Q.; Dun, C.; Xing, J.; Lu, C.; Adhikari, S.; Jiang, L.; Carroll, D. L.; Geyer, S. M., Earth-abundant iron diboride (FeB2) nanoparticles as highly active bifunctional electrocatalysts for overall water splitting. *Advanced Energy Materials* **2017,** *7* (17), 1700513.
17. Zou, X.; Wang, L.; Ai, X.; Chen, H.; Zou, X., Crystal phase-dependent electrocatalytic hydrogen evolution performance of ruthenium–boron intermetallics. *Chemical Communications* **2020,** *56* (20), 3061-3064.
18. Jothi, P. R.; Zhang, Y.; Yubuta, K.; Culver, D.; Conley, M.; Fokwa, B., Abundant vanadium diboride with graphene-like boron layers for hydrogen evolution. *ACS Applied Energy Materials* **2018,** *2* (1), 176-181.

19. Li, Q.; Zou, X.; Ai, X.; Chen, H.; Sun, L.; Zou, X., Revealing activity trends of metal diborides toward pH-universal hydrogen evolution electrocatalysts with Pt-like activity. *Advanced Energy Materials* **2019,** *9* (5), 1803369.
20. Zhu, J.; Hu, L.; Zhao, P.; Lee, L. Y. S.; Wong, K.-Y., Recent advances in electrocatalytic hydrogen evolution using nanoparticles. *Chemical reviews* **2019,** *120* (2), 851-918.
21. Carenco, S.; Portehault, D.; Boissiere, C.; Mezailles, N.; Sanchez, C., Nanoscaled metal borides and phosphides: recent developments and perspectives. *Chemical reviews* **2013,** *113* (10), 7981-8065.
22. Vrubel, H.; Hu, X., Molybdenum boride and carbide catalyze hydrogen evolution in both acidic and basic solutions. *Angewandte Chemie International Edition* **2012,** *51* (51), 12703-12706.
23. Park, H.; Encinas, A.; Scheifers, J. P.; Zhang, Y.; Fokwa, B. P., Boron-dependency of molybdenum boride electrocatalysts for the hydrogen evolution reaction. *Angewandte Chemie International Edition* **2017,** *56* (20), 5575-5578.
24. Li, Q.; Wang, L.; Ai, X.; Chen, H.; Zou, J.; Li, G.-D.; Zou, X., Multiple crystal phases of intermetallic tungsten borides and phase-dependent electrocatalytic property for hydrogen evolution. *Chemical Communications* **2020,** *56* (90), 13983-13986.
25. Jothi, P. R.; Zhang, Y.; Scheifers, J. P.; Park, H.; Fokwa, B. P., Molybdenum diboride nanoparticles as a highly efficient electrocatalyst for the hydrogen evolution reaction. *Sustainable Energy & Fuels* **2017,** *1* (9), 1928-1934.
26. Tang, Q.; Jiang, D.-e., Mechanism of hydrogen evolution reaction on 1T-MoS2 from first principles. *Acs Catalysis* **2016,** *6* (8), 4953-4961.
27. Park, H.; Zhang, Y.; Scheifers, J. P.; Jothi, P. R.; Encinas, A.; Fokwa, B. P., Graphene-and phosphorene-like boron layers with contrasting activities in highly active Mo2B4 for hydrogen evolution. *Journal of the American Chemical Society* **2017,** *139* (37), 12915-12918.
28. Park, H.; Zhang, Y.; Lee, E.; Shankhari, P.; Fokwa, B. P., High-Current-Density HER Electrocatalysts: Graphene-like Boron Layer and Tungsten as Key Ingredients in Metal Diborides. *ChemSusChem* **2019,** *12* (16), 3726-3731.
29. Wang, J.; Xu, F.; Jin, H.; Chen, Y.; Wang, Y., Non-noble metal-based carbon composites in hydrogen evolution reaction: fundamentals to applications. *Advanced materials* **2017,** *29* (14), 1605838.
30. Park, H.; Lee, E.; Lei, M.; Joo, H.; Coh, S.; Fokwa, B. P., Canonic-Like HER Activity of Cr1–xMoxB2 Solid Solution: Overpowering Pt/C at High Current Density. *Advanced Materials* **2020**, 2000855.
31. Lee, E.; Park, H.; Joo, H.; Fokwa, B. T. P., Unexpected Correlation Between Boron Chain Condensation and HER Activity in Highly Active Vanadium Borides: Enabling Predictions. *Angewandte Chemie International Edition* **2020**.
32. Ai, X.; Zou, X.; Chen, H.; Su, Y.; Feng, X.; Li, Q.; Liu, Y.; Zhang, Y.; Zou, X., Transition-Metal–Boron Intermetallics with Strong Interatomic d–sp Orbital Hybridization for High-Performance Electrocatalysis. *Angewandte Chemie International Edition* **2020,** *59* (10), 3961-3965.

33. Jothi, P. R.; Yubuta, K.; Fokwa, B. P., A simple, general synthetic route toward nanoscale transition metal borides. *Advanced Materials* **2018,** *30* (14), 1704181.
34. Chen, Y.; Yu, G.; Chen, W.; Liu, Y.; Li, G.-D.; Zhu, P.; Tao, Q.; Li, Q.; Liu, J.; Shen, X., Highly active, nonprecious electrocatalyst comprising borophene subunits for the hydrogen evolution reaction. *Journal of the American Chemical Society* **2017,** *139* (36), 12370-12373.

Chapter 5.

Molybdenum Borocarbide (Mo_2BC) as The First Hydrogen Evolution Reaction Electrocatalyst

Molybdenum-based electrocatalysts recently have been focused on excellent hydrogen evolution (HER) electrocatalysts. Among them, we study Mo_2BC, which consisted of both boride (Mo_6B trigonal prisms in β-MoB) and carbide sub-cell (Mo_6C octahedron in α-MoC), for the first time as HER electrocatalyst. The HER activity of Mo_2BC in an acid medium (0.5 M H_2SO_4) is better than that of β-MoB and α-MoC. In Mo_2BC, the electron density near Mo is moderated by electron transfer from Mo to B and C, which could enhance the activity of Mo_2BC.

Moreover, various types of electrodes (disk, bulk pellet, and ball-milled pellet) were prepared to maximize the activity. All the electrodes have high electrocatalytic HER activity in 0.5 M H_2SO_4 and especially, ball-milled pellet requires the lowest overpotential (η_{10}=-94.7 mV) to achieve 10 mA/cm^2 rather than disk (η_{10}=-182m V) and bulk pellet (η_{10}=-145 mV) electrodes. This is because the ball-milled pellet has much higher electrochemical double-layer capacitance (C_{DL}). Furthermore, Mo_2BC has outstanding activity (η_{10}=-117 mV) in an alkaline electrolyte (1 M KOH). These results are showing that Mo_2BC can be one of the promising and new non-noble electrocatalysts for HER.

5.1. Introduction

Interest in hydrogen energy has soared since the first use of the term "hydrogen economy (a forthcoming energy system based on hydrogen fuel)" by John Bockris in 1970.[1-2] Although 50 years past since the term was used, there are numerous obstacles to enabling a hydrogen economy due to the high cost of hydrogen production, storage, and delivery. One of the major hurdles to achieving the hydrogen economy is the scaling up of hydrogen production.[3] So far, about 66 % of global hydrogen is produced through coal gasification and methane reforming at a relatively low cost, but this method produces CO_2 as a by-product, which dramatically accelerates global climate change.[4] As an alternative, electrochemical water splitting through the hydrogen evolution reaction (HER) is a promising method to produce hydrogen due to its efficient and easy coupling with a renewable energy source.[5] However, there is still a problem that platinum-based catalysts, the most active catalyst for HER found so far, are too costly to be used in the industry.[6-8]

For these reasons, non-noble metal-based electrocatalysts are in the spotlight. Among them, research on molybdenum-based electrocatalysts (such as MoS_2[9-11], Mo_xB_y[12-14], Mo_2C[11, 15-16], and MoP[17-19]) is being carried out actively in both acid and alkaline electrolytes due to the low-cost and high activity. Moreover, as reported previously,[12, 14, 20] revealing the structure-activity relationship of that materials is also a crucial part of designing optimal electrocatalysts. In terms of crystal structure, molybdenum borocarbide (Mo_2BC) is a very interesting material because it consisted of both boride and carbide sub-cell; Mo_6B trigonal prisms, and Mo_6C octahedron and the

zigzag chains of boron atom are formed through the Mo_6B trigonal prisms **(Figure 5.1a)**.[21-22] In the structure, Mo_6B trigonal prisms and the Mo_6C octahedron are the same sub-cell with that of β-MoB (space group *Cmcm)* and α-MoC (space group *Fm-3m)* respectively. Therefore, we assume that it could show reasonable activity because it contains β-MoB and α-MoC substructure which has good HER activity as mentioned before. However, no one focuses on Mo_2BC as an electrocatalyst. So far, it has been studied as a hard coating material because it has been predicted by *ab initio* calculations that not only a high stiffness but also moderate ductility is shown. [23-25] In this chapter, we apply Mo_2BC to HER electrocatalyst in both acid and alkaline electrolytes for the first time and suggest the synergy effect of β-MoB and α-MoC substructure in Mo_2BC crystal structure. Moreover, a suitable electrode preparation method beyond dense electrode, which was studied in our previous report[26], is proposed for maximizing HER activity.

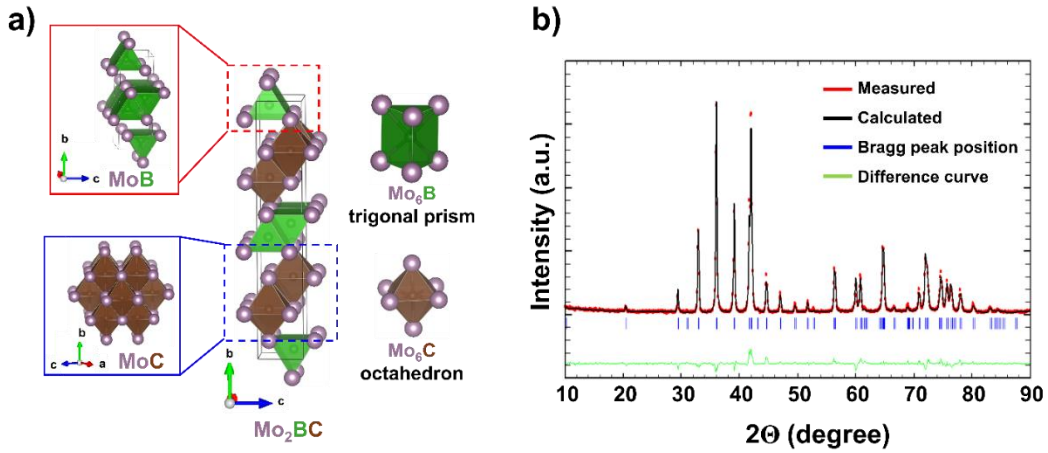

Figure 5.1. (a) Projection of the crystal structure and **(b)** Refined powder XRD pattern of Mo_2BC

Table 5.1. Crystallographic information for the prepared Mo_2BC. The reported lattice parameters from the ICSD database are given in square brackets.

Sample	Mo_2BC	β-MoB	α-MoC
Space group	*Cmcm*	*Cmcm*	*Fm-3m*
***a* [Å]**	3.0842(4)-[3.083]	3.1395(5)-[3.1482]	4.280(2)-[4.2700]
***b* [Å]**	17.348(2)-[17.356]	8.484(1)-[8.4858]	4.280(2)-[4.2700]
***c* [Å]**	3.0476(4)-[3.045]	3.0717(5)-[3.0778]	4.280(2)-[4.2700]
V [Å^3]	163.06(4)-[162.93]	81.81(2)-[82.223]	78.40(5)-[77.854]
Calc. density	8.746	9.503	9.146

5.2. Experimental Section

5.2.1. Sample preparation

Appropriate amount of molybdenum (Mo) powder, boron (B) powder, and carbon black (C) (total mass 0.3 g, the atomic ratio of Mo:B=1:1 for MoB, Mo:C=1:1 for MoC, and Mo:B:C=2:1:1 for Mo_2BC)) were weighed, mixed and pressed into pellets. The pellets were melted in a copper crucible, which is cooled by water, using a tungsten tip at 40 A current under an argon atmosphere until homogeneous melting occurred.

5.2.2. Electrode preparation

Disk type electrode: Arc-melted Mo_2BC sample was put into the epoxy adhesive and dried overnight at room temperature. The top and bottom of the dried samples were ground using a grinder (South Bay Technology, USA) until it forms a disk shape. The ground samples were attached to a copper sheet using conductive silver paste. The exposed surface of the copper sheet was covered with epoxy adhesive and dried overnight at room temperature.

Pellet type electrode: Arc-melted Mo_2BC sample was ground in two ways: mortar and 24 h ball-milling using MSE PRO^{TM} Planetary Mill (PMV1-0.4L). 50 mg of ground Mo_2BC sample were pressed into a pellet and the pressed pellet was put into the epoxy adhesive and dried overnight at room temperature. The top and bottom of the dried samples were ground using a grinder. Then, it attached to the copper sheet using conductive silver paste. The exposed surface of the copper sheet was covered with epoxy adhesive and dried overnight at room temperature.

Pt/C: 1 mg of 20% Pt/C powder was sonicated in 95 µl IPA and 5 µl Nafion solution. Then, the 3.0 µl of the solution was dropwise on carbon cloth (0.3×0.3 cm^2). The carbon cloth was dried for 5 h at 50 °C in an oven (the catalyst loading: ~0.3 mg/cm^2). The dried carbon cloth was attached to the copper sheet using conductive silver paste. The exposed surface of the copper sheet was covered with epoxy adhesive and dried overnight at room temperature.

5.3. Results and Discussion

As shown in **Figure 5.1b** and **Table 5.1**, the prepared sample is a single phase and the calculated lattice parameters are *a*=3.0842(4) Å, *b*=17.348(2) Å, and *c*=3.0476(4) Å with orthorhombic structure and space group *Cmcm*. The diffraction peaks and refined lattice parameters of the sample are matched very well with reported previous data.[27] Moreover, to analyze the surface chemical composition and the core-level binding energy of Mo_2BC, X-ray photoelectron spectroscopy (XPS) is performed. **Figure 5.2** is showing the oxidation states of the molybdenum, boron, and carbon species on the analyzed

surfaces. The binding energy of Mo^0 in Mo_2BC is localized at 228.2 eV, 231.4 eV, and peaks at 229.2 eV and 232.6 eV are assigned MoO_2.[28-29] Although it is difficult to interpret the B1s peak due to low intensity, it is possible to resolve the binding energy and the B^0 peaks in Mo_2BC appear at 188.5 eV and 187.8 eV. These similar values can be found in previous reports.[29] Moreover, the high-resolution C 1s spectrum shows the 3 peaks at 282.6 eV, 284.5 eV, and 286.4 eV which are related to the C bond in Mo_2BC, C-C bond, and C-O bond, respectively. [28, 30] The C-C bond peak at 284.5 eV derives from adventitious carbon,[28] and the C-O and MoO_2 peaks reveal that the O atom exists on the surfaces of the synthesized sample due to exposure to air.[31] However, the peak intensity of oxide is so low that the effect on the catalytic activity can be ignored.

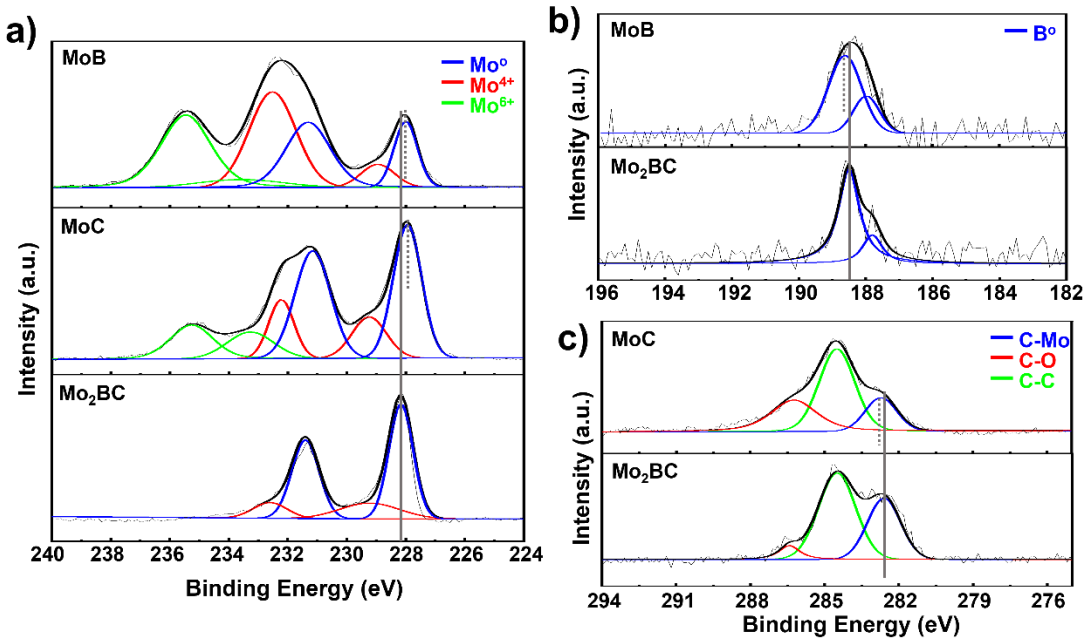

Figure 5.2. X-ray photoelectron spectroscopy spectra of **(a)** Mo 3d, **(b)** B 1s, and **(c)** C 1s of β-MoB, α-MoC, and Mo_2BC.

On the other hand, the electrical resistivity is measured using four-wire resistance measurements, and the temperature-dependent resistivity of Mo_2BC at the temperature range of 2 K to 300 K is plotted in **Figure 5.3**. It is worth noting that the resistivity at room temperature (300 K) is very low (82 $\mu\Omega\, cm$) although it is the bulk samples. It implies that Mo_2BC is showing high electrical conductivity properties and there is a high density of states at the Fermi energy level.[32] Moreover, **Figure 5.3** is showing a sharp decrease in resistivity at the temperature of ~6 K which means it has a superconductor property. It is matched well with the previous report.[27]

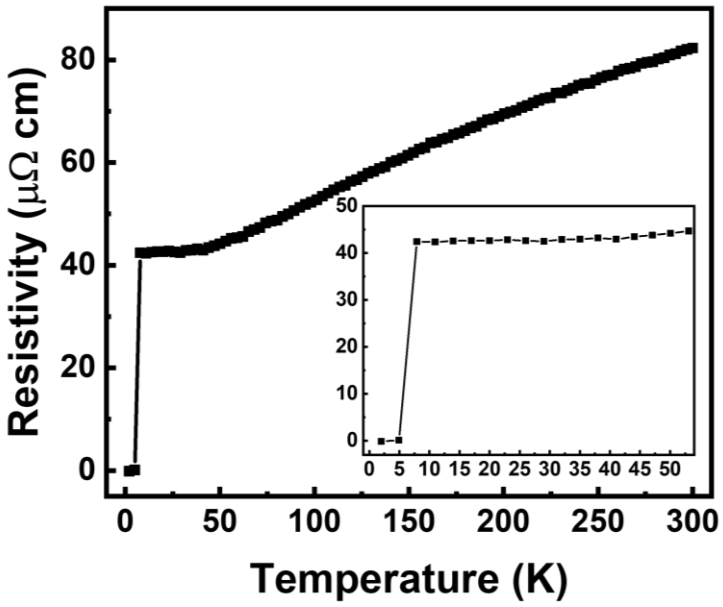

Figure 5.3. Temperature-dependent electrical resistivity of Mo_2BC. Inset: a small range of temperatures.

For electrochemical measurements, a typical three-electrode system which is composed of the counter electrode (graphite rod), reference electrode (saturated calomel electrode), and the working electrode (disk type electrode) has been used. To compare

HER activity of Mo_2BC with β-MoB and α-MoC, we synthesize a single phase of β-MoB and α-MoC by arc melting method **(Figure 5.4)** and measure the HER activity. As shown in the *iR*-corrected polarization curves in **Figure 5.5**, Mo_2BC requires -182 mV to achieve a current density of -10 mA/cm^2 (η_{10}=-182 mV). It is 36 mV and 73 mV less overpotential than β-MoB (η_{10}=-218 mV) and α-MoC (η_{10}=-255 mV), respectively. It indicates that Mo_2BC is a highly active HER electrocatalyst as we expected. The better activity of Mo_2BC can be explained by electron density. As shown in XPS data in **Figure 5.2**, the binding energy of Mo^0 in Mo_2BC (**Figure 5.2a**) is larger and the binding energy of B^0 (**Figure 5.2b**) and C-Mo (**Figure 5.2c**) in Mo_2BC is smaller than that in β-MoB and α-MoC. It indicates that electron transfer from Mo to B and C in Mo_2BC structure because the binding energy generally has a negative correlation with surface electron density.[33] The large electron density of Mo in β-MoB and α-MoC might contribute to reduce the strength of Mo-H because the antibonding states will shift to lower energy and become more occupied.[34] Due the the weak strength of Mo-H, β-MoB, and α-MoC have lower activity than Mo_2BC. It also be proved by Tafel slope in **Figure 5.5b**. According to the HER mechanism in an acid electrolyte, three possible reactions can be the rate-determining step (RDS); Volmer reaction (Tafel slope ~120 mV/dec), Heyrovsky reaction (Tafel slope ~40 mV/dec), and Tafel reaction (Tafel slope ~30 mV/dec).[35-36] The Tafel slope of β-MoB (91.1 mV/dec.) and α-MoC (134 mV/dec.) is close to the that of Volmer reaction, which means that there is limitation of H adsorption due to week Mo-H strength. Therefore, Mo_2BC with lower electron density in Mo shows better activity and lower Tafel slope than others because it has moderate Mo-H strength.

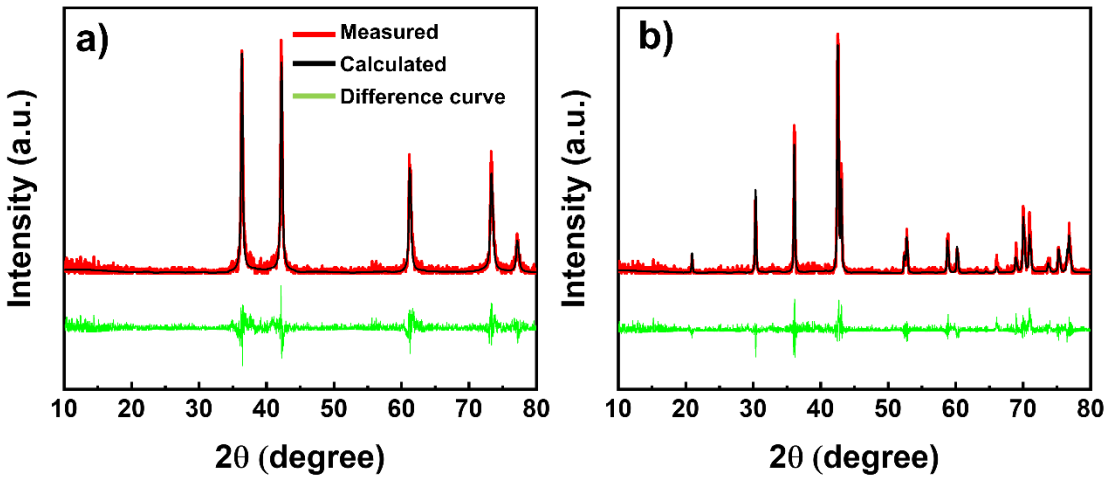

Figure 5.4. Refined powder XRD pattern of (**a)** α-MoC and **(b)** β-MoB

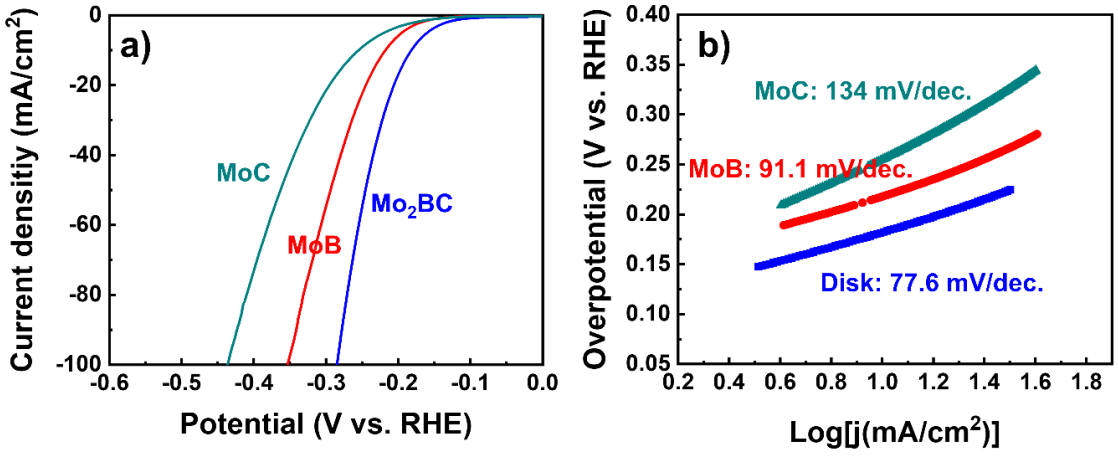

Figure 5.5. (a) Polarization curves of β-MoB, α-MoC, and Mo_2BC. The data is recorded in 0.5 M H_2SO_4 at a scan rate of 5 mV/s with *iR*-correction. **(b)** Tafel plots were obtained using the polarization curves in (a).

To study the effect of the electrode preparation method and maximize the activity, we made three different types of electrodes: disk, bulk pellet, and ball-milled pellet

electrode. As shown in **Figure 5.6b**, the particle size of the ball-milled samples is ≤1 μm and is more homogenous than bulk powder (**Figure 5.6a**). Moreover, It shows a broader XRD pattern than bulk powder (**Figure 5.6c**). This means that the particle size decreased significantly after ball milling.[37] Then, the bulk and ball-milled powder are pressed into a pellet and attached to a copper sheet using a conductive silver paste to make the electrode.

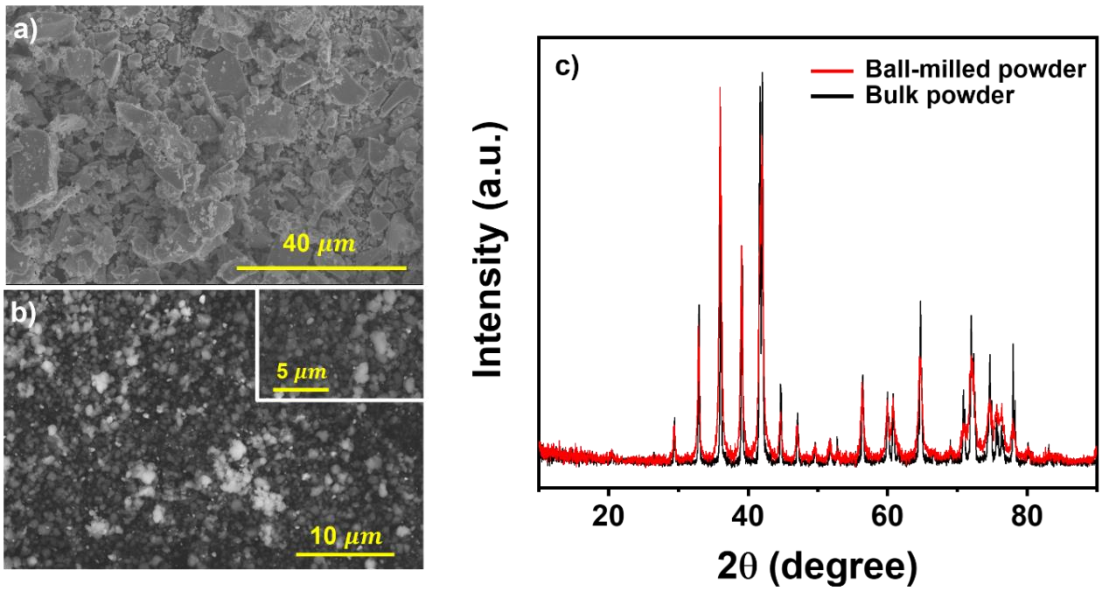

Figure 5.6. SEM morphologies of **(a)** bulk (gound by hand) and **(b)** ball-milled Mo_2BC powder. **(c)** Powder X-ray diffraction patterns of bulk and ball-milled powder.

Figure 5.7a shows the *iR*-corrected polarization curves of different types of Mo_2BC electrodes recorded at a scan rate of 5 mV/s in 0.5 M H_2SO_4. The ball-milled pellet has the lowest overpotential of η_{10}=-94.7 mV than the bulk pellet (η_{10}=-145 mV) and disk (η_{10}=-182 mV). As decreasing particle size, HER activity increase. As shown in **Figure 5.8c**, the particle in the ball-milled pellet surface is much smaller and denser than

the bulk pellet and it contributes to exposing a more active site. It is supported by the electrochemically active surface area (ECSA). The ECSA can be estimated from the electrochemical double-layer capacitance (C_{DL}) of the catalyst surface[38] and the C_{DL} measured using electrochemical impedance spectroscopy (EIS) based on the equation (1),[39, 40] where Q_0 is constant with units of $[F\ s^{a-1}]$ and a is related to the phase angle of the frequency response ($0 \leq a \leq 1$, a=1 for perfect capacitor). Then it is normalized by a geometric surface area (**Figure 5.9, Table 5.2**). This is the best method for comparing C_{DL} of electrodes with different roughness because the roughness can be revised by a value.[41]

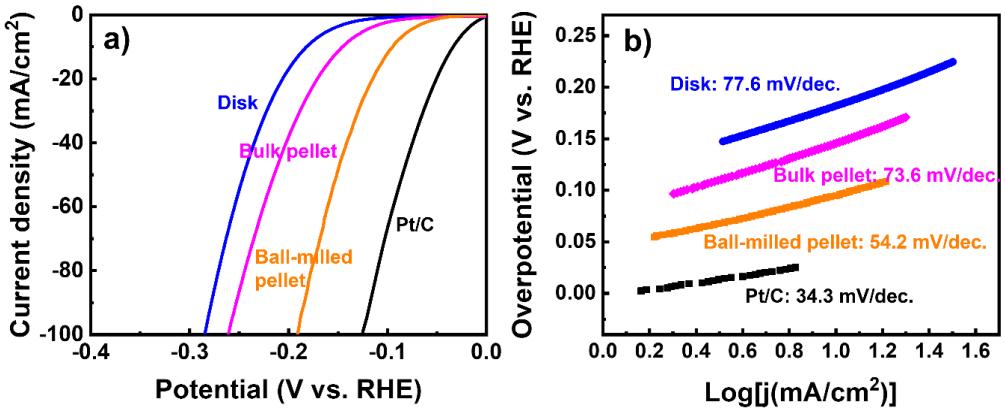

Figure 5.7. (a) Polarization curves of Mo_2BC made by various electrode preparation methods. The data is recorded in 0.5 M H_2SO_4 at a scan rate of 5 mV/s with *iR*-correction. **(b)** Tafel plots were obtained using the polarization curves in (a).

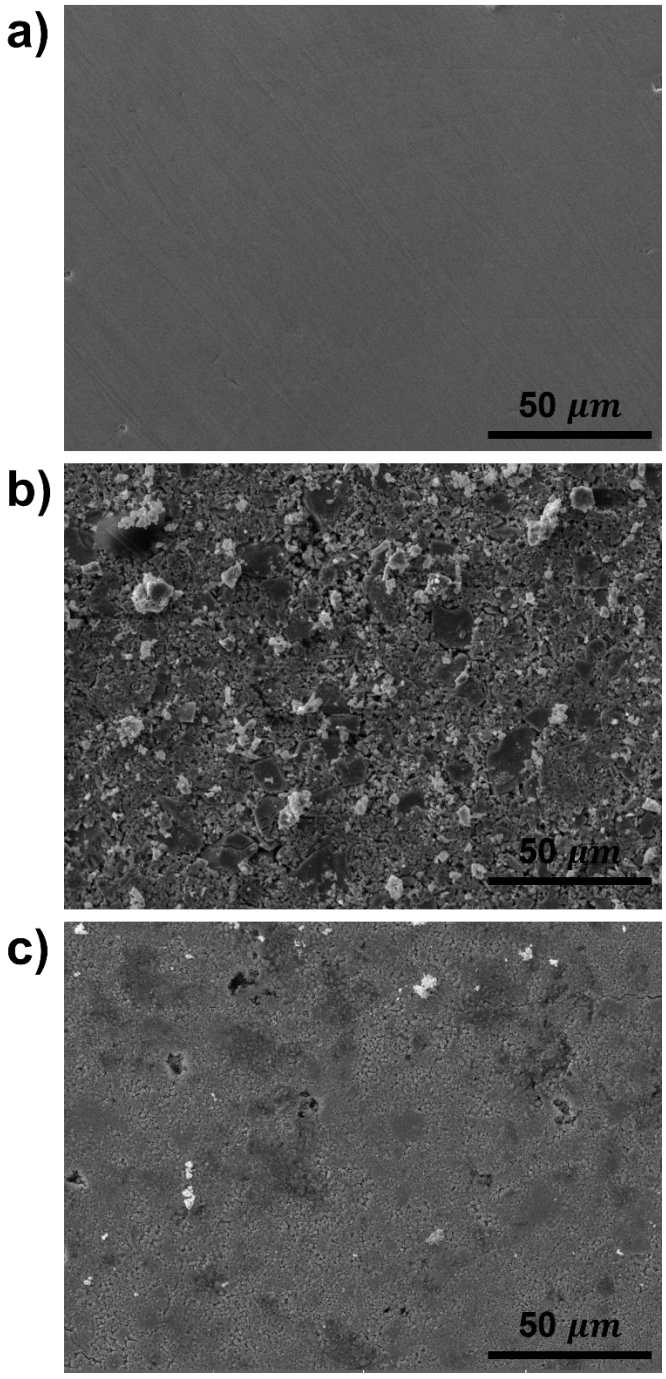

Figure 5.8. SEM morphologies of the various electrode surface. **(a)** disk **(b)** bulk pellet, and **(c)** ball-milled pellet type electrode.

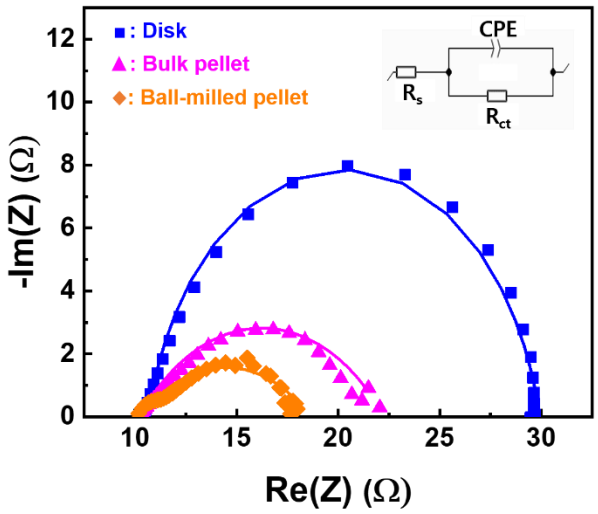

Figure 5.9. Nyquist plot representations of the electrochemical impedance spectra of various Mo_2BC electrode types in 0.5 M H_2SO_4. The point is experimental data and the line is the fitting line.

Table 5.2. Fitted EIS data

Electrolyte	Eletrode type	R_s [42]	R_{ct} [42]	Q_0 [F s^{a-1}]	a	C_{DL} [mF/cm^2]
0.5 M H_2SO_4	Disk	10.83	18.96	6.12 e^{-4}	0.8949	0.434
	Bulk pellet	10.33	11.88	1.21 e^{-2}	0.5660	7.76
	Ball-milled pellet	10.27	8.36	2.98 e^{-2}	0.4590	14.6

The Nyquist plot can be fitted using an equivalent circuit model consisting of series resistance (Rs, solution resistance, and Rct, charge transfer resistance) and a constant phase element (CPE). As shown in the fitted data in **Table 5.2**, the calculated C_{DL} of the ball-milled pellet (14.6 mF/cm^2) is much higher than that of the bulk pellet (7.76 mF/cm^2) and disk type electrode (0.434 mF/cm^2). It means that pellet-type electrodes have a much higher C_{DL} at the same geometry surface. This large increment of C_{DL} can affect the improved HER activity of the ball-milled pellet electrode. It is very

interesting because only the difference in the electrode preparation method affects a huge increase in C_{DL}.

$$C_{DL} = \left[Q_0 \left(\frac{1}{R_s} + \frac{1}{R_{ct}} \right)^{(a-1)} \right]^{1/a} \quad (1)$$

Figure 5.7b shows the corresponding Tafel plots of the disk, bulk pellet, ball-milled pellet type electrode, and Pt/C near the onset potential. The fitted Tafel plot for Pt/C and ball-milled pellet exhibit a Tafel slope of 34.3 and 54.2 mV/dec indicating that the Tafel and Heyrovsky reaction is likely the RDS, respectively. On the other hand, the Tafel slope of the disk (77.6 mV/dec) and bulk pellet (73.6 mV/dec) is the median Tafel slope of the Volmer reaction and Heyrovsky reaction. It deviates from the theoretical value, indicating that they follow complex mechanisms. Besides, it is larger than that of the ball-milled pellet which means the HER efficiency of the ball-milled pellet is better than others.[26] It corresponds to other electrochemical analyses.

The long cycle stability of the catalysts is a key factor for practical application. For the durability test, CV analysis was performed for 5000 cycles in acid solution (**Figure 5.10a, c, e**). The final polarization curves exhibit highly efficient HER activity without degradation after 5000 cycles. Besides, further long-term electrochemical stability tests of the samples are continuously conducted at 10 mA/cm^2 for 24 h (**Figure 5.10b,d, f**). It also shows all of the electrodes maintain stable current density during the test demonstrating the excellent stability of Mo_2BC.

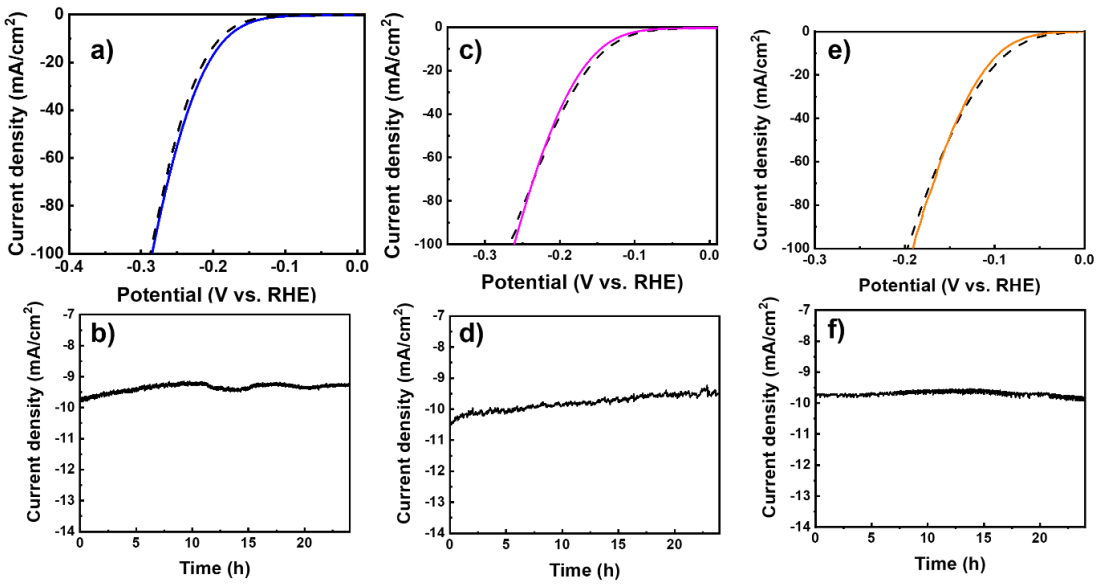

Figure 5.10. HER stability measurement of **(a)** disk, **(c)** bulk pellet, and **(e)** ball-milled pellet Mo_2BC electrode before and after 5000 cycles with a scan rate of 100 mV s^{-1} in 0.5 M H_2SO_4, Chronoamperometry curve of **(b)** disk, **(d)** bulk pellet, and **(f)** ball-milled pellet Mo_2BC electrode for 24 h.

Interestingly, Mo_2BC also exhibits excellent HER activity in the alkaline electrolyte. We further investigated the HER performance of the ball-milled pellet electrode in 1 M KOH, which showed the best performance. It shows an overpotential of -117 mV is required to approach the current density of 10 mA/cm^2 (**Figure 5.11a**) and a Tafel slope is calculated to be 64.7 mV/dec (**Figure 5.11b**) with excellent durability (**Figure 5.11c, d**). The electrochemical water splitting system is widely used not only under strongly acidic (proton exchange membrane)[43], but also in neutral (microbial electrolysis cell)[44], or strongly basic media (alkaline electrolysis)[45]. Therefore, the high HER activity of Mo_2BC in both acid and the alkaline electrolyte is a substantial result.

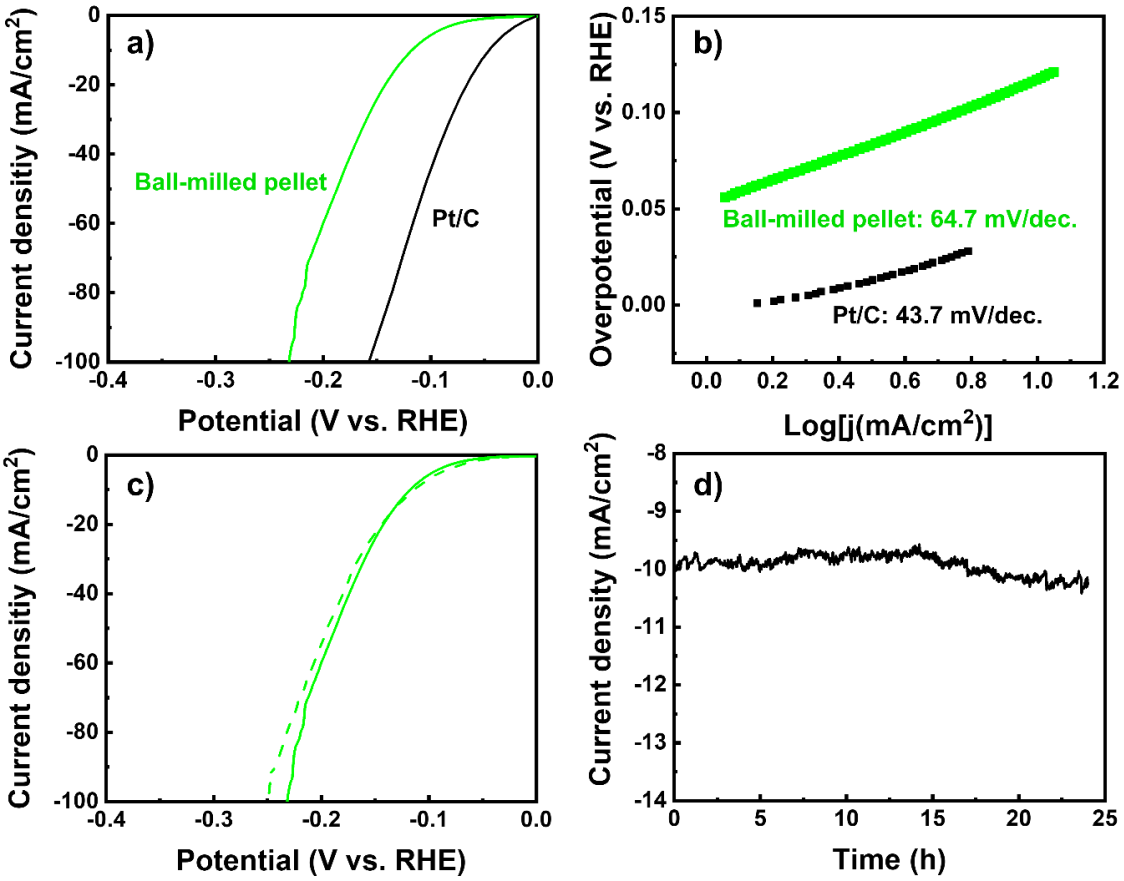

Figure 5.11. (a) Polarization curves of ball-milled pellet type Mo_2BC electrode recorded in 1 M KOH at a scan rate of 5 mV/s with *iR*-correction. **(b)** Tafel plots were obtained using the polarization curves in (a). **(c)** Stability measurement of before and after 5000 cycles with a scan rate of 100 mV s^{-1} in 1 M KOH, and **(d)** Chronoamperometry curve for 24 h.

5.4. Conclusion

In summary, a highly crystalline single phase of Mo_2BC has been synthesized by an arc-melting method and applied to HER electrocatalyst for the first time. As we expected, Mo_2BC is a highly active HER electrocatalyst and has better HER activity than the β-MoB and α-MoC. The electron density from XPS can explain the splendid activity. According to XPS data, the electron in Mo transfers to B and C in the Mo_2BC structure.

Therefore, the electron density in Mo of Mo_2BC is lower than the β-MoB and α-MoC, and it contributes to moderate Mo-H strength. After that, 3 types of electrodes (disk, bulk pellet, and ball-milled pellet) were made to study the effect of the electrode preparation method. Among the electrodes, a ball-milled pellet type electrode, which had a higher C_{DL}, showed the best HER activity with stable durability. Moreover, it also exhibited excellent activity in an alkaline solution. We suggest that this material has huge potential as a new material for HER electrocatalyst.

5.5. Reference

1. Abe, J.; Ajenifuja, E.; Popoola, O., Hydrogen energy, economy and storage: review and recommendation. *International Journal of Hydrogen Energy* **2019**.
2. Bockris, J. M.; Appleby, A., The hydrogen economy-an ultimate economy. *Environ. This Month* **1972,** *1* (1), 29-35.
3. Brandon, N.; Kurban, Z., Clean energy and the hydrogen economy. *Philosophical Transactions of the Royal Society A: Mathematical, Physical and Engineering Sciences* **2017,** *375* (2098), 20160400.
4. Edwards, P. P.; Kuznetsov, V. L.; David, W. I.; Brandon, N. P., Hydrogen and fuel cells: towards a sustainable energy future. *Energy policy* **2008,** *36* (12), 4356-4362.
5. Cook, T. R.; Dogutan, D. K.; Reece, S. Y.; Surendranath, Y.; Teets, T. S.; Nocera, D. G., Solar energy supply and storage for the legacy and nonlegacy worlds. *Chemical reviews* **2010,** *110* (11), 6474-6502.
6. Zhao, Y.; Kamiya, K.; Hashimoto, K.; Nakanishi, S., In situ CO2-emission assisted synthesis of molybdenum carbonitride nanomaterial as hydrogen evolution electrocatalyst. *Journal of the American Chemical Society* **2014,** *137* (1), 110-113.
7. Anantharaj, S.; Kennedy, J.; Kundu, S., Microwave-initiated facile formation of Ni3Se4 nanoassemblies for enhanced and stable water splitting in neutral and alkaline media. *ACS applied materials & interfaces* **2017,** *9* (10), 8714-8728.
8. Sivanantham, A.; Shanmugam, S., Nickel selenide supported on nickel foam as an efficient and durable non-precious electrocatalyst for the alkaline water electrolysis. *Applied Catalysis B: Environmental* **2017,** *203*, 485-493.
9. Kibsgaard, J.; Chen, Z.; Reinecke, B. N.; Jaramillo, T. F., Engineering the surface structure of MoS 2 to preferentially expose active edge sites for electrocatalysis. *Nature materials* **2012,** *11* (11), 963.
10. Sun, K.; Zeng, L.; Liu, S.; Zhao, L.; Zhu, H.; Zhao, J.; Liu, Z.; Cao, D.; Hou, Y.; Liu, Y., Design of basal plane active MoS2 through one-step nitrogen and

phosphorus co-doping as an efficient pH-universal electrocatalyst for hydrogen evolution. *Nano Energy* **2019,** *58*, 862-869.
11. Laursen, A. B.; Kegnæs, S.; Dahl, S.; Chorkendorff, I., Molybdenum sulfides—efficient and viable materials for electro-and photoelectrocatalytic hydrogen evolution. *Energy & Environmental Science* **2012,** *5* (2), 5577-5591.
12. Park, H.; Encinas, A.; Scheifers, J. P.; Zhang, Y.; Fokwa, B. P., Boron-dependency of molybdenum boride electrocatalysts for the hydrogen evolution reaction. *Angewandte Chemie International Edition* **2017,** *56* (20), 5575-5578.
13. Vrubel, H.; Hu, X., Molybdenum boride and carbide catalyze hydrogen evolution in both acidic and basic solutions. *Angewandte Chemie International Edition* **2012,** *51* (51), 12703-12706.
14. Park, H.; Zhang, Y.; Scheifers, J. P.; Jothi, P. R.; Encinas, A.; Fokwa, B. P., Graphene-and phosphorene-like boron layers with contrasting activities in highly active Mo2B4 for hydrogen evolution. *Journal of the American Chemical Society* **2017,** *139* (37), 12915-12918.
15. Liao, L.; Wang, S.; Xiao, J.; Bian, X.; Zhang, Y.; Scanlon, M. D.; Hu, X.; Tang, Y.; Liu, B.; Girault, H. H., A nanoporous molybdenum carbide nanowire as an electrocatalyst for hydrogen evolution reaction. *Energy & Environmental Science* **2014,** *7* (1), 387-392.
16. Ge, C.; Jiang, P.; Cui, W.; Pu, Z.; Xing, Z.; Asiri, A. M.; Obaid, A. Y.; Sun, X.; Tian, J., Shape-controllable synthesis of Mo2C nanostructures as hydrogen evolution reaction electrocatalysts with high activity. *Electrochimica Acta* **2014,** *134*, 182-186.
17. Wang, T.; Du, K.; Liu, W.; Zhu, Z.; Shao, Y.; Li, M., Enhanced electrocatalytic activity of MoP microparticles for hydrogen evolution by grinding and electrochemical activation. *Journal of Materials Chemistry A* **2015,** *3* (8), 4368-4373.
18. Xing, Z.; Liu, Q.; Asiri, A. M.; Sun, X., Closely interconnected network of molybdenum phosphide nanoparticles: a highly efficient electrocatalyst for generating hydrogen from water. *Advanced materials* **2014,** *26* (32), 5702-5707.
19. Yang, J.; Zhang, F.; Wang, X.; He, D.; Wu, G.; Yang, Q.; Hong, X.; Wu, Y.; Li, Y., Porous molybdenum phosphide nano-octahedrons derived from confined phosphorization in UIO-66 for efficient hydrogen evolution. *Angewandte Chemie International Edition* **2016,** *55* (41), 12854-12858.
20. Lee, E.; Park, H.; Joo, H.; Fokwa, B. T. P., Unexpected Correlation Between Boron Chain Condensation and HER Activity in Highly Active Vanadium Borides: Enabling Predictions. *Angewandte Chemie International Edition* **2020**.
21. Lejay, P.; Chevalier, B.; Etourneau, J.; Hagenmuller, P., Influence of some metal substitutions on the superconducting behaviour of molybdenum borocarbide. *Journal of the Less Common Metals* **1981,** *82*, 193-200.
22. Bovin, J.-O.; O'Keeffe, M.; Stenberg, L., Planar defects in Mo2BC. An electron microscope study. *Journal of Solid State Chemistry* **1977,** *22* (2), 221-231.

23. Emmerlich, J.; Music, D.; Braun, M.; Fayek, P.; Munnik, F.; Schneider, J., A proposal for an unusually stiff and moderately ductile hard coating material: Mo2BC. *Journal of Physics D: Applied Physics* **2009,** *42* (18), 185406.
24. Mansouri Tehrani, A.; Oliynyk, A. O.; Rizvi, Z.; Lotfi, S.; Parry, M.; Sparks, T. D.; Brgoch, J., Atomic Substitution to Balance Hardness, Ductility, and Sustainability in Molybdenum Tungsten Borocarbide. *Chemistry of Materials* **2019,** *31* (18), 7696-7703.
25. Barua, P.; Hossain, M.; Ali, M.; Uddin, M.; Naqib, S.; Islam, A., Effects of transition metals on physical properties of M2BC (M= V, Nb, Mo and Ta): A DFT calculation. *Journal of Alloys and Compounds* **2019,** *770*, 523-534.
26. Park, H.; Zhang, Y.; Lee, E.; Shankhari, P.; Fokwa, B. P., High-Current-Density HER Electrocatalysts: Graphene-like Boron Layer and Tungsten as Key Ingredients in Metal Diborides. *ChemSusChem* **2019,** *12* (16), 3726-3731.
27. Lejay, P.; Chevalier, B.; Etourneau, J.; Hagenmuller, P.; Peshev, P., The borocarbides Mo2− xWxBC (0⩽×⩽ 1.1), a new family of refractory superconducting materials. *Synthetic Metals* **1981,** *4* (2), 139-145.
28. Escamilla, R.; Carvajal, E.; Cruz-Irisson, M.; Morales, F.; Huerta, L.; Verdin, E., XPS study of the electronic density of states in the superconducting Mo 2 B and Mo 2 BC compounds. *Journal of materials science* **2016,** *51* (13), 6411-6418.
29. Mavel, G.; Escard, J.; Costa, P.; Castaing, J., ESCA surface study of metal borides. *Surface Science* **1973,** *35*, 109-116.
30. Dong, J.; Wu, Q.; Huang, C.; Yao, W.; Xu, Q., Cost effective Mo rich Mo 2 C electrocatalysts for the hydrogen evolution reaction. *Journal of Materials Chemistry A* **2018,** *6* (21), 10028-10035.
31. Xiao, X.; Tao, L.; Li, M.; Lv, X.; Huang, D.; Jiang, X.; Pan, H.; Wang, M.; Shen, Y., Electronic modulation of transition metal phosphide via doping as efficient and pH-universal electrocatalysts for hydrogen evolution reaction. *Chemical science* **2018,** *9* (7), 1970-1975.
32. Ge, Y.; Ma, S.; Bao, K.; Tao, Q.; Zhao, X.; Feng, X.; Li, L.; Liu, B.; Zhu, P.; Cui, T., Superconductivity with high hardness in Mo 3 C 2. *Inorganic Chemistry Frontiers* **2019,** *6* (5), 1282-1288.
33. Zhuang, Z.; Li, Y.; Li, Z.; Lv, F.; Lang, Z.; Zhao, K.; Zhou, L.; Moskaleva, L.; Guo, S.; Mai, L., MoB/g-C3N4 interface materials as a Schottky catalyst to boost hydrogen evolution. *Angewandte Chemie* **2018,** *130* (2), 505-509.
34. Li, Q.; Zou, X.; Ai, X.; Chen, H.; Sun, L.; Zou, X., Revealing activity trends of metal diborides toward pH-universal hydrogen evolution electrocatalysts with Pt-like activity. *Advanced Energy Materials* **2019,** *9* (5), 1803369.
35. Chung, D. Y.; Park, S.-K.; Chung, Y.-H.; Yu, S.-H.; Lim, D.-H.; Jung, N.; Ham, H. C.; Park, H.-Y.; Piao, Y.; Yoo, S. J., Edge-exposed MoS 2 nano-assembled structures as efficient electrocatalysts for hydrogen evolution reaction. *Nanoscale* **2014,** *6* (4), 2131-2136.
36. Sheng, W.; Gasteiger, H. A.; Shao-Horn, Y., Hydrogen oxidation and evolution reaction kinetics on platinum: acid vs alkaline electrolytes. *Journal of The Electrochemical Society* **2010,** *157* (11), B1529-B1536.

37. Jothi, P. R.; Yubuta, K.; Fokwa, B. P., A simple, general synthetic route toward nanoscale transition metal borides. *Advanced Materials* **2018,** *30* (14), 1704181.
38. Trasatti, S.; Petrii, O., Real surface area measurements in electrochemistry. *Pure and applied chemistry* **1991,** *63* (5), 711-734.
39. Orazem, M. E.; Tribollet, B., *Electrochemical impedance spectroscopy*. John Wiley & Sons: 2017.
40. McCrory, C. C.; Jung, S.; Peters, J. C.; Jaramillo, T. F., Benchmarking heterogeneous electrocatalysts for the oxygen evolution reaction. *Journal of the American Chemical Society* **2013,** *135* (45), 16977-16987.
41. Alexander, C. L.; Tribollet, B.; Orazem, M. E., Contribution of surface distributions to constant-phase-element (CPE) behavior: 1. Influence of roughness. *Electrochimica Acta* **2015,** *173*, 416-424.
42. Alghamdi, M.; Lohmann, M.; Li, J.; Jothi, P. R.; Shao, Q.; Aldosary, M.; Su, T.; Fokwa, B. P.; Shi, J., Highly efficient spin–orbit torque and switching of layered ferromagnet Fe3GeTe2. *Nano letters* **2019,** *19* (7), 4400-4405.
43. Le Goff, A.; Artero, V.; Jousselme, B.; Tran, P. D.; Guillet, N.; Métayé, R.; Fihri, A.; Palacin, S.; Fontecave, M., From hydrogenases to noble metal–free catalytic nanomaterials for H2 production and uptake. *Science* **2009,** *326* (5958), 1384-1387.
44. Kundu, A.; Sahu, J. N.; Redzwan, G.; Hashim, M., An overview of cathode material and catalysts suitable for generating hydrogen in microbial electrolysis cell. *international journal of hydrogen energy* **2013,** *38* (4), 1745-1757.
45. LeRoy, R., Industrial water electrolysis: present and future. *International Journal of Hydrogen Energy* **1983,** *8* (6), 401-417.

Chapter 6.

$Fe_5Ge_2Te_2$: Iron-rich Layered Chalcogenide for Highly Efficient Hydrogen Evolution

Recent research on van der Waals (vdW) metal chalcogenides electrocatalysts for the hydrogen evolution reaction (HER) has been devoted to finding new catalysts with active basal planes. Here, we report on experimental and theoretical investigations of the HER activity of a recently discovered iron-rich vdW spintronic material, $Fe_5Ge_2Te_2$ (FG2T) in alkaline media (1 M KOH). We show that a densified electrode of FG2T requires an overpotential of only −90.5 mV to drive a current density of 10 mA/cm^2. Free energy calculations of hydrogen adsorption using density functional theory (DFT) proved that the numerous sites present on the hexagonal Te layer are more active than those found in the recently proposed Fe_3GeTe_2 (FGT) catalyst, supporting higher activity for the new Fe-richer catalyst. Like in FGT, XPS analysis has found that a thin oxide layer covers the active FG2T layers, suggesting the real active surface to be a hybrid FG2T/oxide layer. These results strengthen the idea of continued screening of iron-based vdW materials to replace the non-abundant platinum group electrocatalysts toward HER and other electrocatalytic processes.

***E. Lee**, Amir A. Rezai, Diana Luong, Johan A. Yapo, Boniface P. T. Fokwa*

6.1. Introduction

Recent climate change-related issues and the increase in energy demand are helping to accelerate the transition from non-renewable and polluting fuels such as fossil fuels and coal to renewable and non-toxic ones.[1-2] Due to its cleanliness, sustainability, and high energy density hydrogen has been accepted as one of the most promising, eco-friendly alternatives.[3-5] Furthermore, hydrogen can be produced through water electrolysis, which is an environmental-friendly method.[6-8] Many research efforts in this field are focused on developing new, efficient, and cost-effective electrocatalysts to replace current scarce and expensive platinum-group metals and noble-metal compounds.[9-10]

Van der Waals (vdW) materials such as transition metal dichalcogenides (TMDs) are among the most studied HER electrocatalysts due to their unique physical and chemical properties.[11-14] The majority of these vdW materials do not show basal plane electrochemical activity toward HER, making them almost inactive in bulk form. Therefore, to improve the basal plane activity, various surface modifications such as defect engineering[15-17], doping[18-20], and interfacial engineering[21-23] have been successfully applied. Recent research is focused on the development of new basal-plane-active vdW materials that will induce greater electrochemical activity post-surface modifications. Among all the vdW layered materials, some are being considered for spintronic applications, especially $Fe_{3-x}GeTe_2$ (FGT), which is an itinerant ferromagnet below a Curie temperature of 220 K.[24-25] Similar to other TMDs, FGT is currently being considered as a potential electrocatalyst candidate for several reactions, including the

oxygen-evolution reaction (OER) and nitrogen reduction reaction (NRR).[14, 26-27] We have recently reported the first experimental and theoretical investigations of the HER activity of FGT.[28] We found that a densified FGT electrode requires the smallest overpotential ($\eta_{10} = -0.105$ V) among all bulk TMDs reported so far and that it displays no significant HER activity loss after 3000 cycles and 24 hours of operation in an alkaline electrolyte. Furthermore, density functional theory (DFT) calculations of the free energy of hydrogen adsorption (ΔG_H) showed that FGT's flat Te basal plane is as active as the puckered Te layer in monoclinic $MoTe_2$ (1T'-$MoTe_2$),[29] thus supporting the basal plane activity of FGT. All active basal plane TMDs so far have puckered chalcogenide basal planes including 3R-MoS_2[30], making FGT the first electrocatalyst with an active flat basal plane. Additionally, DFT calculations presented an active edge layer (106) that is superior to the basal plane, supporting the observed increased activity with particle size reduction. The discovery of FGT's HER activity has put other iron-based vdW materials into focus, especially those richer in iron as they will ultimately be less expensive than FGT. Herein, we report on the experimental and theoretical investigations of the HER activity of a recently discovered iron-richer phase that is structurally related to FGT, $Fe_{5-x}Ge_2Te_2$ (FG2T).

6.2. Experimental Section

6.2.1. Sample preparation

For the synthesis of FG2T, stoichiometric amounts of iron (Fe – 99.9%, Sigma Aldrich), germanium (Ge – 99.99%, Alfa Aesar), and tellurium (Te – 99.99%, Alfa

Aesar) powders were mixed homogeneously and pressed into a pellet. The pellet was loaded in a quartz glass ampoule and sealed under vacuum, where it was then placed into a tube furnace and heated to a temperature of 800°C. After 36 hours, the tube was slowly cooled to room temperature for 5 days.

In order to exfoliate the FG2T layers and break them into smaller particles, the crushed powder was loaded into an ethanol vial and sonicated for 2 hours in an ice-water bath (SharperTek 50/60 Hz). Then the sample was removed and dried for further measurements.

6.2.2. Electrode preparation

Pt/C: 1 mg of the sample was sonicated in 95 µl Isopropyl Alcohol (IPA) and 5 µl Nafion solution. Then, 5.0 µl of the solution was added dropwise on carbon cloth (0.3×0.3 cm^2). The carbon cloth was dried for 5 h at 50 °C in an oven (the catalyst loading: ~0.55 mg/cm^2). The dried carbon cloth was attached to the copper sheet using conductive silver paste. The exposed surface of the copper sheet was covered with epoxy adhesive and dried overnight at room temperature.

Pellet electrode: 70 mg of sonicated FG2T was pressed by a hydraulic pump at room temperature. Then, the pressed pellet ($diameter \approx 5mm$) was put into the epoxy adhesive and dried overnight at room temperature. The epoxy covered the edges of the pellet making the electrode only exposable on the surface. The top and bottom of the dried samples were polished (South Bay Technology, USA). The polished sample was attached to a copper sheet using conductive silver paste. The exposed surface of the copper sheet was covered with epoxy adhesive and dried overnight at room temperature.

6.3. Computational Details

The density functional theory (DFT) was used to determine the H-binding energy (ΔE_h) on the modeled {00l} surface of FG2T. The total energy calculations for the surface were done using the projector augmented wave[31] coded in the Vienna ab initio simulation package (VASP).[32] In addition, all the VASP calculations done here employed the generalized gradient approximation (GGA) with the exchange and correlation functionals treated by the Perdew-Burke-Enzerhoff (PBE)[33] and revised PBE[34] with Pade approximation methods for the structure relaxations and single-point energy calculations respectively. The convergence threshold for the ionic relaxation loop was set to 0.02 eV/Å in force and the cutoff energy for the plane wave calculations was set to 500 eV. Spin polarization functions were also calculated just for the single-point energy calculations of the surface. The Brillouin zone integrations were carried out with a 7 x 23 x 3 k-point mesh using the Monkhorst-Pack automatic grid generation mode.

To construct the surface first the unit cell of $Fe_5Ge_2Te_2$ was obtained and the cell shape, volume and positions of all the atoms were all optimized with VASP. To make the surface we need to cleave the bulk material in the desired direction and then add vacuum spacing in that same direction to create 2D slabs (surface supercells) with the proper surface exposed. In this work, a 2 x 2 x 2 supercell was created from their respective unit cells. Then about 15 Å of vacuum space was added in the {00l} direction of the supercell in order to expose the (002) basal plane and ensure that there would be no inter-slab interactions. This resulted in 2D slabs with four Te layers and 1 vdW gap layer between two $Fe_5Ge_2Te_2$ layers. During the structural relaxation step, both the stress tensor and

forces were calculated allowing the position of all the atoms to move and the magnitude of the unit cell vectors to change.

To calculate the Gibbs free energy (ΔG_H) for H adsorption to predict the HER activity of the different HER active sites on the surface the equation $\Delta G_H = \Delta E_H + \Delta E_{ZPE} - T\Delta S$ was used, where ΔE_H is the H-surface binding energy computed using DFT, ΔE_{ZPE} is the zero-point energy difference between adsorbed H and free H_2 and $T\Delta S$ is the temperature and entropy contribution terms. One thing to note here is that ΔE_{ZPE} is usually very small, between 0.01 to 0.05 eV[35] which is around or less than the chemical accuracy target of 1 kcal·mol^{-1} or 0.043 eV that is desired for ab initio computational methods, so it can be neglected here and the equation can be simplified to $\Delta G_H = \Delta E_H - T\Delta S$. $T\Delta S$ is calculated with the approximation $T\Delta S \approx \frac{1}{2}TS°(H2)$, where $T = 298.15\,K$ and $S°(H2) = 130.7\,J \cdot mol^{-1}K^{-1}$.[36] Lastly, the equation used to solve for the binding energy of hydrogen ΔE_H was $\Delta E_H = E[surface + nH] - E[surface + (n-1)H] - \frac{1}{2}E[H_2]$. Here $E[surface + nH]$ and $E[surface + (n-1)H]$ are the total energies of the surface with n and $n-1$ hydrogen atoms adsorbed on it respectively and calculated using VASP, and $\frac{1}{2}E[H_2]$ is half of the energy of one gas phase, diatomic hydrogen molecule.

6.4. Results and Discussion

Compared to FGT, FG2T has an extra Fe_2Ge layer that allows for a change in crystal symmetry from a hexagonal (space group $P6_3/mmc$) to trigonal (space group

$P\bar{3}m1$). In fact, FG2T's crystal structure consists of a "$Fe_{5-x}Ge_2$" substructure sandwiched between two layers of Te atoms weakly bonded by vdW forces on adjacent slabs as seen in **Figure 6.1c.**

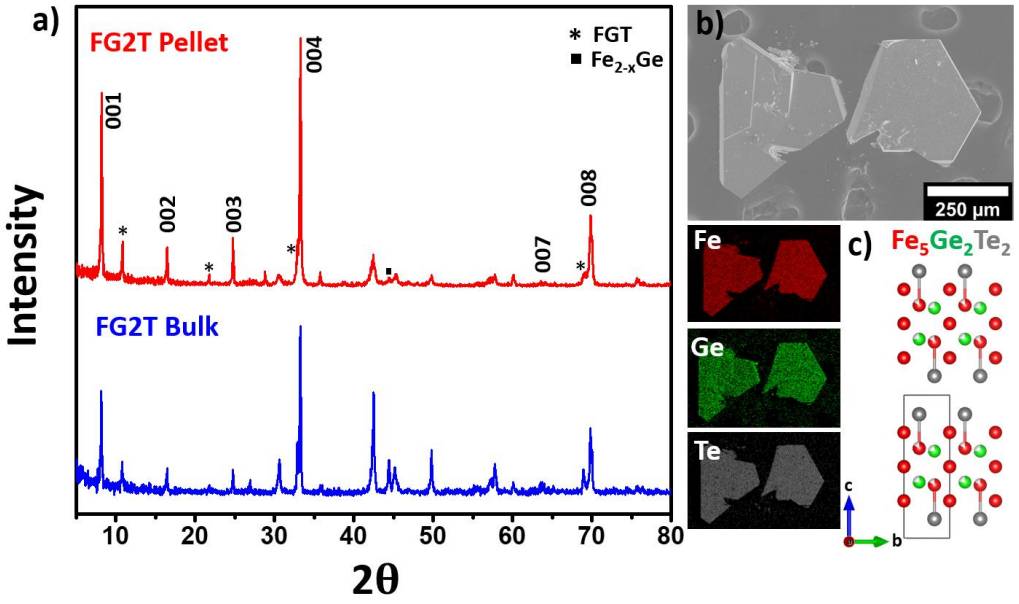

Figure 6.1. a) Powder X-ray diffraction patterns of FG2T samples (bulk and pellet). **b)** SEM images and EDS mappings of as-synthesized FGT crystals. **c)** Crystal structure of FG2T (* represents FGT peaks, ■ represents $Fe_{2-x}Ge$ peaks)

The FG2T sample was synthesized via our previous method[37] through a solid-state reaction. The as-grown crystals were characterized by powder X-ray diffraction (PXRD) for their phase purity (**Figure 6.1a**), scanning electron microscope (SEM) for their morphology, and energy dispersive X-ray spectroscopy (EDS) mapping (**Figure 6.1b**) for elemental distribution. The PXRD pattern displayed FG2T as the majority phase (90 %), according to Rietveld Refinement. However small percentages of FGT (8.3 %) and $Fe_{2-x}Ge$ (1.7 %) were identified as side phases. Intensity mismatches were also

observed for the (*00l*) peaks, similar to the previously reported FGT,[28] which is due to the preferred orientation of these layered crystals (**Figure 6.1b**). The EDS mapping on the FG2T crystals confirmed the existence and homogenous distribution of all three elements (**Figure 6.1b**).

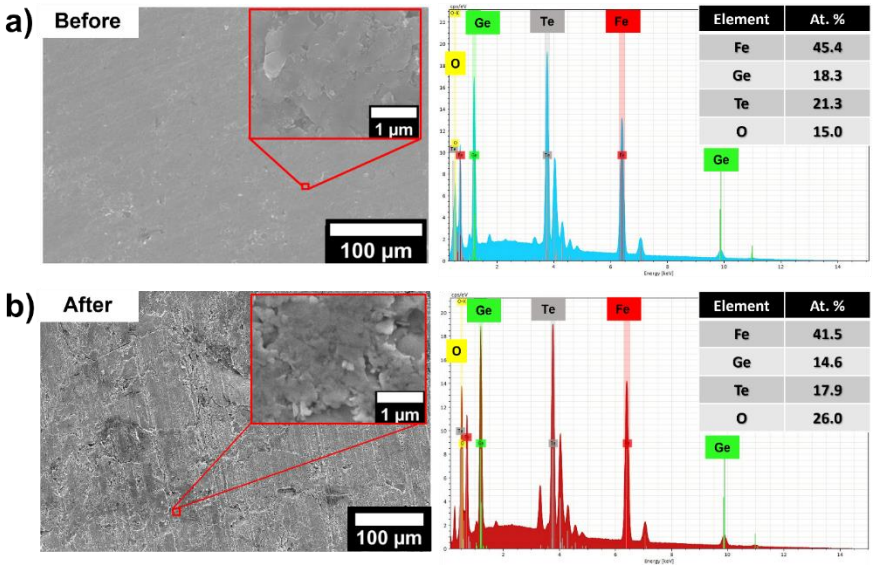

Figure 6.2. SEM micrograph and EDX of the densified FG2T pellet electrode's surface **a)** before, and **b)** after HER measurement.

In our previous report on the HER activity of FGT[28], we showed that a pressed pellet electrode from an ultrasonicated powder sample of this vdW material has the best performance versus its bulk or sonicated powder electrode forms. Therefore, we have studied the HER activity of FG2T based on its similarly pressed pellet electrode. FG2T powder was dispersed in ethanol and ultrasonicated in an ice-water bath for two hours. The ultrasonicated powder was then compressed under a hydraulic press at room temperature providing a densified disk. The PXRD pattern of the densified pellet

displayed an increased preferred orientation toward the [*00l*] direction similar to the previously reported FGT (**Figure 6.1a**). The preferred orientation was also observed for the small FGT impurity. SEM micrograph confirmed the highly oriented sheet-like morphology of the electrode's surface (**Figure 6.2**).

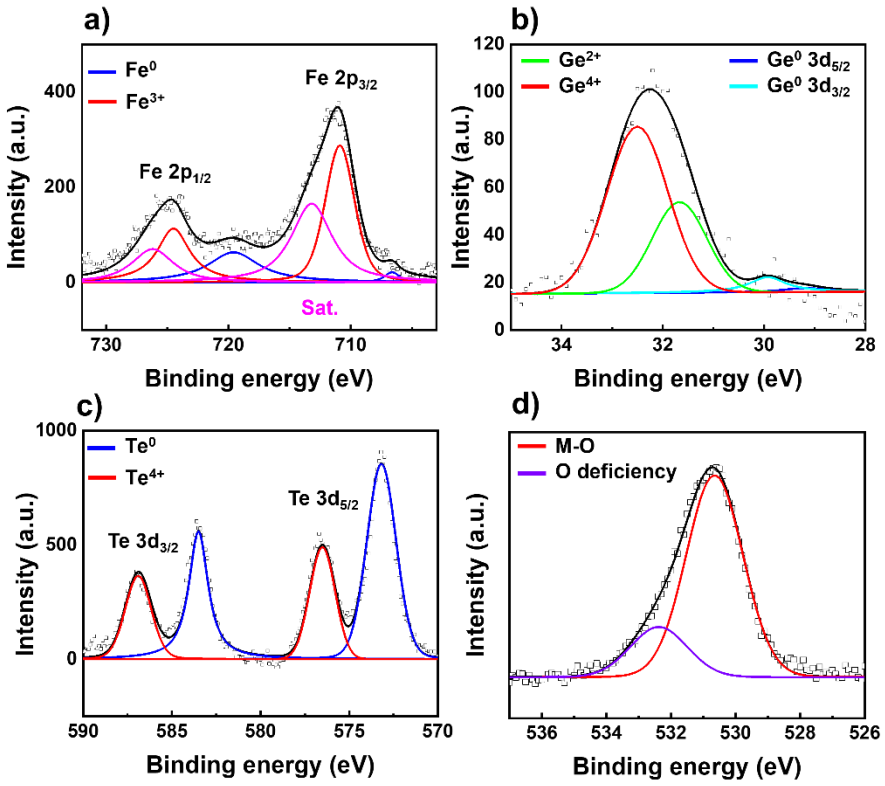

Figure 6.3. X-ray photoelectron spectroscopy spectra of **a)** Fe 2p, **b)** Ge 3d, **c)** Te 3d, and **d)** O 1s for the sonicated FG2T pellet (Before HER meansurement). Experimental and fitting data are indicated as (□) and solid lines, respectively.

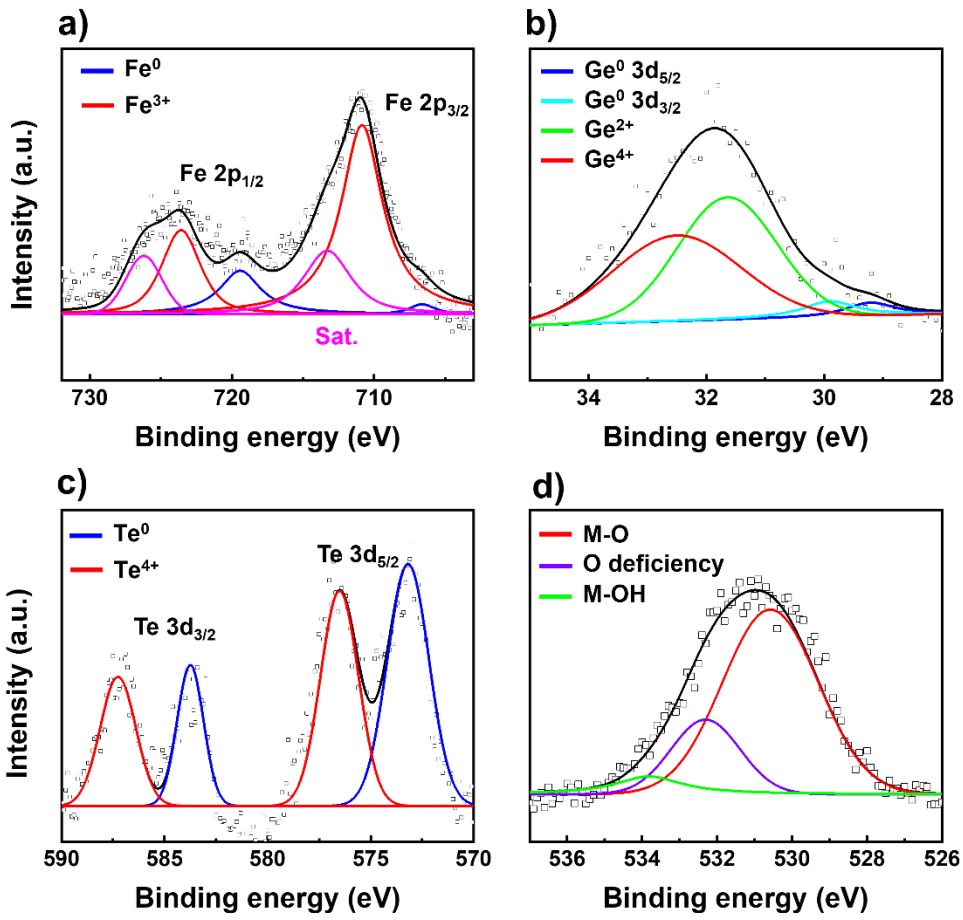

Figure 6.4. X-ray photoelectron spectroscopy spectra of **a)** Fe 2p, **b)** Ge 3d, **c)** Te 3d, and **d)** O 1s of the FG2T pellet after HER measurement. Experimental and fitting data are indicated as (□) and solid lines, respectively.

Table 6.1. XPS peak position and full width at half maximum (FWHM) parameters for Fe 2p, Ge 3d, and Te 2d of FG2T.

	Species	Peak position (eV)	FWHM (eV)
Sonicated pellet Before HER	Fe^0	706.6, 719.6	1.5, 5
	Fe^{3+}	710.9, 724.5	2.8, 3.1
	Satellite	713.2, 726.2	4.0, 4.0
	Ge^0	29.2, 29.9	1.0, 0.9
	Ge^{2+}	31.7	1.3
	Ge^{4+}	32.5	1.4
	Te^0	573.2, 583.5	2.0, 1.3
	Te^{4+}	576.5, 586.9	1.7, 1.7
	M-O	530.6	2.07
	O deficiency	532.4	2.08
Sonicated pellet After HER	Fe^0	706.6, 719.4	2.2, 3.5
	Fe^{3+}	710.9, 723.6	3.5, 3.2
	Satellite	713.3, 726.2	3.9, 3.0
	Ge^0	29.2, 29.9	1.0, 1.1
	Ge^{2+}	31.6	2.0
	Ge^{4+}	32.5	2.6
	Te^0	573.2, 583.7	2.4, 1.5
	Te^{4+}	576.5, 587.2	2.2, 2.0
	M-O	530.6	3.01
	O deficiency	532.3	2.16
	M-OH	533.8	2.16

X-ray photoelectron spectroscopy (XPS) was applied to investigate the surface chemical composition and the core-level binding energy of the FG2T pellet before (**Figure 6.3**) and after HER activity measurements (**Figure 6.4**). The results of the analyzed surface show the oxidation states of the Fe 2p, Ge 3d, and Te 3d species

(**Figure 6.3** and **Table 6.1)**. As seen in **Figure 6.3**, the spectra are very similar to those reported for FGT,[28, 38-41] thus only similarities and differences will be discussed here. Similar to FGT, the high-resolution Fe 2p spectrum shows two peaks at 706.6 eV/719.6 eV which originate from the metallic iron (Fe^0 in FG2T) as well as two other doublets at 710.9 eV and 724.5 eV (with 713.2 and 726.2 eV satellites) [28, 38-41] ascribed to Fe^{3+} from the surface oxide layer. The high-resolution Ge 3d spectrum (**Figure 6.3b**) depicts peaks at 29.2/29.9 eV assigned to metallic germanium (Ge^0 in FG2T) and others at 31.7 eV (Ge^{2+}) and 32.5 eV (Ge^{4+}) corresponding to germanium oxide peaks.[28, 42-44] The high-resolution Te 3d spectrum (**Figure 6.3c**) contains peaks at 573.2/583.5 eV ascribed to metallic tellurium (Te^0 in FG2T) while those at 576.5/586.9 eV are assigned to Te^{4+}.[28, 45-46] The O 1s spectrum (**Figure 6.3d**) indicates peaks at 530.6 eV and 532.4 eV assigned to metal oxide and oxygen deficiencies on the surface, respectively.[47-48] The sonication decreases the particle size, thus exposing more surface area to oxidation. However, the FG2T peaks are still clearly detectable by XPS, suggesting that the formed oxide layer is thin. In fact, the peak intensities of Te^0 are higher than those of the oxidized Te-species, indicating that Te^0 is the most abundant species on the surface due to the Te-terminated vdW atomic structure in FG2T. This finding contrasts with that of FGT which showed dominating oxidized Te-species instead. Interestingly, our DFT calculations (discussed later in the manuscript) clearly show that FG2T is intrinsically active, showing even more active sites on its basal Te plane than FGT. Nevertheless, the presence of surface oxidized species may affect the HER activity, suggesting that the real active surface may be a complex hybrid FG2T/oxide layer.

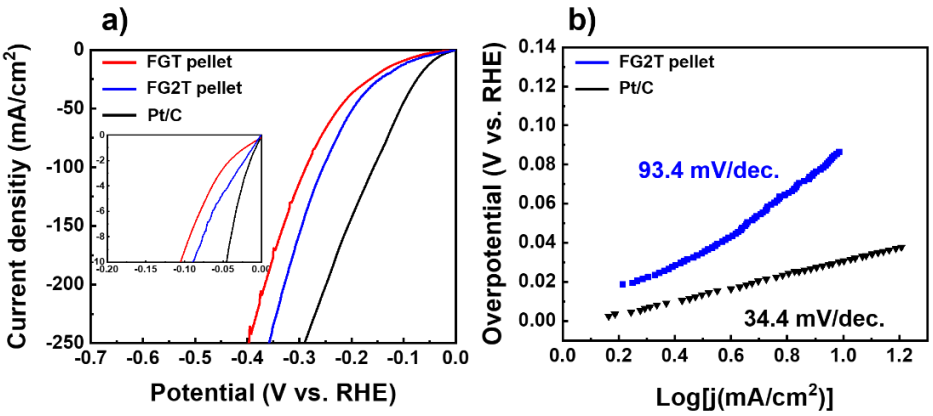

Figure 6.5. a) Polarization curves of sonicated FG2T pellet, sonicated FGT pellet from the previous study[28], and Pt/C. The data is recorded in 1 M KOH at a scan rate of 1 mV/s with iR-correction. **b)** Tafel plots obtained using the polarization curves in **a)**.

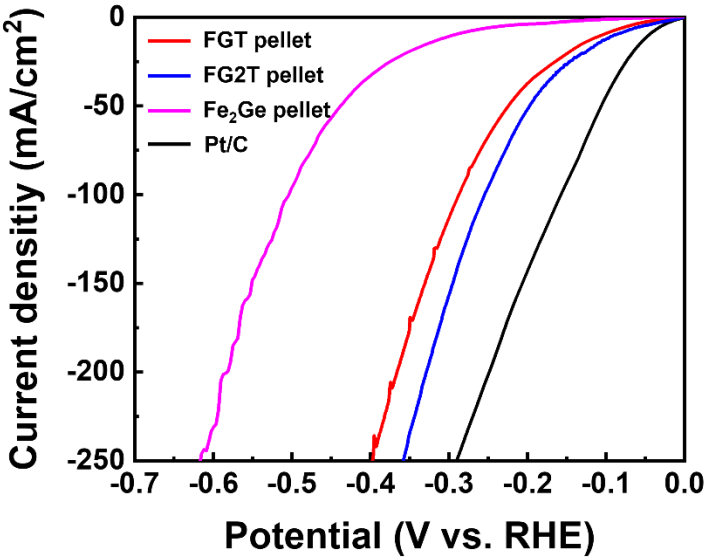

Figure 6.6. Polarization curves of the impurity $Fe_{2-x}Ge$ pellet, the sonicated FG2T pellet, the sonicated FGT pellet, and Pt/C.

The HER activity of the FG2T pellet electrode was examined in a 1 M KOH electrolyte. To rule out any effect of the $Fe_{2-x}Ge$ impurity, its activity was studied, and it

showed very poor activity (**Figure 6.6**). The linear sweep voltammetry (LSV) curve of the sonicated FG2T pellet exhibits an overpotential of η_{10} = -90.5 mV at 10 mA/cm^2 and η_{250} = -358 mV at a high current density of 250 mA/cm^2 (**Figure 6.5a**). Consequently, the FG2T pellet shows a 13.8% improved overpotential (at 10 mA/cm^2) if compared to the previously reported FGT pellet (η_{10} = -105 mV and η_{250} = -398 mV).[28] To support this result, we have estimated the electrochemical active surface area (ECSA) from cyclic voltammetry (CV) measured at various scan rates. ECSA was estimated from the electrochemical double-layer capacitance (C_{dl}). The C_{dl} is linearly proportional to the effective surface area. This is because the double layer charging current (i_c) is proportional to the electrochemically active surface area of the electrode.[49-50] Therefore, large C_{dl} indicates more exposed surface-active sites. **Figure 6.7** shows that the C_{dl} value (55.2 mF/cm^2) of the FG2T pellet is larger than that reported for the FGT pellet (52.7 mF/cm^2),[28] confirming the presence of more active sites on FG2T. Furthermore, electrochemical impedance spectroscopy (EIS) data in **Figure 6.8 and Table 6.2** also indicate that FG2T is a more efficient electrocatalyst than FGT. The first parallel components (R_{ct} and CPE) indicate the charge transfer kinetics and the second parallel components (R and C) reflect the hydrogen adsorption behavior.[51] In fact, the charge transfer resistance (R_{ct}), which is derived from the Nyquist plot, shows that the FG2T electrode has a smaller R_{ct} (8.06 Ω) than the FGT electrode (9.71 Ω)[28], supporting the idea that electrons will move more efficiently on the FG2T electrode surface and thus boosting its charge transfer rate during HER.

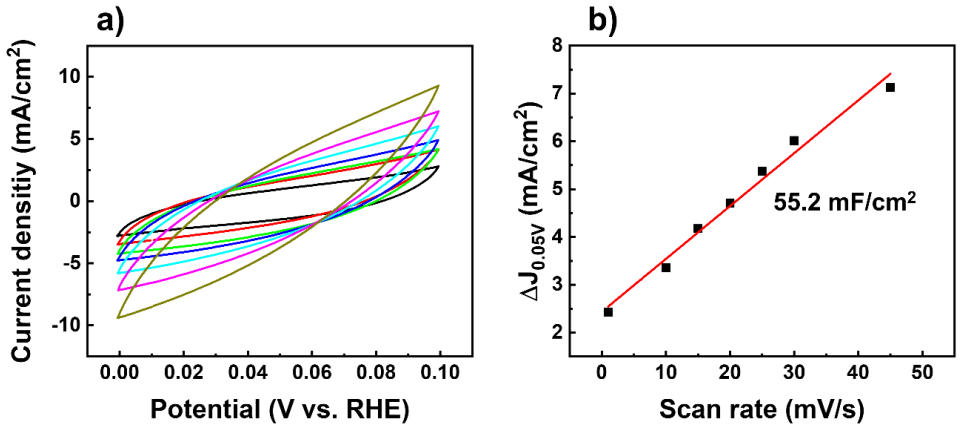

Figure 6.7. a) Cyclic voltammetry profiles and **b)** linear fitting of the capacitive currents versus scan rates obtained from cyclic voltammetry tests at 0.05 V vs. RHE to estimate C_{dl} for FG2T pellet electrode in 1 M KOH.

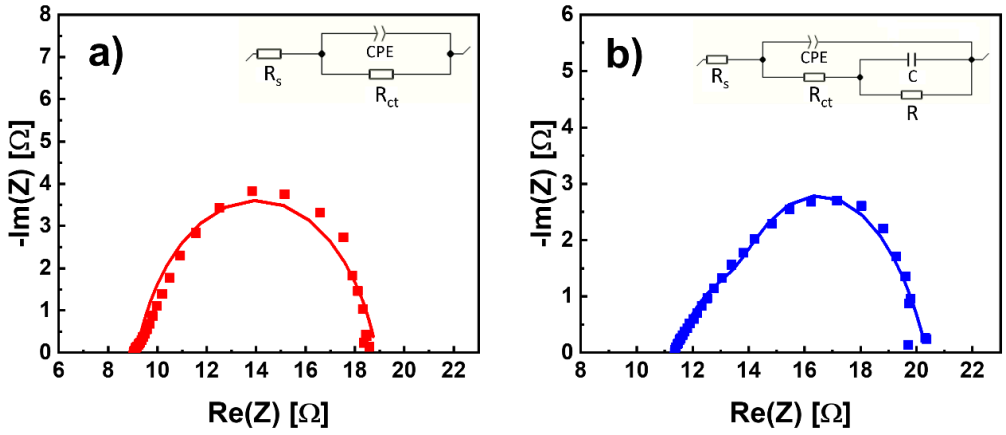

Figure 6.8. Electrochemical impedance spectroscopy (EIS) Nyquist plots of FGT[28] (previous work) and FG2T pellet electrode in 1 M KOH. The points represent the experimental data and the lines are the fitting data.

Table 6.2. Fitted EIS data

Electrode	R_s [Ω]	R_{ct} [Ω]	CPE [F s^{a-1}]	a	R [Ω]	C [F]	
$Fe_5Ge_2Te_2$	11.41	8.06	0.01636	0.6643	2.425	0.021	This work
Fe_3GeTe_2	9.16	9.71	0.0210	0.813	-	-	Ref. 28

The Tafel slope was used to understand the reaction kinetics by evaluating the rate-determining step. From the Tafel plots (**Figure 6.5b**) extracted from the LSV curve, the FG2T pellet demonstrates a high HER activity with a lower Tafel slope (93.4 mV/dec) versus the FGT pellet electrodes (97.3mV/dec),[28] indicating a more efficient HER with faster kinetics for FG2T. In the alkaline electrolyte, there are three microscopic steps as shown below.[52]

Tafel reaction: $2\ H_{ad} \leftrightarrows H_2$ (Tafel slop= ~30 mV/dec)

Heyrovsky reaction: $H_{ad} + e^- + H_2O \leftrightarrows H_2 + OH^-$ (Tafel slop= ~40 mV/dec)

Volmer reaction: $H_{ad} + OH^- \leftrightarrows H_2O + e^-$ (Tafel slop= ~120 mV/dec)

The FG2T pellet's Tafel slope is located between that proposed for the Volmer reaction (Tafel slope ~120 mV/dec) and that of the Heyrovsky reaction (Tafel slope ~40 mV/dec), hinting at a complex reaction as often observed for highly active bulk catalysts.[53] Moreover, continuous CV measurements were used to evaluate the stability of FG2T (**Figure 6.9a**), and the electrode showed very little degradation after 3000 cycles. Besides, at a fixed overpotential, a chronoamperometric test (**Figure 6.9b**) of the electrode yields a stable current density of about 10 mA/cm^2 for 24 h, proving its high durability under these HER conditions. The high stability of the FG2T electrode was further confirmed by XPS, which showed almost identical spectra before (**Figure 6.3**) and after (**Figure 6.4**) HER activity measurements. In the O 1s spectrum, a hydroxide peak appears after electrochemical measurement due to the alkaline electrolyte. However, the amount is so small that it did not affect the activity.

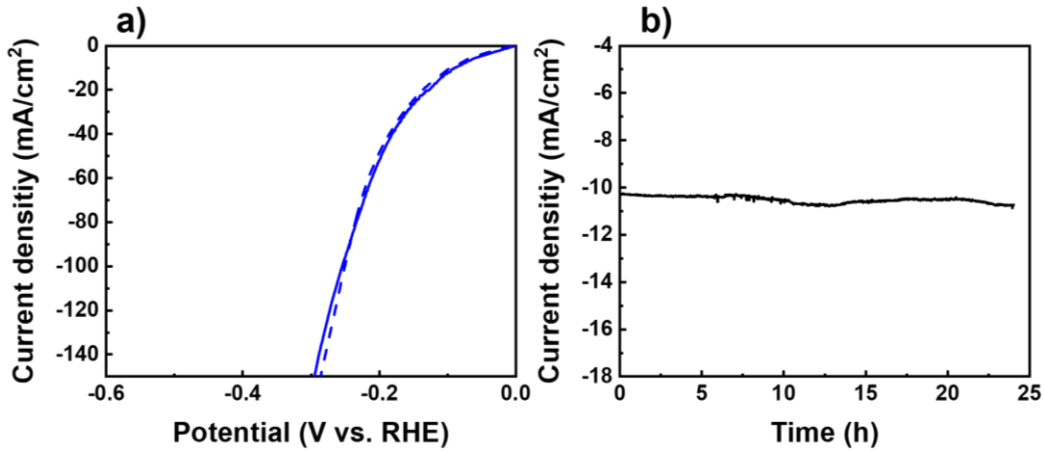

Figure 6.9. HER stability measurement of FG2T pellet **a)** before and after 3000 cycles with a scan rate of 100 mV/s, **b)** Chronoamperometry curve for 24 h in 1 M KOH.

According to the XPS results discussed above Te^0 from the FG2T basal plane is the dominant species on the FG2T's surface and electrochemical activity studies proved that FG2T is more active than FGT. Consequently, we hypothesized that FG2T should have a more active Te basal plane than FGT. To verify this hypothesis first-principles DFT calculations were carried out on a model of FG2T's basal plane (002) using a unit cell doubled in the *c*-direction. The Gibbs free energy (ΔG_H) values of different H-adsorption sites were calculated. ΔG_H for atomic hydrogen adsorbed on a catalyst surface is widely accepted as a descriptor of HER activity as it was shown to correlate with the experimentally measured HER activity for a variety of systems.[54-56] Theoretically, the optimal HER activity is achieved when the ΔG_H value is close to zero, as it ensures that the reaction rates for both an H atom adsorbing and H_2 molecule desorbing onto/off the surface are maximized. For the all-tellurium (002) layer, four sites were considered as shown in **Figure 6.10b**: (1) on top (Top) of a Te atom, two hollow sites (2 & 3), one above a Fe atom (Hol-1) and another above a Ge atom (Hol-2), and lastly (4) a bridge

(Brdg) site between two Te atoms. The calculated ΔG_H values are 1.53 eV, 0.91 eV, 1.90 eV, and 1.04 eV for the Top, Hol-1, Hol-2, and Brdg sites, respectively. As **Figure 6.10a** illustrates, almost all sites are also present in the recently discovered HER-active FGT, with the missing site in FGT being the bridge site that converged to the top site after structure optimization.[28] Interestingly, comparing the ΔG_H values of the two materials (**Figure 6.10a**) shows that the FG2T-Brdg site is more active than the best FGT site (Top). Furthermore, the two most active FG2T sites (Hol-1 and Brdg) have lower ΔG_H than all FGT sites. These theoretical results not only support the experimental findings that FG2T is more HER active than FGT, but it also possesses a basal plane that is more active than other highly studied chalcogenides such as 1T'-$MoTe_2$ [57] and 3R-MoS_2 [30].

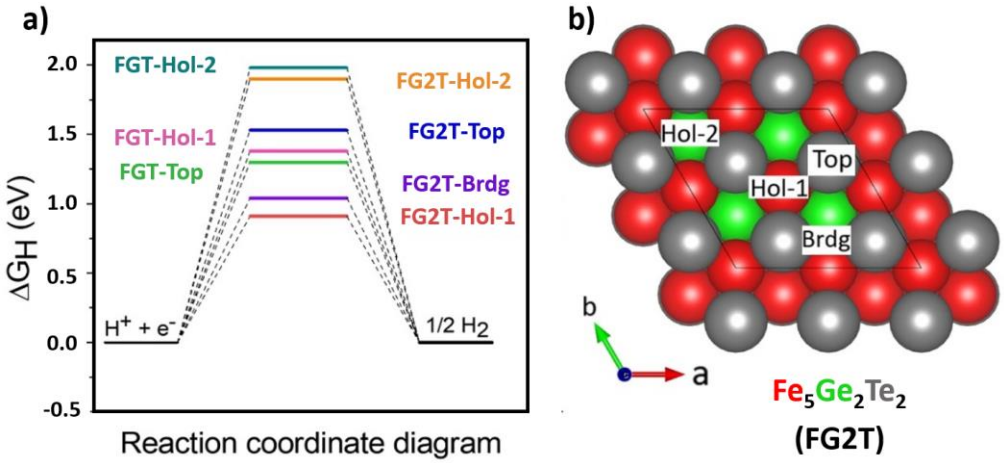

Figure 6.10. a) The Gibbs free energy (ΔG_H) of H-adsorption on the studied active sites of FG2T and FGT (obtained from [28]). **b)** FG2T slab model generated for the (002) basal plane highlighting the studied sites.

6.5. Conclusion

In summary, the iron-rich layered chalcogenide FG2T was synthesized by a solid-state reaction route and characterized through PXRD, SEM, and EDS analyses. The HER

activity of the FG2T pellet was investigated, the results of which demonstrated an improved HER activity by 13.8% if compared to the recently reported iron-poorer FGT pellet. DFT calculations evaluated and confirmed these findings by discovering the existence of numerous active sites on the hexagonal layer of FG2T, two of which attained lower ΔG_H values versus all FGT sites. This study introduces FG2T as a highly HER active trigonal vdW material showing the most active basal plane to date among all vdW materials.

6.6. References

1. Chow, J.; Kopp, R. J.; Portney, P. R., Energy resources and global development. *Science* **2003,** *302* (5650), 1528-1531.
2. Roger, I.; Shipman, M. A.; Symes, M. D., Earth-abundant catalysts for electrochemical and photoelectrochemical water splitting. *Nature Reviews Chemistry* **2017,** *1* (1), 0003.
3. Turner, J. A., Sustainable hydrogen production. *Science* **2004,** *305* (5686), 972-974.
4. Bonaccorso, F.; Colombo, L.; Yu, G.; Stoller, M.; Tozzini, V.; Ferrari, A. C.; Ruoff, R. S.; Pellegrini, V., Graphene, related two-dimensional crystals, and hybrid systems for energy conversion and storage. *Science* **2015,** *347* (6217), 1246501.
5. Xie, Z.; He, P.; Du, L.; Dong, F.; Dai, K.; Zhang, T., Comparison of four nickel-based electrodes for hydrogen evolution reaction. *Electrochim. Acta* **2013,** *88*, 390-394.
6. McCrory, C. C.; Jung, S.; Ferrer, I. M.; Chatman, S. M.; Peters, J. C.; Jaramillo, T. F., Benchmarking hydrogen evolving reaction and oxygen evolving reaction electrocatalysts for solar water splitting devices. *J. Am. Chem. Soc.* **2015,** *137* (13), 4347-4357.
7. Lewis, N. S.; Nocera, D. G., Powering the planet: Chemical challenges in solar energy utilization. *Prog. Nat. Acad. Sci.* **2006,** *103* (43), 15729-15735.
8. Cook, T. R.; Dogutan, D. K.; Reece, S. Y.; Surendranath, Y.; Teets, T. S.; Nocera, D. G., Solar energy supply and storage for the legacy and nonlegacy worlds. *Chem. Rev.* **2010,** *110* (11), 6474-6502.
9. Park, S.; Shao, Y.; Liu, J.; Wang, Y., Oxygen electrocatalysts for water electrolyzers and reversible fuel cells: status and perspective. *Energy & Environmental Science* **2012,** *5* (11), 9331-9344.

10. Feng, J.; Lv, F.; Zhang, W.; Li, P.; Wang, K.; Yang, C.; Wang, B.; Yang, Y.; Zhou, J.; Lin, F., Iridium-based multimetallic porous hollow nanocrystals for efficient overall-water-splitting catalysis. *Adv. Mater.* **2017,** *29* (47), 1703798.
11. Li, H.; Tsai, C.; Koh, A. L.; Cai, L.; Contryman, A. W.; Fragapane, A. H.; Zhao, J.; Han, H. S.; Manoharan, H. C.; Abild-Pedersen, F., Activating and optimizing MoS 2 basal planes for hydrogen evolution through the formation of strained sulphur vacancies. *Nature materials* **2016,** *15* (1), 48-53.
12. Voiry, D.; Fullon, R.; Yang, J.; e Silva, C. d. C. C.; Kappera, R.; Bozkurt, I.; Kaplan, D.; Lagos, M. J.; Batson, P. E.; Gupta, G., The role of electronic coupling between substrate and 2D MoS 2 nanosheets in electrocatalytic production of hydrogen. *Nature materials* **2016,** *15* (9), 1003-1009.
13. Wang, Y.; Li, Y.; Heine, T., PtTe Monolayer: Two-Dimensional Electrocatalyst with High Basal Plane Activity toward Oxygen Reduction Reaction. *Journal of the American Chemical Society* **2018,** *140* (40), 12732-12735.
14. Zhao, Y.; Gu, J.; Chen, Z., Oxygen Evolution Reaction on 2D Ferromagnetic Fe3GeTe2: Boosting the Reactivity by the Self-Reduction of Surface Hydroxyl. *Advanced Functional Materials* **2019,** *29* (44), 1904782.
15. Li, D.; Jia, Y.; Chang, G.; Chen, J.; Liu, H.; Wang, J.; Hu, Y.; Xia, Y.; Yang, D.; Yao, X., A defect-driven metal-free electrocatalyst for oxygen reduction in acidic electrolyte. *Chem* **2018,** *4* (10), 2345-2356.
16. Li, Y.; Yin, K.; Wang, L.; Lu, X.; Zhang, Y.; Liu, Y.; Yan, D.; Song, Y.; Luo, S., Engineering MoS2 nanomesh with holes and lattice defects for highly active hydrogen evolution reaction. *Applied Catalysis B: Environmental* **2018,** *239*, 537-544.
17. Ou, G.; Fan, P.; Ke, X.; Xu, Y.; Huang, K.; Wei, H.; Yu, W.; Zhang, H.; Zhong, M.; Wu, H., Defective molybdenum sulfide quantum dots as highly active hydrogen evolution electrocatalysts. *Nano Research* **2018,** *11* (2), 751-761.
18. Qin, Y.; Wu, H.-H.; Zhang, L. A.; Zhou, X.; Bu, Y.; Zhang, W.; Chu, F.; Li, Y.; Kong, Y.; Zhang, Q., Aluminum and nitrogen codoped graphene: Highly active and durable electrocatalyst for oxygen reduction reaction. *ACS Catalysis* **2018,** *9* (1), 610-619.
19. Luo, Z.; Ouyang, Y.; Zhang, H.; Xiao, M.; Ge, J.; Jiang, Z.; Wang, J.; Tang, D.; Cao, X.; Liu, C., Chemically activating MoS 2 via spontaneous atomic palladium interfacial doping towards efficient hydrogen evolution. *Nature communications* **2018,** *9* (1), 1-8.
20. Zhao, Y.; Wan, J.; Yao, H.; Zhang, L.; Lin, K.; Wang, L.; Yang, N.; Liu, D.; Song, L.; Zhu, J., Few-layer graphdiyne doped with sp-hybridized nitrogen atoms at acetylenic sites for oxygen reduction electrocatalysis. *Nature chemistry* **2018,** *10* (9), 924-931.
21. Zhu, Z.; Yin, H.; He, C. T.; Al-Mamun, M.; Liu, P.; Jiang, L.; Zhao, Y.; Wang, Y.; Yang, H. G.; Tang, Z., Ultrathin transition metal dichalcogenide/3d metal hydroxide hybridized nanosheets to enhance hydrogen evolution activity. *Advanced Materials* **2018,** *30* (28), 1801171.

22. Gao, M.-R.; Liang, J.-X.; Zheng, Y.-R.; Xu, Y.-F.; Jiang, J.; Gao, Q.; Li, J.; Yu, S.-H., An efficient molybdenum disulfide/cobalt diselenide hybrid catalyst for electrochemical hydrogen generation. *Nature communications* **2015,** *6* (1), 1-7.
23. Hong, H.; Liu, C.; Cao, T.; Jin, C.; Wang, S.; Wang, F.; Liu, K., Interfacial engineering of van der waals coupled 2D layered materials. *Advanced Materials Interfaces* **2017,** *4* (9), 1601054.
24. Abrikosov, N. K.; Bagaeva, L.; Dudkin, L., Phase equilibria in Fe-Ge-Te system. *Izv. Akad. Nauk SSSR, Neorg. Mater* **1985,** *21* (10), 1680-1686.
25. Deiseroth, H. J.; Aleksandrov, K.; Reiner, C.; Kienle, L.; Kremer, R. K., Fe3GeTe2 and Ni3GeTe2–Two New Layered Transition-Metal Compounds: Crystal Structures, HRTEM Investigations, and Magnetic and Electrical Properties. *Eur. J. Inorg. Chem.* **2006,** *2006* (8), 1561-1567.
26. Cui, Z.; Xiao, C.; Lv, Y.; Li, Q.; Sa, R.; Ma, Z., Adsorption behavior of CO, CO2, H2, H2O, NO, and O2 on pristine and defective 2D monolayer Ferromagnetic Fe3GeTe2. *Appl. Surf. Sci.* **2020**, 146894.
27. Ma, Z.; Xiao, C.; Cui, Z.; Du, W.; Li, Q.; Sa, R.; Sun, C., Defective Fe 3 GeTe 2 monolayer as a promising electrocatalyst for spontaneous nitrogen reduction reaction. *Journal of Materials Chemistry A* **2021,** *9* (11), 6945-6954.
28. Rezaie, A. A.; Lee, E.; Luong, D.; Yapo, J. A.; Fokwa, B. P., Abundant Active Sites on the Basal Plane and Edges of Layered van der Waals Fe3GeTe2 for Highly Efficient Hydrogen Evolution. *ACS Materials Letters* **2021,** *3*, 313-319.
29. McGlynn, J. C.; Cascallana-Matías, I.; Fraser, J. P.; Roger, I.; McAllister, J.; Miras, H. N.; Symes, M. D.; Ganin, A. Y., Molybdenum ditelluride rendered into an efficient and stable electrocatalyst for the hydrogen evolution reaction by polymorphic control. *Energy Technology* **2018,** *6* (2), 345-350.
30. Toh, R. J.; Sofer, Z.; Luxa, J.; Sedmidubský, D.; Pumera, M., 3R phase of MoS 2 and WS 2 outperforms the corresponding 2H phase for hydrogen evolution. *Chemical Communications* **2017,** *53* (21), 3054-3057.
31. Kresse, G.; Joubert, D., From ultrasoft pseudopotentials to the projector augmented-wave method. *Physical review b* **1999,** *59* (3), 1758.
32. Kresse, G.; Furthmüller, J., Efficient iterative schemes for ab initio total-energy calculations using a plane-wave basis set. *Physical review B* **1996,** *54* (16), 11169.
33. Perdew, J. P.; Burke, K.; Ernzerhof, M., Generalized gradient approximation made simple. *Physical review letters* **1996,** *77* (18), 3865.
34. Hammer, B.; Hansen, L. B.; Nørskov, J. K., Improved adsorption energetics within density-functional theory using revised Perdew-Burke-Ernzerhof functionals. *Physical review B* **1999,** *59* (11), 7413.
35. Tang, Q.; Jiang, D.-e., Mechanism of hydrogen evolution reaction on 1T-MoS2 from first principles. *Acs Catalysis* **2016,** *6* (8), 4953-4961.
36. Chase, M., NIST-JANAF Thermochemical Tables 4th ed. *J. of Physical and Chemical Reffernce Data* **1998**, 1529-1564.
37. Jothi, P. R.; Scheifers, J. P.; Zhang, Y.; Alghamdi, M.; Stekovic, D.; Itkis, M. E.; Shi, J.; Fokwa, B. P., Fe5− xGe2Te2—a New Exfoliable Itinerant Ferromagnet

with High Curie Temperature and Large Perpendicular Magnetic Anisotropy. *physica status solidi (RRL)–Rapid Research Letters* **2020,** *14* (3), 1900666.
38. Yan, Y.; Xia, B. Y.; Ge, X.; Liu, Z.; Fisher, A.; Wang, X., A flexible electrode based on iron phosphide nanotubes for overall water splitting. *Chemistry–A European Journal* **2015,** *21* (50), 18062-18067.
39. Grosvenor, A. P.; Wik, S. D.; Cavell, R. G.; Mar, A., Examination of the bonding in binary transition-metal monophosphides MP (M= Cr, Mn, Fe, Co) by X-ray photoelectron spectroscopy. *Inorganic chemistry* **2005,** *44* (24), 8988-8998.
40. Li, H.; Wen, P.; Li, Q.; Dun, C.; Xing, J.; Lu, C.; Adhikari, S.; Jiang, L.; Carroll, D. L.; Geyer, S. M., Earth-abundant iron diboride (FeB2) nanoparticles as highly active bifunctional electrocatalysts for overall water splitting. *Advanced Energy Materials* **2017,** *7* (17), 1700513.
41. Liang, R.; Shen, L.; Jing, F.; Qin, N.; Wu, L., Preparation of MIL-53 (Fe)-reduced graphene oxide nanocomposites by a simple self-assembly strategy for increasing interfacial contact: efficient visible-light photocatalysts. *ACS applied materials & interfaces* **2015,** *7* (18), 9507-9515.
42. Grossi, V.; Ottaviano, L.; Santucci, S.; Passacantando, M., XPS and SEM studies of oxide reduction of germanium nanowires. *Journal of non-crystalline solids* **2010,** *356* (37-40), 1988-1993.
43. Huang, Y.; Xu, J.-P.; Liu, L.; Lai, P.-T.; Tang, W.-M., N 2-Plasma-Treated Ga 2 O 3 (Gd 2 O 3) as Interface Passivation Layer for Ge MOS Capacitor With HfTiON Gate Dielectric. *IEEE Transactions on Electron Devices* **2016,** *63* (7), 2838-2843.
44. Xie, Q.; Deng, S.; Schaekers, M.; Lin, D.; Caymax, M.; Delabie, A.; Qu, X.-P.; Jiang, Y.-L.; Deduytsche, D.; Detavernier, C., Germanium surface passivation and atomic layer deposition of high-k dielectrics—A tutorial review on Ge-based MOS capacitors. *Semiconductor Science and Technology* **2012,** *27* (7), 074012.
45. Yang, Z.; Xu, M.; Cheng, X.; Tong, H.; Miao, X., Manipulation of dangling bonds of interfacial states coupled in GeTe-rich GeTe/Sb 2 Te 3 superlattices. *Scientific reports* **2017,** *7* (1), 1-9.
46. Reese, M. O.; Perkins, C. L.; Burst, J. M.; Farrell, S.; Barnes, T. M.; Johnston, S. W.; Kuciauskas, D.; Gessert, T. A.; Metzger, W. K., Intrinsic surface passivation of CdTe. *Journal of Applied Physics* **2015,** *118* (15), 155305.
47. Sabri, M. M.; Jung, J.; Yoon, D. H.; Yoon, S.; Tak, Y. J.; Kim, H. J., Hydroxyl radical-assisted decomposition and oxidation in solution-processed indium oxide thin-film transistors. *Journal of Materials Chemistry C* **2015,** *3* (28), 7499-7505.
48. Liu, F.; Chen, C.; Guo, H.; Saghayezhian, M.; Wang, G.; Chen, L.; Chen, W.; Zhang, J.; Plummer, E., Unusual Fe–H bonding associated with oxygen vacancies at the (001) surface of Fe3O4. *Surface Science* **2017,** *655*, 25-30.
49. Trasatti, S.; Petrii, O., Real surface area measurements in electrochemistry. *Pure and applied chemistry* **1991,** *63* (5), 711-734.
50. Benck, J. D.; Chen, Z.; Kuritzky, L. Y.; Forman, A. J.; Jaramillo, T. F., Amorphous molybdenum sulfide catalysts for electrochemical hydrogen production: insights into the origin of their catalytic activity. *Acs Catalysis* **2012,** *2* (9), 1916-1923.

51. Li, J.; Liu, H.-X.; Gou, W.; Zhang, M.; Xia, Z.; Zhang, S.; Chang, C.-R.; Ma, Y.; Qu, Y., Ethylene-glycol ligand environment facilitates highly efficient hydrogen evolution of Pt/CoP through proton concentration and hydrogen spillover. *Energy & Environmental Science* **2019,** *12* (7), 2298-2304.
52. Durst, J.; Siebel, A.; Simon, C.; Hasché, F.; Herranz, J.; Gasteiger, H., New insights into the electrochemical hydrogen oxidation and evolution reaction mechanism. *Energy & Environmental Science* **2014,** *7* (7), 2255-2260.
53. Park, H.; Zhang, Y.; Lee, E.; Shankhari, P.; Fokwa, B. P., High-Current-Density HER Electrocatalysts: Graphene-like Boron Layer and Tungsten as Key Ingredients in Metal Diborides. *ChemSusChem* **2019,** *12* (16), 3726-3731.
54. Skúlason, E.; Karlberg, G. S.; Rossmeisl, J.; Bligaard, T.; Greeley, J.; Jónsson, H.; Nørskov, J. K., Density functional theory calculations for the hydrogen evolution reaction in an electrochemical double layer on the Pt (111) electrode. *Physical Chemistry Chemical Physics* **2007,** *9* (25), 3241-3250.
55. Gupta, S.; Patel, M. K.; Miotello, A.; Patel, N., Metal boride-based catalysts for electrochemical water-splitting: A review. *Advanced Functional Materials* **2020,** *30* (1), 1906481.
56. Tsai, C.; Chan, K.; Nørskov, J. K.; Abild-Pedersen, F., Theoretical insights into the hydrogen evolution activity of layered transition metal dichalcogenides. *Surface Science* **2015,** *640*, 133-140.
57. You, H.; Zhuo, Z.; Lu, X.; Liu, Y.; Guo, Y.; Wang, W.; Yang, H.; Wu, X.; Li, H.; Zhai, T., 1T′-MoTe2-Based On-Chip Electrocatalytic Microdevice: A Platform to Unravel Oxidation-Dependent Electrocatalysis. *CCS Chemistry* **2019,** *1* (5), 396-406.

Chapter 7.

Conclusion

This thesis has focused on the importance of boron and its substructures in achieving extraordinary hydrogen evolution reaction performances and the importance of using structure−activity relationships to design next-generation transition metal borides (TMBs) electrocatalysts. In **chapter 2**, the hydrogen evolution activity according to the boron structure in vanadium boride was studied. As a result, it was found that VB_2, which has a flat boron layer such as graphene, is the most suitable catalyst. Moreover, we found that the ratio of boron with two bonds to boron with three bonds was related to the activity. Based on this, it was found that the activity of the catalyst synthesized using two different metals together (V/Mo) while maintaining the flat boron layer structure showed better activity than that using one metal in **chapter 3**. Especially, the *c* lattice of $V_{1-x}Mo_xB_2$ which was calculated by Rietveld refinement increased and then decreased according to the ratio of the two metals. Interestingly, it was consistent with the hydrogen evolution activity trend. These results prove that there is a direct relationship between the crystal structure and the activity of the catalyst, and the more details studied in our lab since 2017 are summarized in **chapter 4**.

Further from the metal boride, we suggest Mo_2BC, which contains both β-MoB and α-MoC sub-cell in the unit cell, for the first time as HER electrocatalyst in **chapter 5**. Mo_2BC has better activity than β-MoB and α-MoC in acidic media due to the moderate electron density near Mo. Moreover, it also exhibited an excellent activity in an

alkaline solution. In **chapter 6**, we showed that iron-rich layered chalcogenide $Fe_5Ge_2Te_2$ had numerous active sites on the hexagonal layer. The HER activity of the $Fe_5Ge_2Te_2$ pellet demonstrated an improved HER activity by 13.8% if compared to the recently reported iron-poorer Fe_3GeTe_2 pellet.

As shown in this thesis, we suggested that the crystal structure and HER activity are very closely related and proved the relationship between them. The study of this relationship is worth noting in that it can design non-noble electrocatalysts and replace noble-metal-based catalysts because the high cost of noble metal is the main hurdle in this field. Therefore, this work is an important step to achieving a "Hydrogen economy" by improving non-noble HER electrocatalyst.